

Applications of Photoemission Electron Microscopy to Melanin and Melanosomes

by

Dana N. Peles

Department of Chemistry
Duke University

Date: _____

Approved:

John D. Simon, Supervisor

Jie Liu

Stephen L. Craig

David R. Smith

Dissertation submitted in partial fulfillment of
the requirements for the degree of
Doctor of Philosophy in the Department of Chemistry
in the Graduate School of Duke University

2011

ABSTRACT

Applications of Photoemission Electron Microscopy to Melanin and Melanosomes

by

Dana N. Peles

Department of Chemistry
Duke University

Date: _____

Approved:

John D. Simon, Supervisor

Jie Liu

Stephen L. Craig

David R. Smith

An abstract of a dissertation submitted in partial
fulfillment of the requirements for the degree
of Doctor of Philosophy in the Department of
Chemistry in the Graduate School
of Duke University

2011

Copyright by
Dana N. Peles
2011

Abstract

Melanin is a biological pigment that is ubiquitous in nature and generally produced within melanosomes, specialized organelles. Typically, melanin is categorized into two distinct classes, based on color and molecular precursor: eumelanin (brown-black) and pheomelanin (yellow-red). Whereas much is known regarding the molecular precursors to the two pigments, an understanding of their resulting molecular structure remains elusive. Despite this lack of knowledge, several functions are attributed to the pigments, including photoprotection and photosensitization. Epidemiological data for skin and ocular cancers have observed an increased incidence for increased relative concentrations of pheomelanin. Furthermore, eumelanin is generally identified as photoprotective and antioxidant, whereas pheomelanin is generally identified as photoreactive and pro-oxidant. This thesis describes the photophysical properties of the naturally-occurring melanin pigments and presents new insights into their roles within the context of skin and ocular cancers.

Photoemission electron microscopy provides a unique opportunity to probe the complex photoproperties of melanins contained within intact melanosomes isolated from tissues of bovine and human eyes. Photoionization threshold potentials characteristic of eumelanin and pheomelanin have been determined and are used to investigate the molecular architecture of the

pigments within the melanosome. Furthermore, a novel approach to photoemission electron microscopy is used to obtain the first direct measurements of the absorption coefficients from intact melanosomes.

Human iridal stroma melanosomes are comprised of both eumelanin and pheomelanin in various ratios according to iris color; dark brown and blue-green iris melanosomes are characterized by a eumelanin:pheomelanin ratio of 14.8 and 1.3, respectively. Despite the significant difference in the overall pigment composition, a common eumelanin surface photoionization threshold is obtained for both melanosomes. This data indicates that within the melanosome, the phototoxic pheomelanin pigment is encased by eumelanin. This structure mitigates the adverse photochemical properties of pheomelanin. However, damage to the eumelanin exterior and or significant reduction in the amount of eumelanin present could compromise the protective ability of eumelanin, providing mechanisms for exposure of pheomelanin and consequently contributing to oxidative stress.

The absorption spectra of intact melanosomes of varying melanin compositions were determined over the spectral range from 244 to 310 nm. The absorption spectra of eumelanin melanosomes are similar regardless of monomer composition or embryonic origin. Furthermore, the absorption spectra of melanosomes containing a mixture of pigments were similar to those containing

pure eumelanin, arguing that the absorption properties of the melanosome are maintained regardless of increased pheomelanin composition. Therefore, the correlation between epidemiological data and the eumelanin:pheomelanin ratio is not predicted to be a reflection of the melanosome's decreased ability to attenuate biologically relevant wavelengths, but instead is predicted to be a reflection of the different photoreactivities of the melanin pigments contained within.

Contents

| | |
|---|------|
| Abstract..... | iv |
| List of Tables..... | x |
| List of Figures..... | xi |
| List of Abbreviations..... | xiii |
| Acknowledgements..... | xv |
| 1. Description and Functional Significance of Melanin and Melanosomes..... | 1 |
| 1.1 Introduction to Melanin and Melanosomes..... | 1 |
| 1.2 The Structure of Melanin..... | 5 |
| 1.3 Physicochemical Properties and Biological Functions of Melanin..... | 7 |
| 1.3.1 Melanin as a Photoprotector..... | 7 |
| 1.3.2 Melanin as a Photosensitizer..... | 9 |
| 1.3.3 The Current State of Melanin..... | 12 |
| 1.4 Overview of This Dissertation..... | 13 |
| 2. Applications of Photoemission Electron Microscopy to Pigment Research..... | 16 |
| 2.1 Introduction to PEEM..... | 16 |
| 2.2 The PEEM Instrument in Detail..... | 19 |
| 2.2.1 Spatial Dependence of the Signal..... | 22 |
| 2.3 Determination of Threshold Potentials..... | 25 |
| 2.3.1 Substrate Preparation..... | 25 |
| 2.3.2 Excitation Source..... | 26 |

| | | |
|-------|--|----|
| 2.3.3 | Measurement Procedure | 26 |
| 2.4 | Determination of Absorption Coefficients..... | 29 |
| 2.4.1 | Substrate Preparation..... | 29 |
| 2.4.2 | Excitation Source | 30 |
| 2.4.3 | Measurement Procedure | 31 |
| 3. | Structural and Morphological Analysis of Human Iridal Stroma Melanosomes | 42 |
| 3.1 | Introduction..... | 42 |
| 3.2 | Materials and Methods | 45 |
| 3.2.1 | Sample Isolation..... | 45 |
| 3.2.2 | Scanning Electron Microscopy | 46 |
| 3.2.3 | Free Electron Laser-Photoemission Electron Microscopy | 46 |
| 3.2.4 | Atomic Force Microscopy..... | 47 |
| 3.3 | Results and Discussion | 47 |
| 3.3.1 | Shape and Size Analysis of Iridal Stroma Melanosomes..... | 47 |
| 3.3.2 | Surface Photoionization Potentials of Iridal Stroma Melanosomes | 51 |
| 3.3.3 | Morphological Surface Organization of Iridal Stroma Melanosomes | 52 |
| 3.4 | Conclusions | 59 |
| 4. | Ultraviolet Absorption Coefficients of Bovine Ocular Melanosomes Containing Eumelanin | 61 |
| 4.1 | Introduction..... | 61 |
| 4.2 | Materials and Methods | 63 |

| | | |
|-------|---|-----|
| 4.2.1 | Sample Isolation..... | 63 |
| 4.2.2 | Photoemission Electron Microscopic Analysis | 65 |
| 4.3 | Results | 65 |
| 4.4 | Discussion | 74 |
| 4.5 | Conclusions | 86 |
| 5. | The Ultraviolet Absorption Coefficients of Human Iridal Stroma Melanosomes | 87 |
| 5.1 | Introduction..... | 87 |
| 5.2 | Materials and Methods | 89 |
| 5.2.1 | Sample Isolation..... | 89 |
| 5.2.2 | Photoemission Electron Microscopic Analysis | 90 |
| 5.3 | Results and Discussion | 90 |
| 5.4 | Conclusions | 101 |
| | References | 103 |
| | Biography | 119 |

List of Tables

| | |
|---|----|
| Table 1: Summary of the size analysis of the melanosomes isolated from human irides..... | 50 |
| Table 2: Summary of the chemical degradation analyses and absorption coefficients of eumelanic melanosomes..... | 73 |

List of Figures

| | |
|---|----|
| Figure 1: Abbreviated depiction of the early steps of melanogenesis..... | 4 |
| Figure 2: A schematic of the PEEM instrument..... | 20 |
| Figure 3: Spatially dependent signal considerations for spherical objects..... | 24 |
| Figure 4: Experimental geometry for PEEM of single melanosomes..... | 32 |
| Figure 5: A top view (x-y dimension) simulation of the interaction of electromagnetic radiation with an ellipsoid..... | 34 |
| Figure 6: Geometrical model of an ellipsoid with dimensions a, b, and c..... | 38 |
| Figure 7: SEM images of (A) dark brown iris melanosomes and (B) blue-green iris melanosomes..... | 48 |
| Figure 8: The distributions of the widths and lengths of dark brown iris melanosomes (A, B) and blue-green iris melanosomes (C, D). | 49 |
| Figure 9: Integrated wavelength-dependent FEL-PEEM data for A) dark brown iridal stroma melanosomes and (B) blue-green iridal stroma melanosomes..... | 53 |
| Figure 10: AFM images of dark brown iridal stroma melanosomes. | 54 |
| Figure 11: PEEM images of melanosomes isolated from A) adult and B) newborn bovine RPE, C) adult and D) newborn choroid melanosomes, and E) adult bovine iris. | 66 |
| Figure 12: Spatial dependence of the shadows depicted through A) an intensity contour plot and B, C) intensity line scans..... | 68 |
| Figure 13: A sequence of PEEM images showing the wavelength-dependence of a single adult bovine RPE melanosome and its shadow on a SiC substrate. | 69 |
| Figure 14: Average absorption coefficients measured at $\lambda = 244$ nm with different experimental conditions..... | 71 |
| Figure 15: Summary of the average measured absorption coefficients of the bovine eumelanosomes versus wavelength..... | 75 |

| | |
|---|----|
| Figure 16: Plot of the observed absorption coefficient versus DHICA content at $\lambda = 244$ nm..... | 79 |
| Figure 17: Predicted absorption spectra as arising from the sum of the absorption of contributing DHI and DHICA..... | 81 |
| Figure 18: Comparison of the PEEM measured absorption coefficients with those previously reported in literature. | 85 |
| Figure 19: PEEM Images of dark brown iridal stroma melanosomes at A) $\lambda = 244$ nm and B) $\lambda = 310$ nm. | 91 |
| Figure 20: Average absorption coefficients versus wavelength for melanosomes isolated from dark brown and blue-green iridal stroma tissues..... | 94 |
| Figure 21: Extinction coefficients as a function of wavelength for eumelanin and pheomelanin. | 97 |
| Figure 22: Extinction coefficients of the A) eumelanin and B) pheomelanin monomers..... | 99 |

List of Abbreviations

| | |
|--------|---|
| 4-AHP | 4-amino-3-hydroxyphenylalanine |
| AFM | atomic force microscopy |
| BZ | 6-(2- amino-2-carboxyethyl)-4-hydroxy- benzothiazole |
| CCD | charge-coupled device |
| DHBTCA | dihydro-1,4-benzothiazine-3-carboxylic acid |
| DHI | 5,6-dihydroxyindole |
| DHICA | 5,6-dihydroxyindole-2-carboxylic acid |
| EPR | electron paramagnetic resonance |
| FEL | free electron laser |
| IPE | iridal pigment epithelium |
| PBS | phosphate buffered saline |
| PBSA | Dulbecco's phosphate buffered saline without calcium and magnesium |
| PDCA | pyrrole-2,3-dicarboxylic acid |
| PEEM | photoemission electron microscopy |
| PTCA | pyrrole-2,3,5-tricarboxylic acid |
| ROS | reactive oxygen species |
| RPE | retinal pigment epithelium |
| SEM | scanning electron microscopy |
| TEM | transmission electron microscopy |

| | |
|-----|-------------------|
| TM | total melanin |
| UHV | ultra high vacuum |
| UV | ultraviolet |

Acknowledgements

First and foremost, I would like to thank my advisor Dr. John Simon, for his continued guidance, support and encouragement throughout my time at Duke. Your interest and influence in my development as a forward-thinking research scientist has motivated me and will continue to resonate throughout my future. Thank you.

Secondly, I thank my committee: Dr. Stephen Craig, Dr. Jie Liu, Dr. David Smith and Dr. David Brady, for their commitment and scientific knowledge throughout the years. I also gratefully acknowledge several key collaborators: Dr. April Brown and Dr. Tong-Ho Kim for helpful assistance and discussions regarding SiC substrates; Dr. Robert Guenther for many helpful discussions regarding diffraction; and Dr. Yongan Tang for helpful modeling simulations.

I would like to thank past and current members of the Department of Chemistry at Duke and of the Simon Lab. In particular, I thank Dr. Lian Hong for her invaluable contributions to the chapters presented in this thesis: the isolation of the samples used herein, stimulating discussions and senior mentorship in the Simon lab. I also extend thanks to Dr. Jacob Garguilo who efficiently and thoroughly trained me on the PEEM, its vacuum and optical components, and its use in pigment cell research. Outside of the Simon Lab, I

thank Dr. Sarah Crider for her wisdom and guidance in successfully navigating and surviving my graduate experience – both scholarly and socially.

Finally, I thank my family. I thank my parents for fostering my curiosity, always encouraging me to aim high and instilling the values in me that I needed to get through the past five years. I thank my grandparents for their constant support and belief in me, regardless of how much I tried to convince them otherwise. I thank my sister for her continued optimism; graduate school (and Duke basketball games) wouldn't have been the same without her continual cheering and encouragement. And most importantly, I thank my husband, Jeremy Edmunds, for the patience, love and support that he provided throughout my time at Duke. I am forever thankful for everything he has done to make this thesis possible, from our FEL dinners to being my practice “audience” and ultimately supporting all of my endeavors in every way he possibly could.

1. Description and Functional Significance of Melanin and Melanosomes¹

1.1 Introduction to Melanin and Melanosomes

Melanin is a generic term used to describe the ubiquitous natural and synthetic phenolic-quinone pigments. The natural melanins are found in: the skin, hair, eye, brain and inner ears of man and other mammals; the feathers of birds; the ink sacs of cuttlefish; and in some fungi. The historical progression of the observation and subsequent study of melanin reaches back over several centuries. Initial experimental studies aimed to understand ethnic pigmentation were reported by Santorio Santorius in 1614, which attributed the color of black skin to the presence of bile (Santorius, 1614). In the early 18th century, studies by Alexis Littre failed to find bile in skin but instead reported the presence of an insoluble black pigment adhered to the reticular membrane (Littre, 1720). Melanin had been discovered, but it wasn't until the turn of 20th century that a more molecular picture of pigments and their formation was obtained.

In 1896, shortly after the discovery of tyrosinase in fungi (Bourquelot and Bertrand, 1895), Bertrand established that tyrosinase converted tyrosine into a black pigment that appeared similar to mammalian melanin (Bertrand, 1896). Experiments

¹ Reproduced in part from: Simon, J. D.; Hong, L., and Peles, D. N. (2008) *J. Phys. Chem. B.*, **112**: 13201-13217, DOI: 10.1021/jp804248h and Simon, J. D. and Peles, D. N. (2010) *Acc. Chem. Res.*, **43**: 1452-1460, DOI: 10.1021/ar100079y

later conducted on mammalian tissues, however, reported melanin formation through the enzymatic oxidation of dopa, rather than tyrosine, by an enzyme termed dopa-oxidase (Bloch and Schaaf, 1925), although, at that point in time, dopa had never been observed in mammalian skin and the enzyme had not been isolated. In 1927, Henry Raper isolated dopa as the primary product of the reaction of tyrosinase with tyrosine and through careful chemical studies subsequently established the primary chemical steps for the enzymatic oxidation of tyrosine to mammalian melanin (Raper, 1927). In doing so, Raper isolated derivatives of 5,6-dihydroxyindole (DHI) and 5,6-dihydroxyindole-2-carboxylic acid (DHICA), which are the two indoles now considered to be the fundamental building blocks of the black pigment eumelanin. Raper's molecular scheme was extended in 1948 by Howard Mason to introduce a "polymer" model of melanin, involving self-condensation of indole quinones (Mason, 1948).

During the 1960s, studies of various natural pigments resulted in the classification of melanin into two major types – the brown black eumelanin (eu – a Greek prefix for "good, well") and the yellow red pheomelanin (phaeo – a Greek prefix meaning "dusky", now commonly written pheomelanin). An important chemical difference between these classes was revealed in 1966 when Guiseppe Prota, Mario Piattelli and Rodolfo Nicolaus proposed that pheomelanin resulted from the specific reaction of cysteine with the quinones produced by tyrosine oxidation, a reaction that does not occur in the synthesis of eumelanin (Prota et al., 1966). Between 1967 and 1968,

Prota, Nicolaus, and collaborators isolated melanin from red feathers, and established the centrality of 5-S-cysteinyl-dopa as a precursor to pheomelanin (Minale et al., 1967; Prota and Nicolaus, 1967a, 1967b; Nicolaus, 1968).

The current understanding of the initial steps of the melanogenesis of the melanin pigments, commonly called the Raper-Mason scheme, is shown in **Figure 1** (Ito and Wakamatsu, 2008). As indicated, the two major types of melanin reflect different molecular precursors in the melanogenesis. Pigment formation is initiated by the enzymatic oxidation of tyrosine to dopaquinone, which is subsequently the branch point between the formation of eumelanin and pheomelanin. In the absence of cysteine, dopaquinone undergoes an intramolecular cyclization, leading to the formation of eumelanin through the DHI and DHICA precursors. However, in the presence of cysteine, dopaquinone progresses through a series of reactions to form a variety of cysteinyl-dopa adducts, which eventually form pheomelanin through benzothiane units. Though these two melanogeneses are chemically distinct, both are often present in the same pigment-generating cell, the melanocyte (Prota et al., 1998; Ito and Wakamatsu, 2003; Wakamatsu et al., 2006; Wakamatsu et al., 2007). While pure eumelanin is found throughout nature, pure pheomelanin is not observed and rarely makes up a significant composition of the total melanin present.

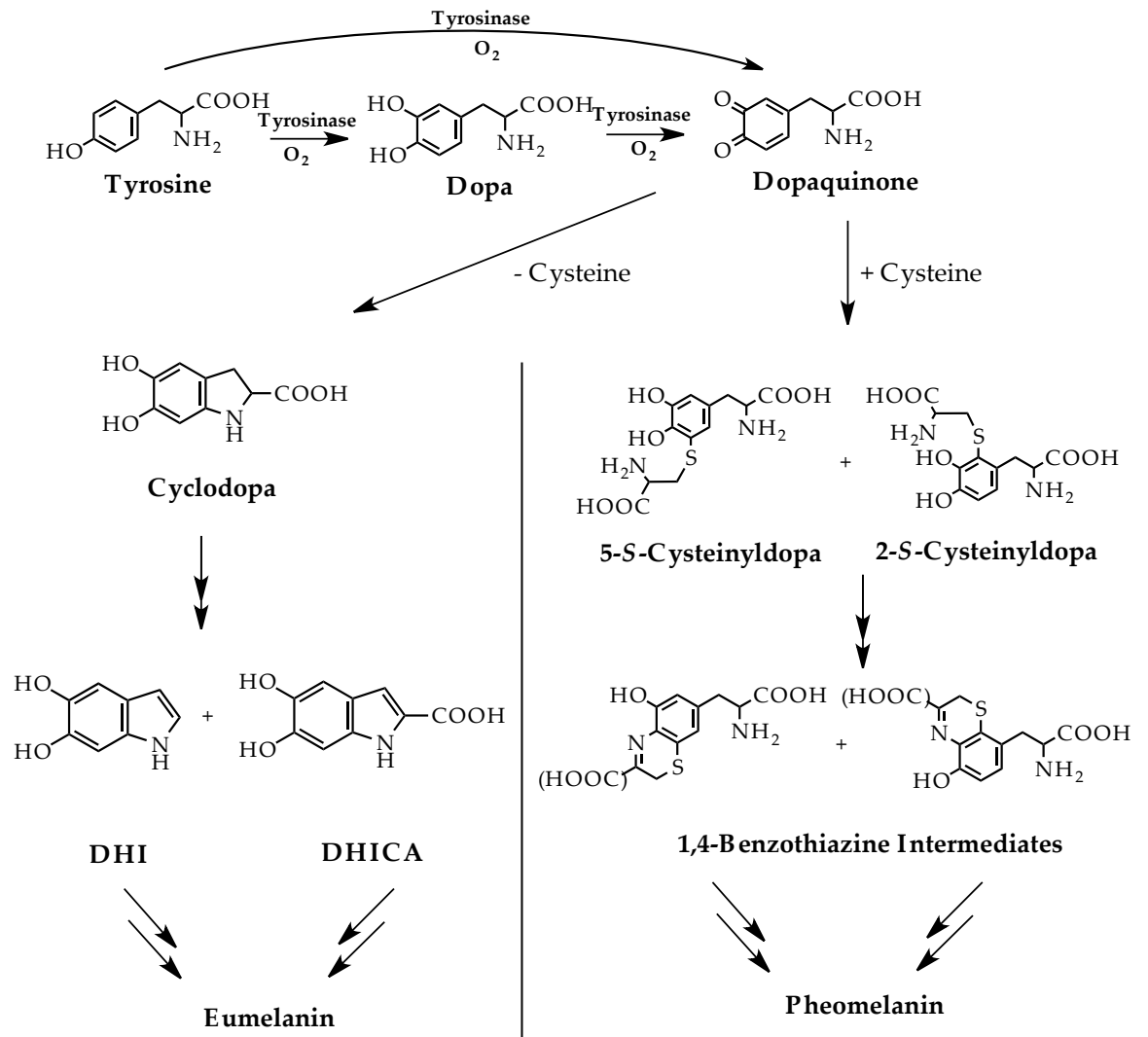


Figure 1: Abbreviated depiction of the early steps of melanogenesis. Initiation of melanogenesis is the oxidation of tyrosine by tyrosinase. Dopaquinone is the branch point between the formation of eumelanin and pheomelanin.

In situ, melanocytes synthesize melanin within specialized organelles termed melanosomes. Note, that like most cellular organelles, melanosomes are membrane-bound structures that also contain lipids, enzymes, metals and proteins (Prota, 1992). The melanocytes are categorized into two distinct types: cutaneous, found in the skin and hair, and extracutaneous, found in the eye and inner ear, among others (Boissy and Hornyak, 2006). The ocular melanocytes are of significance for pigment cell research because the different layers of pigmented tissues originate from two different embryonic origins: the uveal melanocytes – found in the iris and choroid – are derived from the neural crest, similar in origin to the cutaneous melanocytes, whereas the retinal pigment epithelium (RPE) and iridal pigment epithelium (IPE) cells are derived from the outer neuroectodermal sheath of the eyecup (Schraermeyer and Heimann, 1999; Bumsted and Barnstable, 2000; Boissy and Hornyak, 2006).

1.2 The Structure of Melanin

The complexities of melanins have so far hindered a detailed understanding of their molecular structures (Prota, 1992; Ito and Wakamatsu, 2006). First, the high molecular weight pigments are virtually insoluble in most all solvents, resulting in difficulties of isolation of the melanins in pure form and utilization of common characterization techniques. Second, the pigments are amorphous and particulate in nature. And thirdly, these pigments are heterogeneous and are made up of mixtures of more or less similar polymers comprised of different monomer units linked through

nonhydrolyzable bonds. To circumvent these obstacles and probe the molecular compositions of the pigment, powerful and informative approaches were developed that were based on the oxidative and reductive degradation of the pigments, followed by identification and quantification of the molecular markers produced (Panizzi and Nicolaus, 1952; Fattorusso et al., 1968; Benathan and Wyler, 1980; Prota, 1998; Ito and Wakamatsu, 2006). These markers were further quantitatively related to the presence of specific chemical moieties present in the original pigment.

Shosuke Ito refined many of these analytical approaches (Ito et al., 2000; Wakamatsu and Ito, 2002), and his methods are currently employed to derive molecular information about melanins from different tissues. The pyrrole units, pyrrole-2-3-5-tricarboxylic acid (PTCA) and pyrrole-2,3-dicarboxylic acid (PDCA), derived from the oxidation products of eumelanin, are routinely used to infer the relative contributions of the specific molecular monomers DHICA and DHI, respectively, to the eumelanin pigment (Piattelli et al., 1962; Benathan and Wyler, 1980; Ito and Fujita, 1985; Wakamatsu and Ito, 2002). Additionally, the 4-amino-3-hydroxyphenylalanine (4-AHP) degradation product derived from the reductive hydrolysis of pheomelanin with hydriodic acid is routinely used to infer the relative contributions of pheomelanin (Ito and Jimbow, 1983; Wakamatsu and Ito, 2002). In short, these approaches quantify structural information regarding a) the relative amounts of eumelanin and pheomelanin present in a sample of pigment and b) the relative amounts of DHI and DHICA present

in eumelanin. Although these methods fail to provide information on the chemical connectivity between the molecular monomers, the ability to determine the relative contributions of the molecular monomers to the overall architecture of the pigment plays an important role in developing structure/function models for melanin.

1.3 *Physicochemical Properties and Biological Functions of Melanin*

The unique physicochemical properties of melanins include: broad-band absorption through the UV and visible, photoreactivity, anti-oxidant and free-radical scavenging, redox reactivity, and binding of metal ions and organic cations (Hill, 1992; Sarna and Swartz, 2006). These properties, a result of the pigment structures, define the biological functions of melanins. For purposes of this thesis, descriptions of the main properties of eumelanin and pheomelanin related to the specific biological roles of photoprotection and photosensitization are presented.

1.3.1 Melanin as a Photoprotector

The optical absorption spectra observed for natural and synthetic melanins is featureless and increases nearly monotonically with decreasing wavelength through the UV (Crippa et al., 1978; Sarna and Sealy, 1984b; Nofsinger et al., 2002b; Sarna and Swartz, 2006). These spectral properties establish the critical photoprotective biological function of melanin as its broad-band absorption in the skin and eye mitigates the exposure of underlying tissues to harmful radiation (Kollias et al., 1991). However, this characteristic feature is complex and despite significant efforts to understand the

unusual optical properties, melanin absorption has defied explanation (Meredith and Sarna, 2006; Sarna and Swartz, 2006; Pezzella et al., 2009a).

Due to the insolubility and particulate nature of the melanins, the absorption spectrum is likely a result of a complex combination of absorption and scattering at different wavelengths and further depends on the aggregation status of melanin in solution (Nofsinger et al., 2002b; Sarna and Swartz, 2006). As a result, and because of the difficulties of isolating natural melanin in pure form, studies of the optical absorption properties of melanins are often carried out on soluble synthetic model systems (Ito, 1989; Sarna and Swartz, 2006; Riesz et al., 2007; Pezzella et al., 2009a). Optical absorption reported for soluble synthetic eumelanin and pheomelanin were found to be similar and well described by the characteristic monotonic broadband absorption (Sarna and Swartz, 2006). It is important to note, however, that while synthetic samples are widely studied, the absorption spectra of melanins depend on several factors, including the synthetic method used and the oxidation/reduction state of various sites within the resulting polymer (Sarna, 1992).

The ability of melanins to scavenge reactive oxygen species (ROS) and mitigate their damaging effects on cellular processes is yet another photoprotective property attributed to the pigments (Bustamante et al., 1993; Meredith and Sarna, 2006; Sarna and Swartz, 2006). These antioxidant properties have been examined through studies measuring the rate constants of the interaction of different melanins with singlet oxygen

and other free radicals with various EPR techniques (Sarna et al., 1985; Korytowski et al., 1986) and pulse radiolysis methods (Sarna et al., 1986; Rózanowska et al., 1999). The apparent rate constants obtained from the pulse radiolysis methods revealed that although the oxidation of synthetic eumelanin by oxidizing radicals was easier than that of synthetic pheomelanin, both synthetic melanins were efficient scavengers of strongly oxidizing free radicals. Furthermore, recent studies on irradiated natural human RPE cells have suggested that the melanin contained within provided protection against light-induced apoptosis through the quenching of photogenerated ROS (Seagle et al., 2005).

1.3.2 Melanin as a Photosensitizer

Despite the photoprotective properties of melanins established above, the pigments can also act as photosensitizers and generate harmful ROS upon aerobic photoexcitation (Chedekel et al., 1978; Felix et al., 1978; Chedekel et al., 1980; Sarna and Sealy, 1984b; Korytowski et al., 1987; Hubbard-Smith et al., 1992; Sarna and Swartz, 2006). Action spectra for photoinduced oxygen consumption were reported for a variety of synthetic and natural melanins and while found to resemble each other, they generally differed significantly from their absorption spectra (Sarna et al., 1984; Sarna and Sealy, 1984a). An explanation was put forth for this disparity in the case of eumelanin through comparisons of the optical properties of different particle-sized fractions with their free-radical generation (Nofsinger et al., 1999; Nofsinger et al.,

2002b). The action spectra were found to match the absorption spectrum of the oligomeric constituents of the natural eumelanins. Furthermore, subsequent studies established that aggregation of these constituents affected their aerobic reactivity (Nofsinger et al., 2002a); the unaggregated oligomeric constituents were found to have a higher efficiency towards ROS photogeneration than the aggregated oligomers. In the case of pheomelanin, it was demonstrated that different molecular constituents are responsible for the emission, transient absorption, and oxygen photoconsumption exhibited by the pigment (Ye et al., 2008). These later studies also observed increased aerobic reactivity of pheomelanin in the UV-A.

The UV photosensitization of pheomelanin has been hypothesized to be linked to an increased susceptibility of skin and ocular cancers for individuals of lighter-colored skin, hair and eyes (Chedekel et al., 1978; Wenczl et al., 1998b; Davies et al., 2002; Wakamatsu et al., 2007; Hu et al., 2008). In exploring this hypothesis, Prota and co-workers have reported that UV sensitivity is associated with high pheomelanin and low eumelanin levels (Vincensi et al., 1998). In contrast, it was reported that factors other than the amount of pheomelanin may be important in determining cancer susceptibility based on an examination of the eumelanin and pheomelanin concentrations in human skin before and after exposure to UV radiation (Hennessy et al., 2005). Douglas Brash and co-workers examined the induction of DNA lesions and apoptosis upon UV exposure of congenic mice with black, yellow, and albino coats (Takeuchi et al., 2004). In

their experiments, UV-B-induced cyclobutane dimerization and apoptosis measured by sunburn cells or keratinocytes containing active caspase-3 were found to be strain independent. However, the UV irradiation of melanin was found to photosensitize adjacent cells to caspase-3 independent apoptosis at a frequency greater than the apoptosis induced through UV absorption by DNA. In particular, pheomelanin exhibited a 3-fold greater activity than eumelanin, supporting the hypothesis that melanin-induced apoptosis may contribute to the observed epidemiology of skin cancer for black-, blond-, and red-haired populations. A suggestion in support of a causative role of pheomelanin is also provided by experiments on UV-A-induced DNA single-strand breaks in human melanocytes differing only in the type of pigment produced; such reactivity occurs in cells expressing pheomelanin, arguing that the origin is an intrinsic chromophore, most likely pheomelanin itself and/or a molecule produced along the pigment's synthetic route (Wenczl et al., 1998b).

Initially reported studies on the photoreactivity of synthetic pheomelanin found that the activation of molecular oxygen resulted from pigment photoionization by UV-A radiation (Chedekel et al., 1978; Chedekel et al., 1980). Building on this mechanistic work, photoemission electron microscopy (PEEM) was used to quantify the photoionization threshold for natural eumelanin and pheomelanin using melanosomes isolated from human black- and red-hair respectively (Samokhvalov et al., 2005; Ye et al., 2006). The PEEM data revealed a common ionization threshold at 282 nm

characteristic for both melanosomes, reflecting the presence of eumelanin in both samples. Pheomelanosomes (melanosomes exhibiting a large concentration of pheomelanin), however, exhibited a unique second ionization threshold at 326 nm, which was attributed to the benzothiazine structural motif present in pheomelanin. The fact that pheomelanin has a lower ionization potential than eumelanin is supportive of the view that pheomelanin could be an active contributor to the greater incidence rate of UV-induced cancers observed for red-haired vs. black-haired individuals. Compelling evidence in support of this assignment was determined by probing the threshold ionization potentials for synthetic pheomelanin by time-resolved spectroscopic detection of solvated electrons and EPR measurements of the photoconsumption of oxygen following excitation of dissolved synthetic pheomelanin in water (Ye et al., 2006). All studies were consistent with the photoionization threshold determined for the pheomelanin contained in human red-hair, and further established the relevance of the threshold potential data collected under the high vacuum conditions of PEEM to those exhibited by pigments in physiologically relevant buffer solutions.

1.3.3 The Current State of Melanin

As described, melanin's photoprotective properties are interrelated to their potentially deleterious side effects of photoinduced oxidative stress and a delicate balance may exist between the two. Based on the increased photoreactivity of synthetic pheomelanin to eumelanin and the observed epidemiological correlation between skin

and ocular cancers and pheomelanin concentrations, the photoreactivity of the two pigments are generally thought to reflect an antioxidant, protective eumelanin contrasted to a reactive and pro-oxidant pheomelanin (Chedekel et al., 1978; Harsanyi et al., 1980; Persad et al., 1983; Takeuchi et al., 2004; Ye et al., 2006). Further studies of the interaction of UV and visible light of melanins contained within intact natural melanosomes are needed to fully understand the dichotomy of the attributed biological functions in cutaneous and extracutaneous tissues.

1.4 Overview of This Dissertation

In this dissertation, the structural and photophysical properties of natural, intact melanosomes were probed with PEEM, a unique, surface sensitive, imaging microscopy, to examine the potential role they may play in the epidemiology of skin and uveal cancers.

As described, intact melanosomes are not amenable to quantitative assessment through conventional techniques and thus, established and novel applications of PEEM have been utilized to assess their complex properties. **Chapter 2** presents the historical perspective of biologically focused PEEM and provides specific details of the instrument (Peles and Simon, 2009). Experimental methodologies are described for the determination of threshold potentials and absorption coefficients. The PEEM assessment of these two properties is of biological importance and provides key insight into the photoproperties of melanins within the melanosome.

Chapter 3 presents a structural analysis of mixed-melanin uveal melanosomes isolated from the iridal stroma of different colored human irides (Peles et al., 2009). The different colored iridal stroma melanosomes vary in their eumelanin:pheomelanin ratios and provide an excellent system to study the structural morphology of mixed melanogenesis. Atomic force microscopy (AFM) and scanning electron microscopy (SEM) were used to examine the size and overall morphology of these melanosomes. PEEM was used to measure their photoionization potentials to examine the structural morphology of the two pigments contained within. The structural observations provided by the aforementioned microscopies contribute to the understanding of the potential contribution iridal stroma melanosomes may have in inducing oxidative stress and accounting for the observed iris-color-dependent epidemiology of uveal melanoma.

The optical UV absorption coefficients were quantified for intact, natural melanosomes to further measure the photophysical properties of melanin. Preliminary measurements were carried out on melanosomes isolated from different ocular tissues of bovine eyes (Peles et al., 2010; Peles and Simon, 2010a). These melanosomes are eumelanin, but vary in their relative DHICA/DHI content and their embryonic origin, thus providing a model system to probe the eumelanin absorption as a function of monomer composition and embryonic origin (**Chapter 4**). After the optical properties of eumelanin had been established, the absorption coefficients were measured for the dark brown and blue-green human iridal stroma melanosomes, described in **Chapter 3**, to

determine the absorption coefficient of pheomelanin (**Chapter 5**) (Peles and Simon, 2010b). These data provide the first directly quantified absorption coefficients from single, intact melanosomes.

2. Applications of Photoemission Electron Microscopy to Pigment Research¹

2.1 Introduction to PEEM

PEEM is a unique, surface-sensitive technique capable of providing real time images of the surface of a sample under high spatial resolution. The physical principle underlying this technique is the photoelectric effect. Simply, electrons are emitted from the surface of the sample when the associated photon energy of the incident light is above the photoionization threshold value characteristic of the sample of interest. The generated photoelectrons are accelerated through a series of electron optics and the surface of the sample is imaged at a high magnification. The first PEEM images were published in 1933 (Brüche, 1933). Following these preliminary images tremendous development in the understanding and instrumentation of PEEM has been achieved (Griffith and Rempfer, 1988; Bauer, 1994).

Although, PEEM is currently used extensively in the field of materials science, O. Hayes Griffith, a pioneer of PEEM technology, initially applied the technique to biological samples and reported first PEEM images of rat epididymis (Griffith et al., 1972). Griffith and his group realized the capabilities of PEEM as the electron-optics analog of fluorescence microscopy and used colloidal gold and silver enhanced colloidal

¹ Reproduced in part from: Peles, D. N., and Simon, J. D. (2009) *Photochem. Photobiol.*, **85**: 8-20, DOI: 10.1111/j.1751-1097.2008.00484.x

gold particles to selectively label portions of a biologic with a higher spatial resolution (Birrell et al., 1985; Griffith and Birrell, 1985; Griffith and Rempfer, 1988). PEEM images for cells (Dam et al., 1977; Nadakavukaren et al., 1981; Habliston et al., 1995), viruses (Houle and Griffith, 1983b; Birrell et al., 1994), and DNA (Houle and Griffith, 1983a; Griffith et al., 1990; Habliston et al., 1993; Birrell et al., 1994), among others (Grund et al., 1979; Birrell et al., 1983; Nadakavukaren and Griffith, 1985), were reported using both labeling and non-labeling techniques. In addition to the experimental evidence, reviews were written establishing PEEM as a powerful tool for biological imaging (Griffith and Rempfer, 1985; Griffith, 1986; Birrell et al., 1991).

Despite the capabilities demonstrated by Griffith and others, the technique did not flourish in the biological sciences and applications of PEEM to biological systems have lagged behind complementary electron imaging techniques, such as SEM and TEM. Instead, as an ultra high vacuum (UHV) instrument suited for relatively flat samples, PEEM found prominence in the fields of surface and materials sciences (Mundschau, 1991; Bauer, 1994). PEEM's applications in surface and materials sciences go beyond imaging. For instance, surface dynamics can be imaged during in situ experiments (e.g. heating, cooling, exposure to reactive gases, etc.) by monitoring the changes in the electronic properties of the surface (Bethge and Klaua, 1983; Mundschau et al., 1990; Mundschau, 1991; Rotermund, 1993; Ehsasi, 1994; Kordesch, 1995; Zeman et al., 2006). If the resulting work function of the modified surface is below (above) the

photon energy of the incident light an image will (will not) be observed. Subsequently, and more importantly for the purposes of this thesis, tunable monochromatic light sources have made it possible to scan a series of photon energies to obtain the work function or selectively turn on or off a particular region of the sample (Ade et al., 1998; Li et al., 2005; Nakano et al., 2008). Thus, PEEM has become a critical tool in surface and materials sciences that is capable of achieving valuable and unique information.

Motivated by the challenges of melanin research, a result of the complex nature of the pigments, the Simon group, in collaboration with Robert Nemanich's group, extended the application of biological PEEM to mirror its use in surface and materials sciences. As a result, photoionization thresholds (work functions) were determined for different types of intact natural melanosomes (Samokhvalov et al., 2004; Samokhvalov et al., 2005; Bush et al., 2006; Hong et al., 2006; Ye et al., 2006; Garguilo et al., 2007). The photoionization thresholds determined for eumelanin and pheomelanin are of biological importance for understanding the potentially phototoxic role of pheomelanin as compared to eumelanin. This technique (described herein) and these results have provided a foundation for the research described in **Chapter 3** on the examination of the morphology of mixed melanins in intact melanosomes. Furthermore, in continuing to expand applications of PEEM to probe critical photophysical properties of melanosomes, the changes in the electronic properties of the substrate were analyzed at different UV wavelengths to measure optical absorption spectra in a similar fashion to the

measurement of the surface dynamics for surface and materials sciences. This novel technique, which has enabled the direct quantification of the absorption coefficients of single, intact melanosomes of variable pigment composition, as described in **Chapters 4** and **5**, is also developed herein.

2.2 The PEEM Instrument in Detail

A schematic of the PEEM is shown in **Figure 2**. The instrument consists of a main chamber, a lens column and a detection center, all of which are held under UHV. Emission of photoelectrons occurs when light of an appropriate wavelength is illuminated on the surface of a sample. A variety of photon sources are available to excite the electrons (X-ray, synchrotron radiation, or UV arc lamps and lasers). UV excitation is generally required to photoionize the valence electrons of biological materials, and is the spectral range utilized for the pigment research described throughout this thesis. As a consequence of the instrumental design the sample must be illuminated with a photon beam at a high incident angle, $\sim 77^\circ$ from the surface normal. This is necessary because the maximal resolution of the instrument is achieved only when there is a short working distance between the anode and the sample ($\sim 4\text{mm}$), shown in **Figure 2**.

Typically, the sample is held at a negative potential (-20kV) and an electric field is created between it and a grounded anode. This potential accelerates the generated

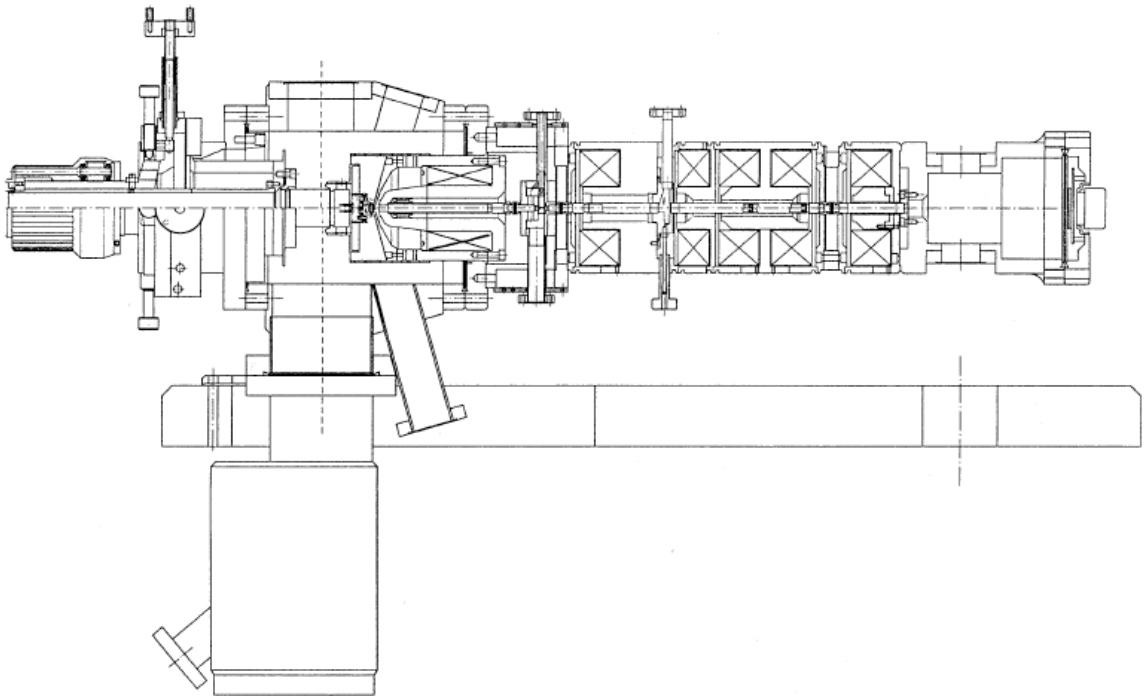


Figure 2: A schematic of the PEEM instrument. The instrument consists of the main chamber, lens column and detection center. The anode and sample cartridge are depicted in the main chamber. Reprinted from: A Free Electron Laser – Photoemission Electron Microscope System (FEL-PEEM) by H. Ade, W. Yang, S. L. English, J. Hartman, R. F. Davis, R. J. Nemanich, V. N. Litvinenko, I. V. Pinayev, Y. Wu and J. M. J. Madey in Surface Review and Letters, Copyright @ 1998 World Scientific.

photoelectrons through a series of electron optics. After passing through the lens column, the emitted electrons are amplified by a microchannel plate and subsequently imaged onto a phosphor screen. A CCD camera captures the data from the screen. The electron optics project the image plane of the sample onto the microchannel plate, thus enabling the direct collection of a spatially-resolved image.

For a geometrically flat sample, the current lateral instrumental resolution is about 10 nm (Xiong et al., 2006). However, biological samples are characterized with significant morphology and subsequently reduce the instrumental resolution through sample dependent accelerating field aberrations. Thus, the spatial resolution of the PEEM used herein for melanosomes is on the order of tens of nanometers, a resolution far exceeded by other imaging microscopies.

In addition to the lateral resolution, it is necessary to also briefly address the depth of information of PEEM. The depth of information is the distance between the surface and a point at which information from the sample contributes to the image at a specified resolution (Houle et al., 1982). To generate photoelectrons, light that penetrates the sample is absorbed, induces photoionization, and the photoionized electrons are transported to the surface where they then escape from the sample to the vacuum (Habliston et al., 1995). The depth-dependent yield of photogenerated electrons is not known. Estimates for organic materials suggest that electrons are generated within the first 10 nm (Houle et al., 1982). However, it is reasonable to assert that the

yield will decrease with depth from the surface and so while light may be absorbed deep in the sample, the volume relatively near the surface will comprise the dominant contribution to the signal (Griffith and Rempfer, 1988). Furthermore, as melanosomes are effective electron scavengers it is likely that the electrons generated below the surface are efficiently trapped.

2.2.1 Spatial Dependence of the Signal

As previously described, the light source must illuminate the sample at a high incident angle with respect to the surface normal. Consequently, only a portion of the sample surface is directly illuminated because the morphology of the spheroidal melanosomes; the curved side of the specimen facing the incident beam will have a significantly higher photoelectron flux than the opposite side. Given the geometrical considerations, spherical samples will result in an asymmetric photoemission image. The long axis of the sampled image is defined as the axis perpendicular to the incident light. This is the axis that is not influenced by the asymmetry that results from the geometrical constraints of the PEEM and the incident light source (Nepijko et al., 2001).

The three-dimensional topography of biological specimens will also result in photoelectron emission at various angles. Thus, “shapes” revealed in the PEEM image may reflect the interplay between the illumination angle and the surface geometry, not simply the shape of the biomolecule. Emitted electrons possess kinetic energy and the large accelerating potential is used to collect these electrons with a minimum loss of

lateral resolution (Griffith and Engle, 1991). However, spreading or bunching of the emitted electrons results from topographical electric field variations by complex three-dimensional surfaces (Rempfer et al., 1980). As a result, the image may have darker or brighter regions according to the topographic features of the sample. An aperture located in the lens column is used to prevent deflected electrons from reaching the detection area. Deflection of the electrons typically occurs from the sides of a protrusion whereas the electrons arising from surrounding flat regions and the top regions of protrusions pass through the electron-optics system undeflected. Thus, the top regions of protrusions and surrounding flat areas appear brighter while the sides of protrusions are darker.

A two-dimensional image detection (the CCD serves as a two-dimensional image plane, with each pixel having the same area) creates a non-linear distance scale for the image of the melanosome. Consider the projection image of a sphere, **Figure 3a**. The region of a curved three-dimensional surface imaged onto an individual pixel increases with the angle from the surface normal. Therefore, a curved melanosome will further affect the resolution achieved by the instrument. With increasing angle from the surface normal, the photo-ejected electrons initially have increased velocity projections in the plane of the substrate, and fan out with different degrees of curvature prior to being accelerated towards the lens column. As a result, if the accelerating potential is reduced, the size of the image will increase. **Figure 3b** displays the length of the long axis of the

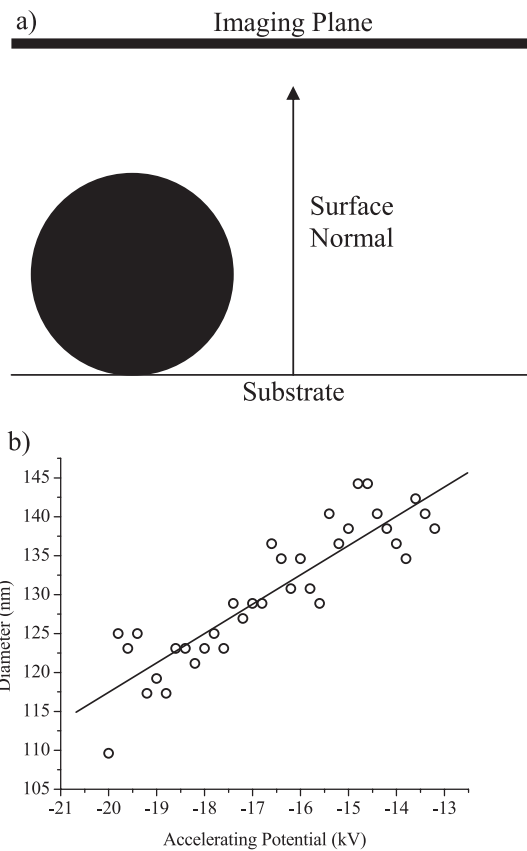


Figure 3: Spatially dependent signal considerations for spherical objects. (a) A three-dimensional sphere projected onto a two-dimensional surface. (b) A plot showing the dependence of the image diameter of a ~150 nm *Sepia* eumelanin granule on the accelerating potential of the instrument.

image of a ~150 nm spherical *Sepia officinalis* eumelanin melanosome (recall that spherical structures appear as ellipsoids) with respect to the accelerating voltage. A linear dependence is observed for the acceleration potential examined. Nepijko has developed a theoretical analysis of such an experiment and provides functional relationships for determining the actual size of the three-dimensional spherical particle from such data (Nepijko et al., 2001).

2.3 Determination of Threshold Potentials²

To acquire the photoionization threshold of an intact melanosome, UV wavelengths are scanned and the integrated brightness of the image is analyzed as a function of the excitation energy (Samokhvalov et al., 2004; Samokhvalov et al., 2005; Bush et al., 2006; Hong et al., 2006; Ye et al., 2006; Garguilo et al., 2007).

2.3.1 Substrate Preparation

Substrates were prepared from $\langle 100 \rangle$ -oriented silicon (N-type, P-doped) purchased from VA Semiconductor, Inc. (Fredericksburg, VA). Sample preparation was initiated by cleaving wafers to square regions of approximately 1 cm². These wafers were cleaned using the standard RCA wet chemical procedure without the hydrofluoric acid step (Senturia, 2001). Isolated melanosomes were suspended in a Nanopure water solution and deposited onto the cleaned silicon wafers in 0.5 μ L aliquots. The samples

²Reproduced in part from: Peles, D. N.; Hong, L.; Hu, D.-N.; Ito, S.; Nemanich, R. J. and Simon, J. D. (2009) *J. Phys. Chem. B*, **113**: 11346-11351, DOI: 10.1021/jp904138n

were allowed to air-dry in a sterile Petri dish before experimentation with care taken to avoid sample exposure to UV light. After drying (< 30 min), the samples were transferred under UHV into the PEEM chamber for data collection. To ensure a large sampling, the instrumental field of view was set at 50 μm . All images were captured with a DVC-1312 M digital camera from DVC Company, Inc. (Austin, TX). The digital camera resolution was 1300 \times 1030 pixels \times 12 bits. Acquisition times were 9 sec.

2.3.2 Excitation Source

The spontaneous emission mode of the Duke UV-free electron laser (FEL) was used to acquire thresholds. Details of the Duke FEL have been described elsewhere (Ade et al., 1998). The FEL was tuned through the spectral range from 240 to 310 nm (5.17 – 4.00 eV) in 5 nm increments.

2.3.3 Measurement Procedure

The measured brightness of the melanosome within the photoelectron image was taken to be proportional to the photocurrent as the emission current cannot be accessed in a standard PEEM. An image was obtained for each wavelength and the melanosome's integrated brightness, S , was measured by a summation of all of the pixel gray scale depths in the selected region. The minimum and maximum gray scale values are regarded as black or white saturated, respectively. Images with a large fraction of the pixel counts located at these values result in a loss of the information regarding the brightness of a melanosome and the photoelectron current is no longer proportional to

the integrated brightness. To ensure the intensity histogram of the image spanned a distribution across the pixel gray scale depths and avoided black and white saturation, the voltage on the multichannel plate and the software gain of the imaging program was adjusted.

Prior to analysis of the threshold curves, standard data corrections were needed for the obtained measurements. The integrated brightness was corrected for the software gain adjustment through the equation:

$$gain(db) = 20 \log_{10} G. \quad (1)$$

To calibrate for the multichannel plate voltage changes on S , PEEM images were collected at fixed wavelength and software gains, but with different voltages. The correction factor was provided by the ratio of S between the two images. Also, because of absorption and the dependence of the incident FEL power on the current in the FEL storage ring, the photon flux of the incident wavelength changed as one scanned through the UV region. This was measured and compensated for with each experiment.

To obtain the photoionization potential of the sample, threshold curves were functionally fit with early theoretical models proposed to explain photoelectric curves. In 1931, Fowler described the photoelectric curve of solid metallic surfaces with an expression that was a function of temperature and the frequency of the incident light (Fowler, 1931). The integrated brightness of the sample, S , proportional to the

photocurrent, I , is in proportion to the product of the square of the temperature of the sample, T , and a function $f(u)$ given by:

$$S \propto I(\chi_0 - h\nu)^{1/2} \propto T^2 f\left(\frac{h\nu - \chi}{k_B T}\right), \text{ where} \quad (2)$$

$$f(u) = e^u - \frac{e^{2u}}{2^2} + \frac{e^{3u}}{3^2} - \dots, \quad (u \leq 0)$$

$$= \frac{\pi^2}{6} + \frac{u^2}{2} - \left[e^{-u} - \frac{e^{-2u}}{2^2} + \frac{e^{-3u}}{3^2} - \dots \right], \quad (u \geq 0).$$

In the above expressions, χ_0 is the threshold potential and χ is the thermionic work function ($\chi = \chi_0 - \varepsilon^*$, where ε^* is the energy of the highest occupied molecular orbital).

Thus, the surface photoionization threshold potentials of melanosomes (discussed in **Chapter 3**) were determined after functionally fitting the threshold curves of S/T^2 vs.

$h\nu/k_B T$. This technique is the same used previously to determine the photoionization threshold potentials of eumelanin and pheomelanin (Samokhvalov et al., 2004;

Samokhvalov et al., 2005; Bush et al., 2006; Hong et al., 2006; Ye et al., 2006; Garguilo et

al., 2007) and while these photoionization threshold potentials are obtained in isolation

and under UHV with PEEM, remarkable consistency has been observed with respect to

how the melanosomes behave under physiologically relevant conditions (Ye et al., 2006).

2.4 Determination of Absorption Coefficients³

The procedure for using the PEEM to directly and quantitatively determine absorption coefficients for single intact melanosomes is established herein.

2.4.1 Substrate Preparation

Two different substrates were utilized in the absorption coefficient calculation. Titanium substrates were used in a single wavelength ($\lambda = 244$ nm) analysis. These substrates were prepared from wafers of $\langle 100 \rangle$ -oriented silicon (P-type, B-doped), purchased from VA Semiconductor, Inc. (Fredericksburg, VA). These wafers were cleaved to square regions of approximately 1 cm² and then cleaned using a simple solvent procedure. Specifically, wafers were added, in subsequent steps, to a trichloroethylene bath, an acetone bath, and a methanol bath for 5 min each. The wafers were then placed on lens paper in a sterile Petri dish and dried with a steady flow of nitrogen gas. Afterward, the cleaned wafers were coated with a thin Ti film (2.5kÅ) using the Kurt J. Lesker PVD 75 E-beam and Thermal Metal Evaporator (Pittsburgh, PA).

Substrates prepared from a wafer of n-type 4H-SiC, purchased from Cree, Inc. (Durham, NC) were used to determine wavelength dependent absorption coefficients and are the predominate substrate used in the studies reported in **Chapters 4** and **5**. The

³ Reproduced in part from: Peles, D. N. and Simon, J. D. (2010) *Photochem. Photobiol.*, **86**: 279-281, DOI: 10.1111/j.1751-1097.2009.00656.x; and Peles, D. N. and Simon, J. D. (2010) *J. Phys. Chem. B*, **114**: 9677-9683, DOI: 10.1021/jp102603b; and Peles, D. N.; Lin, E.; Wakamatsu, K.; Ito, S. and Simon, J. D. *J. Phys. Chem. Lett.*, **1**: 2391-2395, DOI: 10.1021/jz100720h.

wafer was chemomechanically polished by NOVASIC (Le Bourget-du-Lac, France) and cleaved to square regions of 1 cm² by American Precision Dicing, Inc. (San Jose, CA). Individual substrates were then subjected to the same simple solvent cleaning process described for the Ti wafers. Similar to the photoionization threshold sample preparation, isolated melanosomes were suspended in a Nanopure water solution and deposited on the substrates in 0.5 μ L aliquots immediately prior to experimentation. The samples were air-dried (< 30 min) with minimal exposure to UV light and subsequently transferred under UHV into the PEEM chamber for data collection. To ensure a large sampling, melanosomes were imaged at fields of view of 150 μ m.

2.4.2 Excitation Source

An intracavity doubled Ar⁺ ion continuous wave laser was used to illuminate the sample at $\lambda = 244$ nm for preliminary investigations on Ti and later for purposes of finding and focusing the sample prior to wavelength scans on SiC with the tunable laser source. Laser excitation utilized for the wavelength dependent absorption experiments was provided by a solid-state tunable nanosecond laser system from Opotek, Inc. (Carlsbad, CA). Data was collected at the following wavelengths: 244 nm (5.08 eV), 257 nm (4.82 eV), 270 nm (4.59 eV), 280 nm (4.43 eV), 290 nm (4.28 eV), 300 nm (4.13 eV) and 310 nm (4.00 eV). The polarization of the light was parallel to the plane of incidence. To avoid noted space-charge effects (Buckanie et al., 2009) and physical disruption of the melanosomes (Glickman et al., 1996) resulting from pulsed laser sources, a neutral

density filter was inserted in the beam path to reduce the average laser power. The maximum pulse energy, after the neutral density filter, was at most 12 mJ/cm² for $\lambda = 244$ nm and decreased at longer wavelengths. The maximum pulse energy used herein is < 10% of the previously calculated photodisruption threshold of 153.6 mJ/cm² for melanosomes (Glickman et al., 1996). At each wavelength, laser power and optical alignment were optimized prior to acquisition of the digital image. All images were captured with a cooled DVC-1500 M digital camera from DVC Company, Inc. (Austin, TX) with a resolution of 1392 x 1040 pixels x 12 bits. As a result of varied laser power across wavelengths, the acquisition times were 5, 7, 14, 28, 42, 50 and 50 min for $\lambda = 244, 257, 270, 280, 290, 300$ and 310 nm, respectively.

2.4.3 Measurement Procedure

For reasons provided below, the Ti and SiC substrates were purposely utilized as their work functions are lower in energy than that of the associated incident light at the single wavelength $\lambda = 244$ nm and through the UV wavelengths examined (5.07 eV at 244 nm and 4.00 eV at 310 nm). As a result, at shorter wavelengths, both the substrate surface and the melanosomes emit electrons and are imaged by the microscope. The melanosomes have a higher efficiency for ionization (electrons per area) than the substrate and are subsequently easily distinguished in the image.

The approach for determining the absorption coefficients is shown schematically in **Figure 4**. As previously described, laser light was focused on the sample at a high

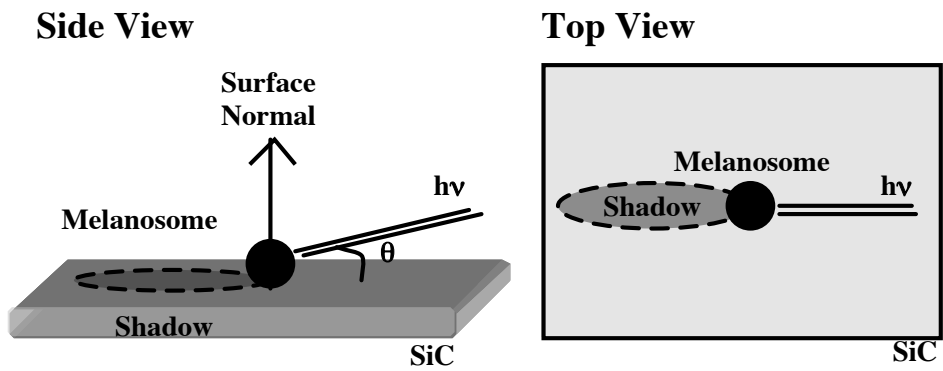


Figure 4: Experimental geometry for PEEM of single melanosomes. Laser excitation hits the melanosome at an angle of incidence of approximately 77° with respect to the surface normal. Light is attenuated and a shadow is generated on the far side of the melanosome.

angle of incidence ($\sim 77^\circ$ with respect to the surface normal). As light travels through the melanosome, absorption attenuates its intensity, causing a reduction in the photoemission of the substrate immediately behind the melanosome, and a shadow is visualized as a result. However, as simulated in **Figure 5**, illumination of an ellipsoidal object with dimensions comparable to a melanosome produces significant scattering of the electric field. Consequently, the absorptive properties of the melanosomes, which are manifested by changes in the image intensity of the substrate, are determined from the region of the substrate immediately behind the melanosome that is void of significant scattering contributions.

Because the molecular structure of melanin is not known, pigment absorption coefficients are represented by the product ϵc , where ϵ is the extinction coefficient and c is the concentration. The Beer-Lambert Law defines ϵc through the following equation:

$$\epsilon c = A \ell^{-1} = \ell^{-1} \log(I_0/I) \quad (3)$$

with units of inverse length. As shown, the calculation of ϵc requires knowledge of the pathlength, ℓ , and the incident and transmitted intensities of light, I_0 and I , respectively. The values of I_0 and I are derived from the PEEM image; an average of the photoemission current of the substrate, where there is no obstruction by absorbing melanosomes gives I_0 , and an average of the photoemission current of the shadow region adjacent to the melanosomes gives I .

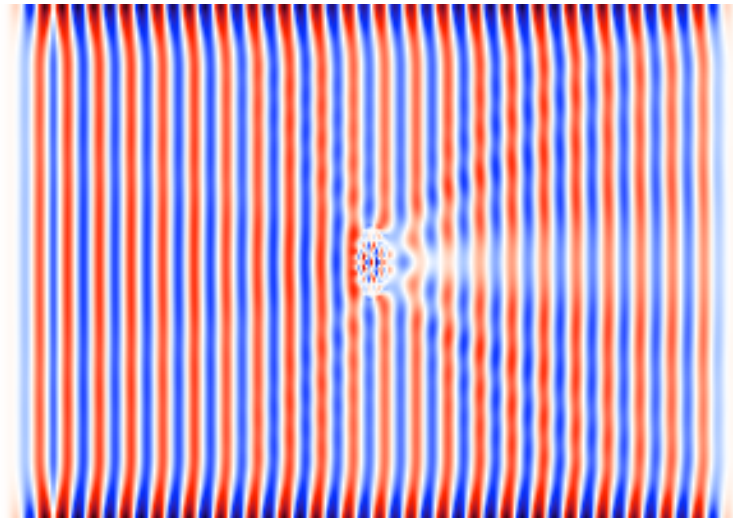


Figure 5: A top view (x-y dimension) simulation of the interaction of electromagnetic radiation with an ellipsoid. The interaction was simulated with $\lambda = 244$ nm light and the model ellipsoid was characterized with a refractive index of 3.4. The dimensions of the ellipsoid are comparable to the melanosomes studied in this thesis (260 nm x 560 nm). Simulations of the electromagnetic field were performed with the finite-difference time-domain method (Taflove and Hagness, 2000) using a freely available software package (Oskooi et al., 2010). The colors reflect the peaks and valleys of the electromagnetic radiation.

2.4.3.1 Disaggregating Absorption and Scattering

To disaggregate the effects of absorption and scattering within the shadow region, the portion of the shadow region that is void of significant scattering contribution was determined. Following the methodology outlined by Chelaru et al. (Chelaru et al., 2006), diffraction will influence the intensity in the shadow region beginning at a distance from the melanosome corresponding to the first maximum in the diffraction pattern of regular Fraunhofer diffraction. Note, according to Babinet's principle, the Fraunhofer diffraction pattern for an opaque object is the same as it is for an aperture of the same shape except that the intensity distributions are inverted (Guenther, 1990). Thus, calculating the dimensions of the first maximum diffraction disk from an elliptical aperture is equivalent to the dimension of the first minimum diffraction disk observed for opaque ellipsoidal melanosomes.

The intensity distribution for the illumination of an elliptical aperture with coherent plane waves is described by

$$I \propto \left[\frac{J_1(x)}{x} \right]^2, \quad (4)$$

where $J_1(x)$ is a first-order Bessel function and $x = 2\pi a \varepsilon p / \lambda z$, $2a$ is the length of the major ellipsoidal axis of the melanosome, ε is the ellipsoidal axial ratio (b/a), p is the radius of the diffraction pattern produced on the plane of observation, z is the distance between the aperture and the plane of observation and λ is the wavelength of the incident light (Kathuria, 1985). The first maximum of the diffraction pattern

corresponds to the first zero of the function $J_1(x)$, occurring at $x = 3.83166 (m_0)$. Thus, the dimension of the first maximum observed on the plane of observation can be expressed as

$$p = \frac{\lambda m_0 z}{2\pi a \epsilon} . \quad (5)$$

This expression then gives the distance in the shadow region from the melanosome that is void of any significant contribution from scattering, and thereby defines the region from which the absorption coefficient is calculated. Under the experimental geometry, z is equivalent to $2b/\tan(\alpha)$ where $2b$ is the length of the minor axis of the ellipse (the height of the melanosome from the surface plane) and $\alpha = 13^\circ$, the angle between the surface plane and the incident light. As expected this region is contained within the first diffraction ring that is visible in the obtained images and it is this region through which the average photoemission current is subsequently determined. Specifically, the upper threshold values of the image were set to visually segment the image into shadow and substrate features. Each region was reduced to an average value by averaging the intensities of the included pixels. These values, taken with the calculated average pathlength, are then used to determine the absorption coefficients.

2.4.3.2 Pathlength Calculation

In principle, the spatial dependence of the photoemission current of the shadow maps directly onto the different pathlengths through the melanosome. In practice, however, it is only possible to precisely know the dimensions of the melanosome to

within a few tens of nm, the resolution of the PEEM. This uncertainty covers the majority of the range of the size distribution of the melanosomes as determined by SEM in **Chapter 3** and in (Liu et al., 2005b), and so the following approach was developed to determine ℓ from average SEM values for the melanosome dimensions.

SEM characterization of the ocular melanosomes examined in **Chapters 4** and **5** reveal ellipsoidal morphologies, **Chapter 3** and (Liu et al., 2005b). As a result, points in the shadow correspond to different chord lengths through the ellipsoid. To compute the absorption coefficient, an average ℓ is calculated and used in **Equation 3** along with the average photoemission intensity obtained from the shadow and the unobstructed substrate regions. The average ℓ calculation is derived as follows. Consider an ellipsoid described by:

$$\frac{x^2}{a^2} + \frac{y^2}{b^2} + \frac{z^2}{c^2} = 1, \quad (6)$$

where a and b are the equatorial radii along the x - and y -axes, respectively (in the plane of the substrate), and c is the polar radius along the z -axis (normal to the substrate), **Figure 6**. Solving this equation for y produces two functions that correspond to the two parabolas of a 2-D horizontal ellipse at a height, z , shown in **Figure 6**. The distance, s , between points on each parabola as a function of x and z can thus be calculated from

$$s(x, z) = 2[b^2 - (b^2 x^2 / a^2) - (b^2 z^2 / c^2)]^{1/2}. \quad (7)$$

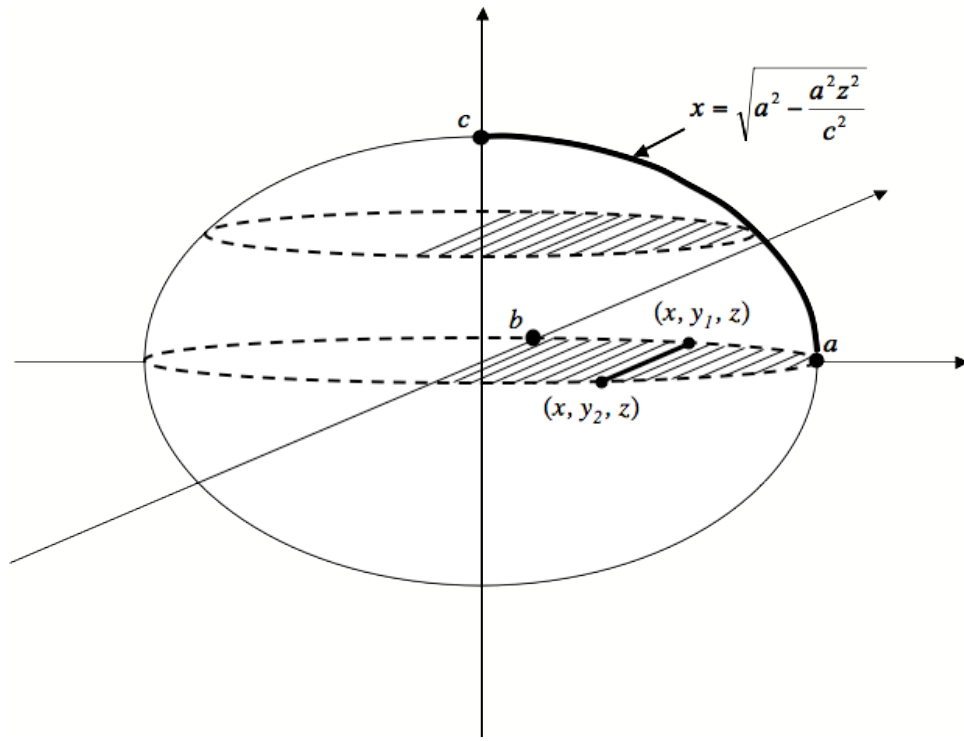


Figure 6: Geometrical model of an ellipsoid with dimensions a , b , and c . Parabolas are diagramed within the ellipsoid as the two halves of the dashed 2-D ellipses. An example of a single chord distance, s , is highlighted in black between the points (x, y_1, z) and (x, y_2, z) . The equation for the highlighted curvature of a melanosome along the x -axis is shown.

To find the average distance (ℓ) of all of the different chord lengths, s , within the collection of 2-D ellipses that make up the ellipsoid, integration, with appropriate bounds, is required. Consider, the 2-D ellipse at height $z = 0$. Here, the range can be limited to $[0, a]$ in the x -axis (by symmetry, the range can be limited to a instead of $2a$). However, as the height, z , changes for each 2-D ellipse, the range must be limited to the radius of that particular slice along the x -axis. Thus, with the range $z \in [0, c]$, it must be that $x \in [0, [a^2 - (a^2 z^2)/c^2]^{1/2}]$ to account for the curvature of the ellipsoid.

Using these bounds, the average pathlength of an ellipsoid is given by

$$\ell = \frac{\int_0^c \int_0^\tau s(x, z) dx dz}{\int_0^c \int_0^\tau dx dz}, \quad (8)$$

where $\tau = [a^2 - (a^2 z^2)/c^2]^{1/2}$. It must be noted, however, that portions of the analyzed shadow regions generally map onto pathlengths that extend beyond half of the volume of the melanosome, but not the entire melanosome, due to the geometry of the experiment. The polar distance, ξ , that extends below $z = 0$ and accounts for the additional pathlengths associated with the shadow region, can be obtained directly from the PEEM image. Once ξ is determined, the averaged experimental pathlength is calculated by integrating Equation 4 with the integration bounds $z \in [\xi, c]$ and $x \in [-\tau, \tau]$.

The above analysis is accurate for ellipsoids whose long axis is oriented perpendicular to the direction of incident light. However, in a typical sample,

melanosomes are oriented at random angles with respect to the direction of incident light. Unfortunately, many of the melanosomes examined are characterized with small dimensions and aspect ratios and determination of the angle between the long axis of the ellipsoid and the incident light is difficult to achieve with reasonable accuracy in the PEEM images. In this limit, the average pathlength is calculated by assuming the melanosomes are oriented perpendicular to the direction of incident light. This is a reasonable approximation; as the aspect ratio decreases, the melanosomes approach a spherical shape. In the case of the RPE eumelanosomes, however, the aspect ratio is such that the orientation of the melanosomes can be determined from the PEEM image. In this instance, it is necessary to take into account the angle between the incident light and the long axis of the melanosome. The modeled melanosome, originally oriented perpendicular to the incident radiation, is rotated in a counter-clockwise rotation around the z -axis by θ radians through variable substitution

$$\begin{aligned} x &= X \cos(\theta) + Y \sin(\theta) \quad \text{and} \\ y &= Y \cos(\theta) - X \sin(\theta). \end{aligned} \tag{9}$$

The chord lengths through the rotated melanosome are then described by

$$s(X, z, \theta) = 2\{[a^2 b^2 [-c^2 X^2 \cos(\theta)^4 + \cos(\theta)^2 [a^2 (c^2 - z^2) - 2c^2 X^2 \sin(\theta)^2] - \sin(\theta)^2 [b^2 (-c^2 + z^2) + c^2 X^2 \sin(\theta)^2]]] / [c^2 [a^2 \cos(\theta)^2 + b^2 \sin(\theta)^2]^2]\}^{1/2}. \tag{10}$$

Note that in this orientation, the major radius no longer lies along the x -axis, and as a consequence, the upper limit of the integration bounds for the X -variable becomes

$\tau_2 = \{[(c^2 - z^2)[a^2 \cos(\theta)^2 + b^2 \sin(\theta)^2]] / c^2\}^{1/2} / \{[\cos(2\theta)]^2\}^{1/2}$. Thus, the average ℓ for half of the volume of a rotated ellipsoidal melanosome is

$$\ell_{rotated} = \frac{\int_0^c \int_0^{\tau_2} s(X, z, \theta) dx dz}{\int_0^c \int_0^{\tau_2} dx dz} . \quad (11)$$

Once again, ξ can be obtained directly from the PEEM image, and then, the limits of the integrals in **Equation 11** are adjusted accordingly.

3. Structural and Morphological Analysis of Human Iridal Stroma Melanosomes¹

3.1 Introduction

The photoreactivities of melanins are generally described as photoprotective and antioxidant for eumelanin and photoreactive and pro-oxidant for pheomelanin (Chedekel et al., 1978; Harsanyi et al., 1980; Persad et al., 1983; Takeuchi et al., 2004; Ye et al., 2006). Furthermore, as the epidemiology of skin cancer and uveal melanoma indicates an observed increased incidence for increased relative concentrations of pheomelanin, the eumelanin:pheomelanin ratio within naturally occurring melanosomes is often discussed as a biologically significant marker (Vincensi et al., 1998; Wenczl et al., 1998b; Wakamatsu et al., 2007; Hu et al., 2008). The fact that pheomelanin has a lower ionization potential than eumelanin is also supportive of the view that pheomelanin could be an active contributor to the greater incidence rate of UV-induced cancers (Ye et al., 2006). Upon comparison of the threshold ionization energies assigned to eumelanin (282 nm) and pheomelanin (326 nm) with the solar irradiance at the Earth's surface for several different solar zenith angles, it is observed that one is exposed to wavelengths of

¹ Reproduced in part from: Peles, D. N.; Hong, L.; Hu, D.-N.; Ito, S.; Nemanich, R. J. and Simon, J. D. *J. Phys. Chem. B*, **113**: 11346-11351, DOI: 10.1021/jp904138n; and Simon, J. D. and Peles, D. N. *Acc. Chem. Res.*, **43**: 1452-1460, DOI: 10.1021/ar100079y

light that are sufficient to ionize pheomelanin, but that the atmosphere nearly completely blocks the light required to photoionize eumelanosomes (Ye et al., 2006).

For pheomelanin to be active in inducing such oxidative stress in natural systems, however, it must be present on or near the surface of the melanosomes. If the pheomelanin is present in the core of melanosome, then it is highly unlikely that photoionization will lead to electrons that can escape the organelle. This becomes even more improbable upon consideration of the excellent scavenging properties of eumelanin. Thus, determination of the pigment composition at the surface of mixed melanic melanosomes is of biological importance. Understanding whether or not the morphology of mixed melanins is such that pheomelanin lies at the core may provide insight into the balance of the dichotomy of the pigments and the possible roles melanosomes may play in the molecular mechanisms of cutaneous and uveal melanoma.

The melanogenesis of the two pigments is described by the Raper-Mason scheme, **Figure 1**. Applying data from pulse radiolysis studies reported by Tad Land and Patrick Riley (Land and Riley, 2000; Land et al., 2003), Ito and co-workers were able to quantify kinetics for several steps of the Raper-Mason scheme (Ito, 2003; Ito and Wakamatsu, 2008). The data indicate that one can think of the synthesis of melanins in terms of a 3-step process. Initially cysteinyl-dopa formation will occur to the exclusion of eumelanin synthesis, as long as the concentration of cysteine is greater than 0.13 μM .

Second, oxidation of cysteinyl-dopa to pheomelanin occurs for concentrations of cysteinyl-dopa greater than 9 μM . Finally, eumelanin is generated – occurring after most of the cysteinyl-dopa and cysteine levels are depleted. While there are no studies that provide a real time view of melanin formation within the melanosome, electron microscopy of melanosomes at differing degrees of melanization indicate that pigment granules gradually grow to diameters of ~ 30 nm within the melanosome, and once they reach this size, no free space can be detected (Liu and Simon, 2003; Simon et al., 2008). Given this morphology, the 3-step process characteristic of samples containing both pheomelanin and eumelanin would predict a structural motif where the ~ 30 nm granule would have pheomelanin at their core and eumelanin at the surface. This type of molecular structure has been previously proposed based on biochemical studies of mixed melanogenesis and solubility properties of synthetic model systems (Agrup et al., 1982; Ozeki et al., 1997a). However, despite the compelling evidence presented from the *in vitro* studies, direct evidence supporting a “casing model” architecture for mixed melanic melanosomes isolated from the skin or uvea has not been reported.

Because different photoionization thresholds characterize the two pigments, PEEM imaging of the melanosome surface can uniquely determine whether or not both pigments comprise its surface. Melanosomes isolated from the stroma of human irides are an optimal system for such a study as different colored irides contain melanosomes of varying eumelanin:pheomelanin ratios (Wakamatsu et al., 2007). This system

presents the opportunity to investigate the surface photoreactivity as the relative pheomelanin concentration changes through a single type of human melanosome with wavelength-dependent PEEM imaging.

3.2 *Materials and Methods*

3.2.1 Sample Isolation

Extraction of the iris was performed on donor eyes from two patients of different colors and ages, dark brown, age 14, and blue-green, age 66. The posterior IPE was isolated from the iris with a previously described method (Prota et al., 1998), and the remaining IPE-scraped iris tissues were stored at -70 °C until further use. An enzymatic extraction was used to isolate the iridal stroma melanosomes from the iris tissue using the same procedure as that reported on melanosome isolation from bovine iris (Liu et al., 2005b). Briefly, wet iris tissue was cut into small pieces and subjected to three steps of enzyme digestions at 37 °C in PBS under argon, collagenase (68 U/mL, with 2 mM CaCl₂) for ~16 h, pancreatin (2.5 mg/ mL) for 2 h, and trypsin (646 U/mL, with 2 mM CaCl₂) for 2 h. After each digestion, the remaining material was washed with water several times and then subsequently subjected to further enzyme digestions. Following these treatments, the materials were suspended in 1% (wt/vol) Triton X-100 solution and stirred for 1.5 h at room temperature under argon. The particles were then washed with methanol/water 1:1 (vol/vol) once and then with water four times. Afterward, the pellets were treated with collagenase (68 U/mL, with 2 mM CaCl₂) for 16 h at 37 °C

under argon. The resulting black to brown melanosomes were washed with water five times and kept at -70 °C until use.

3.2.2 Scanning Electron Microscopy

Melanosomes were suspended in a water suspension and dropped onto freshly cleaved mica slides in 2 μ L aliquots. The slides were then mounted on stainless steel pegs with double stick tape and air-dried in the dark. The mounted samples were coated with Au/Pd under argon plasma for 2 min at 15 mA using a Hummer V sputter coater (Anatech, Springfield, VA). A Philips XL30 ESEM (FEI company, Hillsboro, OR) equipped with a backscattering secondary electron detector was used to examine the samples in high vacuum mode. Multiple SEM images were captured at magnifications of 10,000 \times for each of the different samples. Care was taken to ensure that each image collected covered a completely different surface area. The dimensions of the melanosomes captured in the SEM images were measured using Scandium Imaging Software (Olympus Soft Image Solutions, Lakewood, CO). For each sample, over 1500 granules were measured from 6 to 14 images taken at 10,000 \times magnification. The histograms of the lengths of the short and long axes of the measured melanosomes were plotted and fit to a single Gaussian function.

3.2.3 Free Electron Laser-Photoemission Electron Microscopy

The photoionization thresholds of the samples were analyzed with the same procedures as described in **Chapter 2**.

3.2.4 Atomic Force Microscopy

A water suspension of iridal stroma melanosomes was pipetted in 0.5 μL aliquots onto freshly cleaved mica and allowed to air-dry in the dark. The instrument and method of imaging has been previously described in detail (Clancy and Simon, 2001). Briefly, AFM height and phase images were collected with a NanoScope IIIa BioScope AFM (Digital Instruments, Santa Barbara, CA) operated in tapping mode. The AFM head was mounted on a Zeiss (Thornwood, NY) Axiovert S100 TV inverted optical microscope, allowing visual observation of the sample.

3.3 Results and Discussion

3.3.1 Shape and Size Analysis of Iridal Stroma Melanosomes

SEM imaging was used to analyze the morphology of blue-green and dark brown iridal stroma melanosomes from donors of age 66 and 14, respectively (**Figure 7**). The shape and size observed in the analysis revealed a consistent morphological distribution across samples regardless of their respective age or iris color origins. The long and short axes of the melanosomes were measured from these images, and the resulting histograms were fit to a single Gaussian function, **Figure 8**. The outcomes of the fitting are given in **Table 1**. The morphology revealed for these iridal stroma melanosomes by SEM is in agreement with previously reported morphological results on iridal stroma melanosomes by TEM (Hu et al., 1992; Hu et al., 1993).

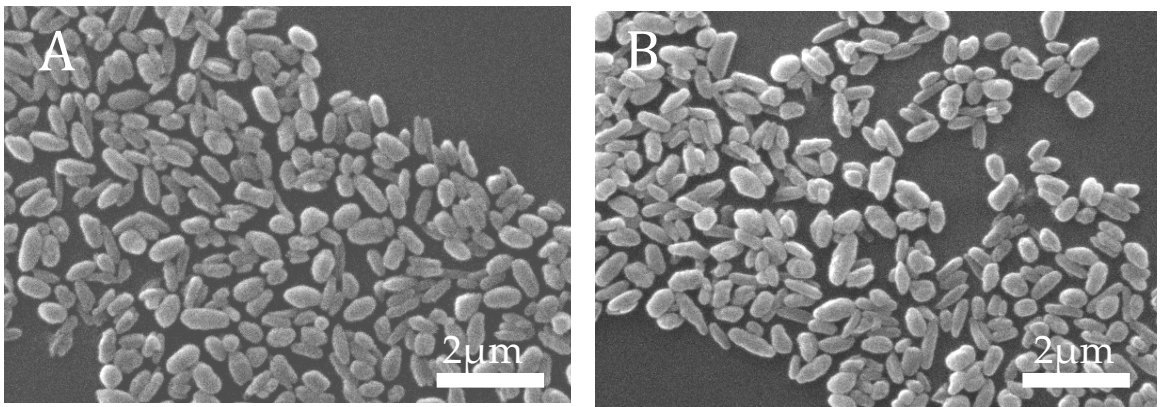


Figure 7: SEM images of (A) dark brown iris melanosomes and (B) blue-green iris melanosomes.

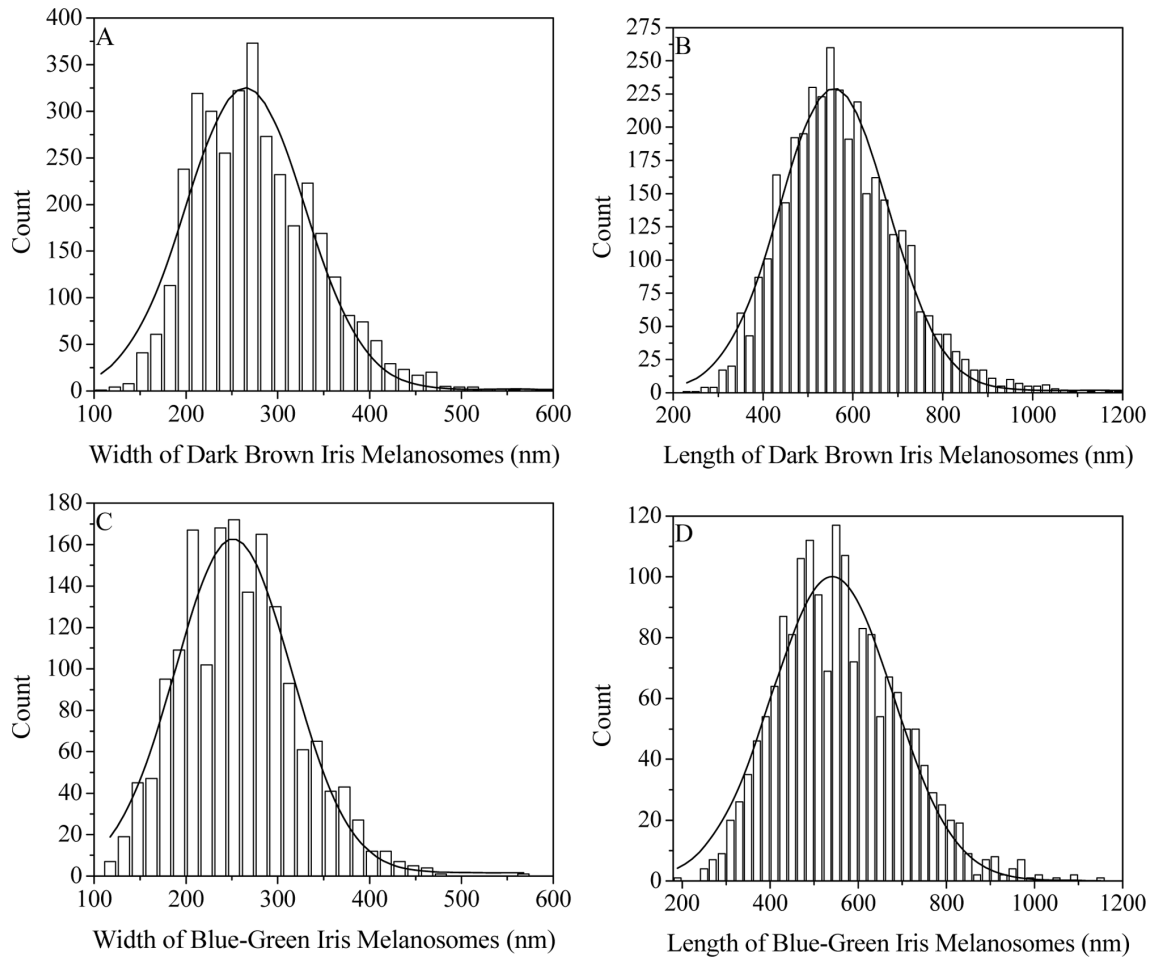


Figure 8: The distributions of the widths and lengths of dark brown iris melanosomes (A, B) and blue-green iris melanosomes (C, D). As shown, the distributions of lengths of the long and short axes are represented by single Gaussian distributions.

Table 1: Summary of the size analysis of the melanosomes isolated from human irides. The error in measuring the dimensions is < 5%. The histograms of the lengths of both the long and short axes were fit to a single Gaussian function. The peak of the distribution is tabulated. The half-width of the distribution is given in parentheses.

| Iris Color | Length/nm | Width/nm |
|------------|-----------|----------|
| Dark Brown | 560 (140) | 260 (80) |
| Blue-Green | 540 (160) | 250 (70) |

During the sample preparation, the IPE is carefully removed from the posterior surface of the iris. However, complete dissection of the IPE is nearly impossible to achieve, and the anterior IPE remains tightly bound to the iris tissue (Prota et al., 1998). As a consequence, melanosomes isolated from this “IPE-scraped” iris tissue comprise those from anterior IPE and iridal stroma. Morphologically, the IPE melanosomes are spherical, with an average diameter of 1.02 μm , whereas the iridal stroma melanosomes are smaller, ovoid-shaped organelles with width and length dimensions of 0.25 and 0.64 μm , respectively (Hu et al., 1992; Hu et al., 1993). The SEM size distributions results revealed a morphology that is consistent with previously reported dimensions for iridal stroma melanosomes (**Figure 8**). Additionally, the representative SEM images shown in **Figure 7** illustrate the dominance of ovoid shapes rather than larger spheres. From the size and shape analysis of the melanosomes isolated from the blue-green and dark brown irides, it is concluded that the samples are dominated by iridal stroma melanosomes rather than anterior IPE.

3.3.2 Surface Photoionization Potentials of Iridal Stroma Melanosomes

The surface composition of melanosomes isolated from dark brown and blue-green iridal stroma tissue was examined using FEL-PEEM. The integrated intensity (S) of the PEEM images was determined as a function of the excitation wavelength generated by the FEL and the acquired data from individual melanosomes was functionally fit. Despite the fact that melanosomes isolated from the iridal stroma tissue

contain both eumelanin and pheomelanin in varying ratios depending on iris color (Prota et al., 1998; Wakamatsu et al., 2007), an analysis of the plots generated with the FEL-PEEM technique for dark brown and blue-green iridal stroma melanosomes revealed data that was best fit by a single photoionization threshold of 4.9 ± 0.2 eV (253 nm) (**Figure 9**). This threshold was attributed to eumelanin since it is comparable to the eumelaninic threshold established in previous reports on purely eumelaninic systems (e.g., *Sepia* ink and black hair melanosomes) (Ye et al., 2006; Garguilo et al., 2007). For reference, the pheomelanin threshold is characterized as 3.8 ± 0.2 eV (326 nm) from comparison studies on red hair melanosomes (Ye et al., 2006). Consistent with this conclusion is our inability to obtain PEEM images on iridal stroma melanosomes using a wavelength that clearly photoionizes pheomelanin in red hair melanosomes. These results suggest that despite the color origin of the melanosome, only eumelaninic components are present on or near the surface.

3.3.3 Morphological Surface Organization of Iridal Stroma Melanosomes

A more detailed view of the surface of the melanosomes is obtained with the AFM images (**Figure 10**). The height and phase images for dark brown iridal stroma melanosomes reveal that the surface is comprised of smaller substructures. This result was expected based on previous studies of naturally occurring pigments isolated from various sources (Clancy and Simon, 2001; Liu et al., 2005a; Liu et al., 2005b; Hong et al., 2006). All of the pigments reveal smaller substructures with lateral dimensions of a few

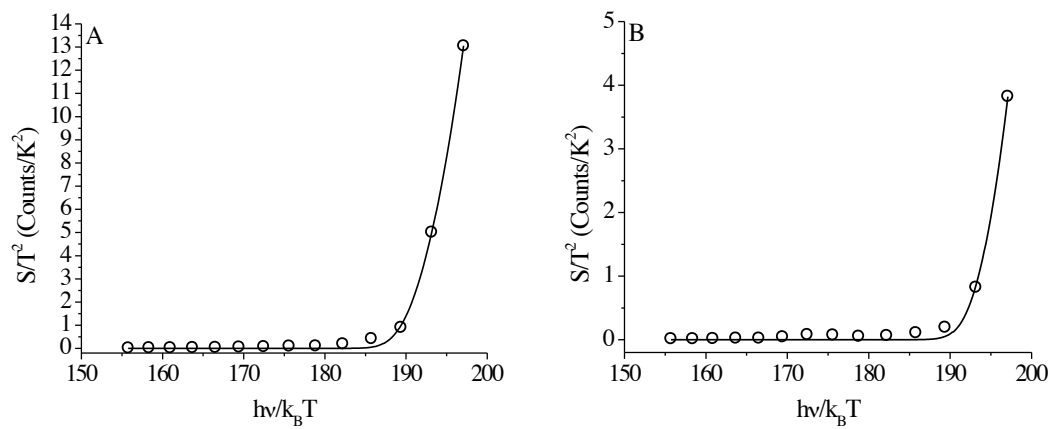


Figure 9: Integrated wavelength-dependent FEL-PEEM data for A) dark brown iridal stroma melanosomes and (B) blue-green iridal stroma melanosomes.

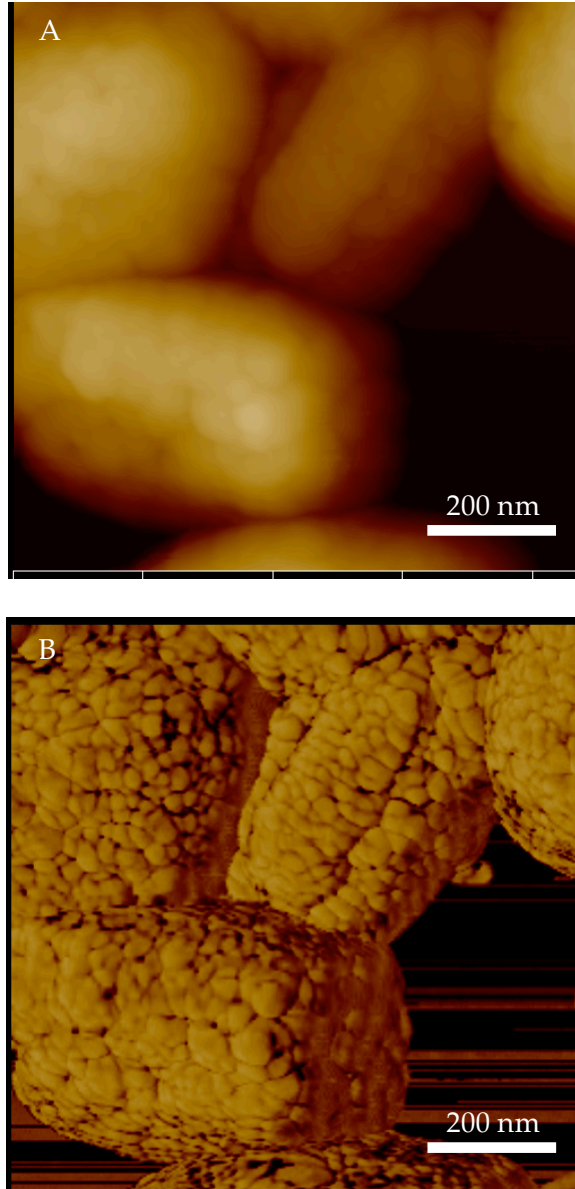


Figure 10: AFM images of dark brown iridal stroma melanosomes. The small substructures of the iridal stroma melanosomes are observed in both A) the height image and B) the phase image.

tens of nanometers. These results are additionally consistent with the view of melanogenesis proposed by Brumbaugh in the late 1960s (Brumbaugh, 1968). In that report, Brumbaugh showed that eumelanin premelanosomes comprise zigzagging longitudinal strands with cross-links that occur every 200 Å. Further analysis of the electron micrographs during the final stages of melanogenesis revealed melanin deposition occurring around and upon these matrixes. As a result of the studies, the FEL- PEEM technique would be probing the surface of these smaller substructures along the surface. Thus, it is concluded that these substructures found along the surface of the iridal stroma melanosomes all have eumelanin coats.

Kinetic studies of the initial steps of the Raper-Mason scheme for melanogenesis established the branching between eumelanin and pheomelanin production. Although initiation of the formation of each pigment is achieved by the enzymatic oxidation of tyrosine by tyrosinase, the kinetic data suggests a three-step process for melanogenesis following this oxidation (Land and Riley, 2000; Ito, 2003; Ito and Wakamatsu, 2008). First, the initial production of cysteinyl-dopa occurs when the cysteine concentration is greater than 1.3 μM . Then, when the cysteinyl-dopa concentration is greater than 9 μM , subsequent oxidation of cysteinyl-dopa to pheomelanin occurs. It is only after the depletion of most of the cysteinyl-dopa and cysteine levels that eumelanin formation occurs. These kinetic results suggest a structural design with a pheomelanin core encased by a eumelanin exterior. Studies on the biochemistry of mixed melanogenesis

(Agrup et al., 1982) and the solubility properties of synthetic model systems (Ozeki et al., 1997a) also proposed this bimolecular casing model. As both of the colored iridal stroma melanosomes analyzed displayed characteristics of pure eumelanin on the surface, the FEL-PEEM results provide strong evidence for the casing model in human iridal stroma melanosomes.

A chemical analysis investigating the relationship between the amount and type of melanin and iris pigmentation was recently described in the literature (Prota et al., 1998; Wakamatsu et al., 2007). For different colored irides, the amount of pheomelanin remained fairly constant, while the eumelanin component increased in darker-colored irides. As result of the casing model and the FEL-PEEM results, the presence of a relatively constant pheomelanic “core” with a varying eumelanic exterior is proposed for colored iridal stroma melanosomes. The variation of the thickness of the eumelanic shell is attributed to the difference of the eumelanin:pheomelanin ratio. In lighter-colored irides (blue, hazel, etc.), melanosomes have a low eumelanin:pheomelanin ratio, and subsequently, a thin eumelanic shell is expected. On the other hand, darker-colored irides, which possess significantly higher eumelanin:pheomelanin ratios, are expected to have a thick eumelanic exterior.

From the report published recently by Wakamatsu et al., the eumelanin:pheomelanin ratios for uveal melanocytes from eyes with blue-green (hazel) and dark brown irides are identified as 1.3 and 14.8, respectively (Wakamatsu et al.,

2007). Using these ratios, conclusions can be drawn about the variation of the thickness of the eumelanic coats. Specifically, calculations show that the eumelanin exterior is 2.48 times thicker for dark brown irides than that for hazel irides, assuming the density of the subunits remains constant for both colors. If we model the substructure of the melanosomes as spheres of diameter 30 nm, the eumelanic exterior would be ~9 and 3.6 nm thick for the dark brown and blue-green iridal melanosome, respectively, and the corresponding diameter of the pheomelanin cores would be ~12 and 22.8 nm, respectively. As described in **Chapter 2**, the electron escape depth for melanosomes is expected to be a few nanometers; thus, the absence of the pheomelanin signature is not surprising despite the thin eumelanic shell.

The photoreactivity of the melanin pigment within the melanosome becomes important as a consequence of these results. A dark-colored iris with lower relative pheomelanin concentration (high eumelanin:pheomelanin ratio) is presumed to have a thick eumelanic exterior. Therefore, after the oxidation of the surface pigment, there is still a large amount of eumelanin that can be protective against oxidative stress. However, in melanosomes from light-colored irides, after the oxidation and degradation of the eumelanic surface, a certain amount of pheomelanin molecules are exposed and show their pro-oxidant properties, causing tissue damage. These results are consistent with the incidence of uveal melanoma in different races and in eyes from different colored irides. Epidemiological studies on the relationship between iridal color and

incidence of uveal melanoma suggest that the light-colored eye (blue, hazel, etc.) and Caucasian is at a higher risk than the dark-colored eye and African-Asians (Michelson and Shields, 1977; Tucker et al., 1985; Holly, 1990; Seddon et al., 1990; Vajdic et al., 2001; Hu et al., 2005). Subsequent exposure of the photoreactive and pro-oxidant pheomelanin coupled to the lower total amount of melanin in lighter-colored irides could be a contributor to the observed epidemiology of uveal melanoma.

It is interesting to consider the potential implications of these findings. While ocular melanosomes have been the focus herein, it has previously been established that a similar encapsulation of pheomelanin by eumelanin pigments is characteristic of the neuromelanin granules isolated from various regions of the human brain (Bush et al., 2006; Ito, 2006; Bush et al., 2009). This suggests that the structure of melanosomes containing both classes of pigments may share a common structural morphology, independent of tissue type. A recent study on the eumelanin and pheomelanin content in uveal melanoma cells found that melanoma cells have a very low eumelanin content and eumelanin:pheomelanin ratio, significantly lower than that from normal melanocytes. These differences likely render melanoma cells more susceptible to mutagenic effects of UV radiation and oxidative stress and may enhance their proliferation, thereby accelerating the progression of melanoma (Hu et al., 2009). Epidemiological studies indicate that the incidence of cutaneous melanoma in individuals with light-colored skin is greater than that from individuals with dark-

colored skin. The relative risk of white/black varies from 12.6 to 17.1 in different reports (Neugut et al., 1994; Cress and Holly, 1997; Tsai et al., 2005). Studies of eumelanin and pheomelanin content of epidermal melanocytes from different donors indicate that the eumelanin:pheomelanin ratio correlates with the color of the skin and the ethnic background of the donors. Melanocytes from dark-colored skin and African- American donors have a greater amount of eumelanin and a high ratio of eumelanin:pheomelanin as compared to that with lighter-colored skin and Caucasian (Wakamatsu et al., 2006). If the melanosomes in uveal melanoma cells and epidermal melanocytes have a similar structure as that in iridal melanocytes melanosomes, the different incidence of cutaneous melanoma in individuals with various colored skins and the progress of uveal melanoma could be explained, at least partly, by the structure of melanosomes and the different thicknesses of eumelanin coats.

3.4 Conclusions

The surface potentials of iridal stroma melanosomes from human dark brown and blue-green irides have been studied with FEL-PEEM, and further analysis of the surface morphology was probed with AFM. All melanosomes show pure eumelanin on their surfaces, independent of their respective eumelanin:pheomelanin ratios. These results provide very strong evidence for the casing model in the human irides and imply that the smaller substructures all have eumelanin coats of varying thickness. This result provides new insights into the molecular mechanisms underlying the epidemiology of

uveal melanoma. As the reactive pheomelanin is encased by the photoprotective eumelanin, degradation of the eumelanic exterior is necessary to expose the pro-oxidant, photoreactive properties of the pheomelanic core. Degradation of the eumelanic surface can be achieved through several processes (photobleaching, oxidation), but exposure of the pheomelanic core will result more quickly in lighter-colored irides with thinner eumelanic shells. These results are consistent with the epidemiological studies, which show that the incidence of uveal melanomas is greater in Caucasian and in eyes with light-colored irides. Further studies are needed, however, to confirm that the outer protective layer thins with the lightening of the color of the iris.

4. Ultraviolet Absorption Coefficients of Bovine Ocular Melanosomes Containing Eumelanin¹

4.1 Introduction

The eumelanin contained within cutaneous and ocular melanosomes has been identified as having a variety of functions, but it is the role of photoprotection that is often the most cited (Kollias et al., 1991; Sarna, 1992; Meredith and Sarna, 2006). Central to understanding the photochemical properties of eumelanosomes, melanosomes predominately comprised of eumelanin, is a direct measurement and thorough description of their absorption coefficients. Within darkly colored mammalian eyes, eumelanosomes are contained in several layers of pigmented tissues, including the choroid, iris and RPE (Dryja et al., 1979; Liu et al., 2005b; Hu et al., 2009). As discussed in **Chapter 1**, these tissues are of varying embryonic origin: RPE cells are derived from the outer neuroectodermal sheath of the eyecup and the uveal melanocytes are of neural crest origin, the same embryonic origin as cutaneous melanocytes (Nordlund, 1989; Schraermeyer and Heimann, 1999; Bumsted and Barnstable, 2000; Boissy and Hornyak, 2006). Furthermore, studies of the eumelanin isolated from these different tissues in bovine eyes display a range of DHICA/DHI monomer ratios (Liu et al., 2005b). Thus, bovine eyes provide a unique system for examining how the absorption coefficients of

¹ Reproduced in part from: Peles, D. N.; Lin, E.; Wakamatsu, K.; Ito, S. and Simon, J. D. *J. Phys. Chem. Lett.*, **1**: 2391-2395, DOI: 10.1021/jz100720h

eumelanosomes vary for differing molecular composition and embryonic origin to ultimately provide insight into the macroscopic biological function of photoprotection.

Approaches to date for determining the optical properties of intact melanosomes involve indirect measurements and require assumptions about the thermodynamic properties of the intact organelle (Jacques and McAuliffe, 1991; Jacques et al., 1996; Strauss et al., 1997; Brinkmann et al., 2000; Glickman et al., 2001; Neumann and Brinkmann, 2005). Recall (**Chapter 2**), the absorption coefficients of melanosomes are reported as ϵc , in units of inverse length, as the lack of knowledge of the melanin structure prevents calculation of the concentration c . Jacques et al. utilized the indirect technique of explosive vaporization to calculate internal absorption coefficients of several types of melanosomes. In this method, the absorption coefficient is deduced from assumed thermodynamic properties of the melanosome and the threshold temperature measured after heating with a pulsed laser *in situ*. While most of this work has been focused in the mid-visible wavelength range, a general wavelength-dependent absorption coefficient is predicted based on the scaling of an *in vivo* spectrophotometer measurement of cutaneous melanin to the acquired data (Jacques and McAuliffe, 1991; Jacques et al., 1996). As a result, the determined wavelength-dependent absorption coefficient for cutaneous melanosomes is predicted to be $\epsilon c(\lambda_{nm}) = 1.70 \times 10^{12} \lambda^{-3.48} \text{cm}^{-1}$, while that for RPE melanosomes is predicted to be ~3.8-fold greater.

Despite the considerable effort directed to determining the absorption coefficient of melanosomes, the results do not directly reflect the absorption coefficient of a single intact melanosome. However, a novel application of the PEEM enables the direct measurement of the absorption coefficients of intact natural melanosomes (**Chapter 2**). Thus, in an effort to fully examine the photochemical properties of eumelanosomes, the PEEM technique is employed to measure the absorption spectra of single, intact natural eumelanosomes of varying DHICA:DHI ratios and embryonic origin over the spectral range from 244 nm to 310 nm to quantitatively probe the relationship between the absorption coefficients and pigment variations.

4.2 *Materials and Methods*

4.2.1 Sample Isolation

Details of the isolation of the studied melanosomes from bovine RPE cells and bovine iris and choroid tissues were previously published along with their chemical analyses (Liu et al., 2005b). Briefly, mature (> 2 years old) and newborn (< 1 week) bovine eyes were obtained from Animal Technology, Inc. (Tyler, TX). Dissection of the eyes occurred immediately upon receipt with a procedure described by Boulton et al. (Boulton et al., 1990). Through this procedure, each eye was hemisected at the equator and separated into the anterior and posterior eyecups. After removing the lens and vitreous body from the anterior segment, the iris and ciliary body were taken out and temporarily stored in Dulbecco's phosphate buffered saline without calcium and

magnesium (PBSA). Similarly, the vitreous body and neural retina were removed from the posterior segment and the RPE cells were then scraped off the Bruch's membrane and temporarily stored in PBSA. Following this removal, the choroid membrane was lifted and separated from the non-pigmented sclera and also temporarily stored in PBSA. Tissues from the two different age groups were pooled from 20-50 individual eyes. The samples were stored at -70° until further use.

As described (Liu et al., 2005b), the RPE melanosomes were extracted with the procedure described by Boulton et al., but with some modifications (Boulton et al., 1990). The RPE cell suspension was homogenized using a Teflon/glass homogenizer and was subsequently centrifuged at 60 g at 6°C for 6 min. The resulting supernatant was collected and the pellet was re-homogenized and centrifuged. The supernatants from both processes were subsequently combined and centrifuged at 3000 g at 6°C for 6 min. The melanosomes were re-suspended and subjected to the following purification procedures. First, melanosomes were washed in triplicate with PBSA using centrifugation at 2000 g at 6°C for 10 min. Second, the resulting melanosomes were subjected to a simplified discontinuous sucrose gradient centrifugation with 2.0 M and 1.4 M sucrose for 1 h at 4°C at 3200 g. Third, the resulting pellet was washed five times with pure water and lyophilized after being re-suspended in water.

The summarized enzymatic extraction used to isolate the iridal stroma melanosomes from the iris tissue described in **Chapter 3** is the same procedure that was utilized for melanosome isolation from bovine iris and choroid tissues (Liu et al., 2005b).

4.2.2 Photoemission Electron Microscopic Analysis

The UV absorption coefficients of the samples were quantified with the same procedures as described in **Chapter 2**.

4.3 Results

Figure 11 shows representative PEEM images of bovine ocular melanosomes on Ti substrates at $\lambda = 244$ nm at 50 μm fields of view. At this excitation wavelength, both the substrate and the melanosomes photoemit, but the organelles are resolved in the image as the efficiency of ionization (electrons per area) differs between the substrate and the melanosome. The shape and dimensions of the observed melanosomes are consistent with previously reported scanning electron microscopy analyses (Liu et al., 2005b). In each image, the substrate reveals shadows on the far side of the melanosomes that are oriented in the direction of the incident light, represented as the white arrow at the left bottom of panel (A). The shadows reflect a decreased photoionization intensity of the substrate as a result of the absorption of the incident light by the melanosomes.

An intensity contour plot of the shadow generated by the absorption of $\lambda = 244$

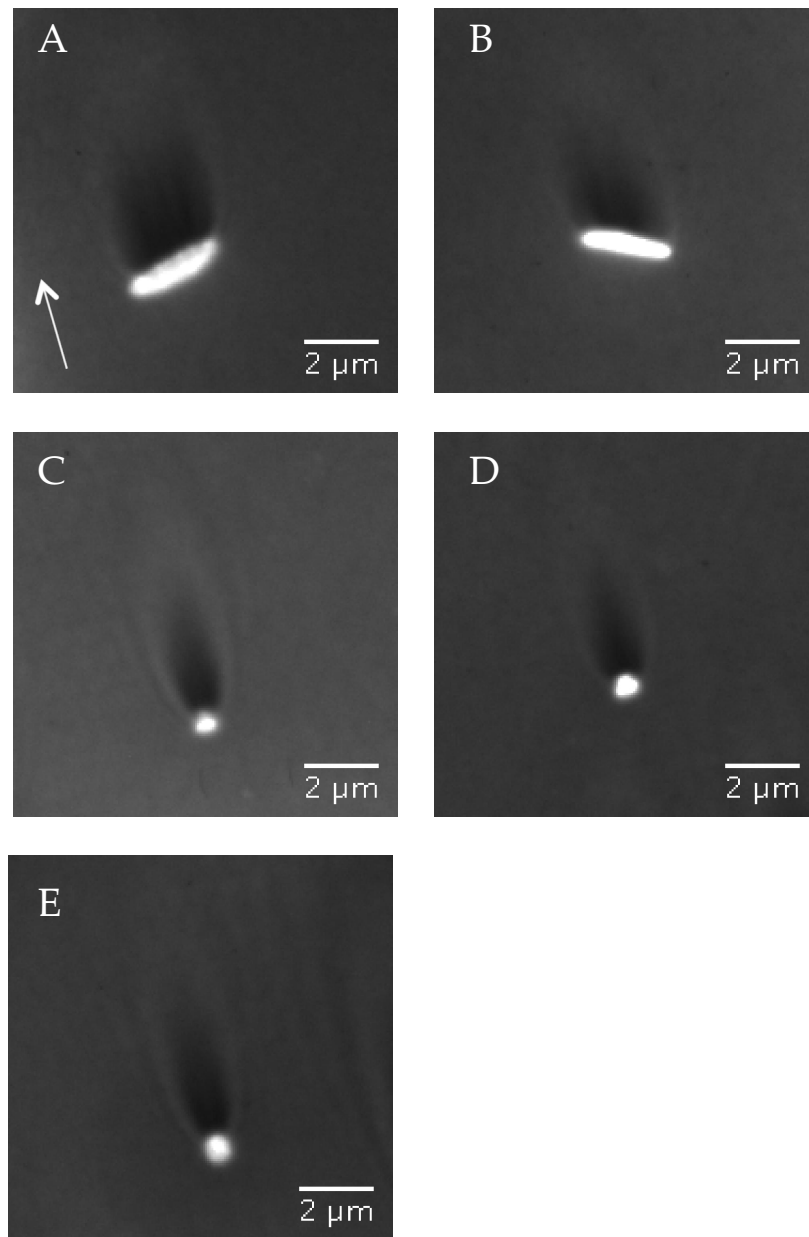


Figure 11: PEEM images of melanosomes isolated from A) adult and B) newborn bovine RPE, C) adult and D) newborn choroid melanosomes, and E) adult bovine iris. The images clearly reveal the shadows generated as a result of absorption of the incident light ($\lambda = 244$ nm). The shadows are oriented in the direction of incident light (indicated by the white arrow).

nm light by a newborn RPE melanosome is shown in **Figure 12-A**. Absorption of the melanosome is observed by the reduction of the photoemission intensity. Line plots reveal the spatial dependence of the photoemission intensity throughout the shadow. Plots of the intensity along the direction of incident light and perpendicular to the incident light are shown in **Figure 12-B** and **12-C**, respectively. The ellipsoidal shape of the melanosome dictates the shape of these plots. The intensity is symmetric about the center of the melanosome. As one moves away from the center toward the ends of the long axis, the pathlength through the melanosome decreases causing more UV light to reach the surface and subsequently produce higher photoemission from the substrate behind the melanosome. Accordingly, as one moves away from the equator toward the top of the melanosome, the pathlengths through the melanosome decrease, and higher photoemission is observed in the corresponding shadow regions.

PEEM images of a single adult bovine RPE eumelanosome are shown in **Figure 13** for each wavelength examined on SiC at 150 μm fields of view. In each image, a shadow is visualized behind the melanosome and was oriented in the direction of the incident light, represented as the white arrow at the left bottom of panel (A). Note, although the physical angle of the incident light remains constant, the apparent direction on the obtained image shifts with different fields of view as a result of changes in the currents through the electromagnetic optics. Eumelanosomes were not observed

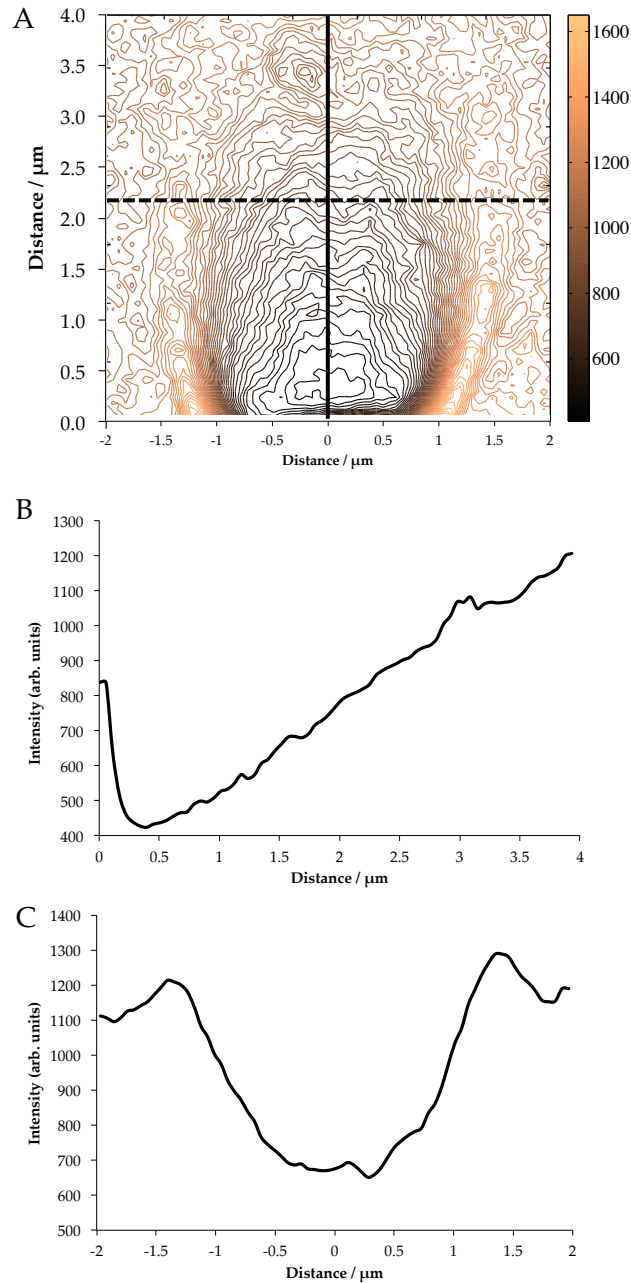


Figure 12: Spatial dependence of the shadows depicted through A) an intensity contour plot and B, C) intensity line scans. The intensity contour plot is of the shadow resulting from a newborn bovine RPE melanosome (not pictured). Line scans of the image are drawn through the shadow (solid and dashed lines in A) and are plotted as B) a function of perpendicular distance from the center of the melanosome, solid line drawn in A, and C) a function of distance parallel to the melanosome at a distance of $2.2 \mu\text{m}$ from its center, dashed line drawn in A.

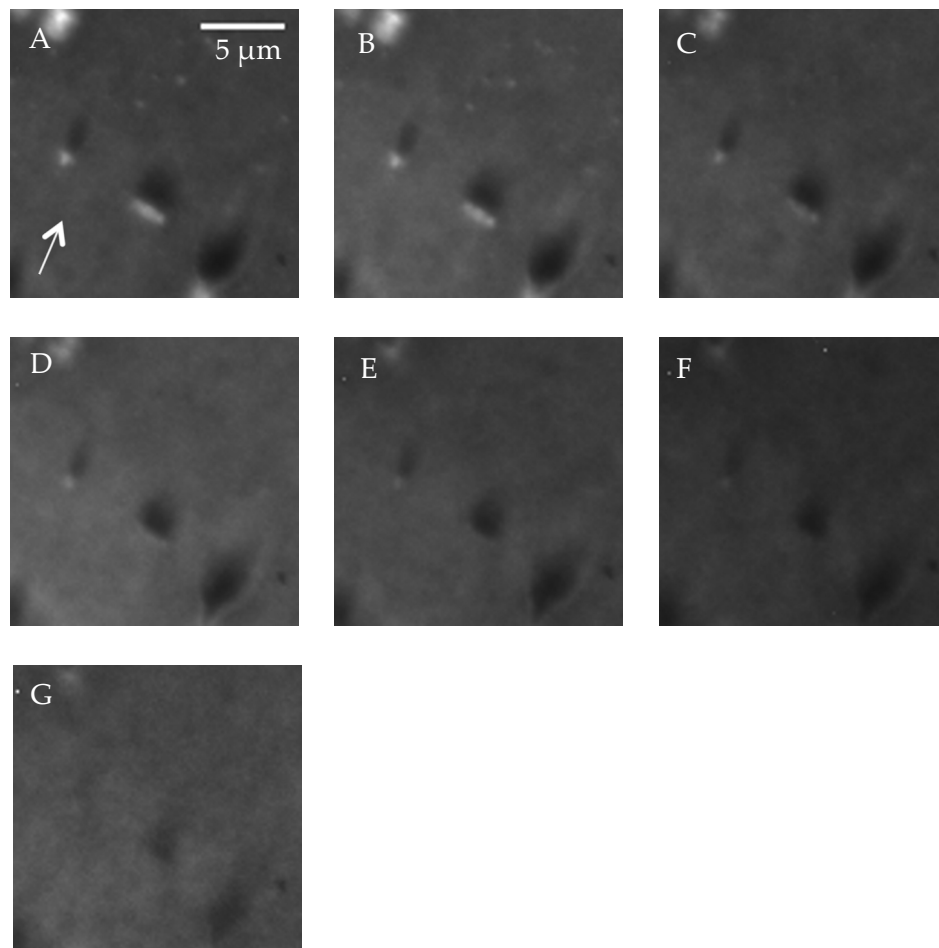


Figure 13: A sequence of PEEM images showing the wavelength-dependence of a single adult bovine RPE melanosome and its shadow on a SiC substrate. Images A - G were obtained upon illumination with laser wavelengths 244, 257, 270, 280, 290, 300, and 310 nm, respectively. The white arrow drawn in the bottom left of panel A) represents the direction of incident light on the sample.

in the PEEM images generated with wavelengths greater than $\sim 270 - 280$ nm as the characteristic photoionization threshold potential of eumelanin is $\sim 4.5 \pm 0.2$ eV (276 nm) (Garguilo et al., 2007). The substrate, however, is photoionized at all wavelengths examined and thus the generated shadows were visualized throughout the experiment. The images shown in **Figure 13** are representative of the wavelength-dependent PEEM images obtained for each of the studied eumelanosomes.

As described in the experimental methods section of **Chapter 2**, the absorption coefficients measured required using a tunable pulsed laser source and SiC substrates so that the shadow could be visualized over the wavelength region examined. Furthermore, as a result of the low-pulsed energy of the laser and a desire to ensure a large spatial sampling, fields of view of $150 \mu\text{m}$ were required. These experimental details were different than those where images were collected using a continuous wave Ar^+ ion laser on Ti at $50 \mu\text{m}$ fields of view. As shown in **Figure 14**, small changes are observed between calculated absorption coefficients when measured with different substrates, magnifications and laser sources; however, there is no systematic variation between the calculated values based on the methodology. Therefore, the different experimental conditions are not determined to have a significant influence on the calculated absorption coefficients and reflect the precision of the PEEM technique. The measured wavelength-dependent absorption coefficients are all obtained under the same experimental conditions and thus, variations between the observed ϵc

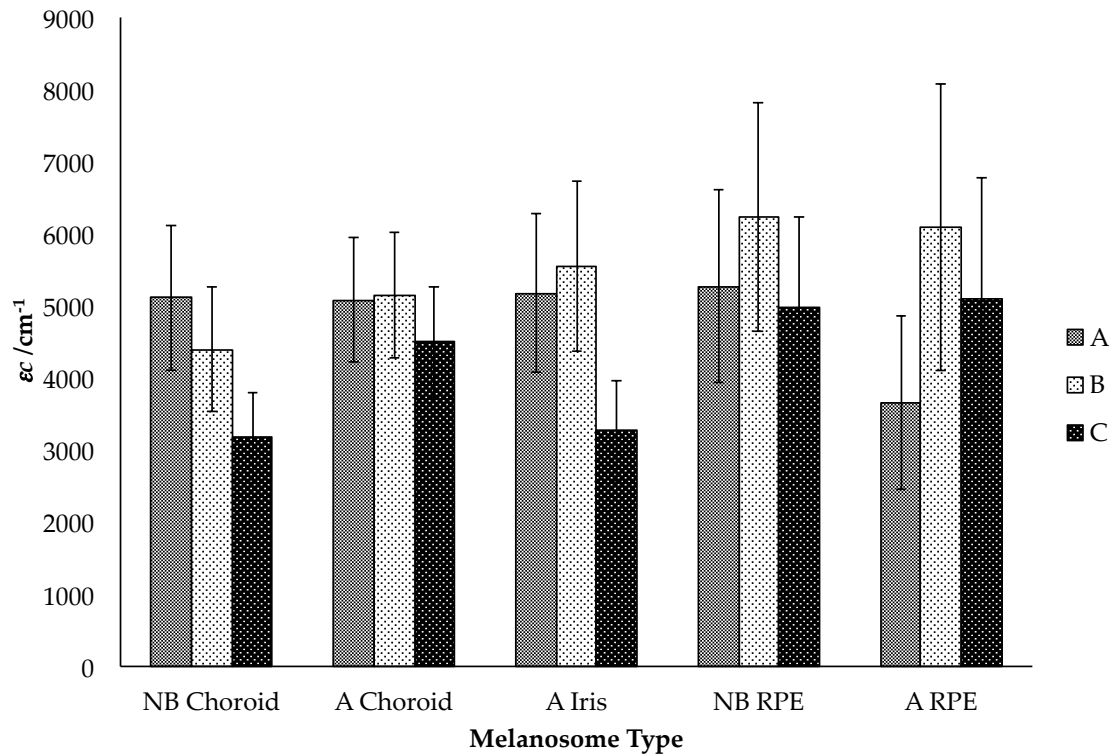


Figure 14: Average absorption coefficients measured at $\lambda = 244$ nm with different experimental conditions. Experimental conditions were A) 50 μm field of view, Ar^+ continuous wave laser and Ti substrate, B) 150 μm field of view, Ar^+ continuous wave laser and SiC substrate, and C) 150 μm field of view, pulsed nanosecond laser and SiC substrate.

measurements on eumelanosomes throughout the UV do not arise from substrate or laser sources used.

The measured absorption coefficients at $\lambda = 244$ and 300 nm are listed in **Table 2** along with the previously reported DHICA:DHI ratios for the bovine eye eumelanosomes (Liu et al., 2005b). The ratio of the yield of PTCA by KMnO_4 oxidation of the melanosomes to the total melanin (TM) determined by the absorbance at 500 nm for the samples dissolved in Soluene-350 serves as an excellent measure of the percentage content of DHICA-derived units (Ozeki et al., 1997b). The reported ϵc values are a result of an average of the full data set collected for each type of eumelanosome examined. Considerable variability was observed within the individual data sets throughout all wavelengths. As has been previously discussed in **Chapter 2**, the observed variability is a result of the fact that the pathlength calculations use the previously reported (Liu et al., 2005b) SEM average size dimensions of each eumelanosome as the limited resolution of the PEEM precluded the possibility of dimension measurements directly. Thus, the error of the averaged absorption coefficients arises through propagation of error of the eumelanosome size analyses. Errors calculated in this way are reported in **Table 2**. The error for each ϵc calculated at all wavelengths for the newborn and adult RPE, newborn and adult choroid and adult iris was determined to be 25.4, 32.8, 19.7, 17.0 and 21.3%, respectively.

Table 2: Summary of the chemical degradation analyses and absorption coefficients of eumelanic melanosomes. The chemical degradation analyses have been previously published (Liu et al., 2005b); products are expressed in units of per mg melanosomes. PTCA was determined from oxidation by KMnO_4 .

| Melanosomes | Age | PTCA $\mu\text{g}/\text{mg}$ | TM A_{500}/mg | PTCA/TM $\mu\text{g}/A_{500}$ | DHICA:DHI | ϵc (244 nm) cm^{-1} | ϵc (300 nm) cm^{-1} |
|-------------|---------|---------------------------------|---------------------------|----------------------------------|-----------|---|---|
| RPE | Newborn | 7.7 | 5.91 | 1.30 | 1.30:1 | 4970 (1260) | 2685 (730) |
| | Adult | 4.2 | 5.26 | 0.80 | 0.80:1 | 5100 (1675) | 3495 (1145) |
| Choroid | Newborn | 14.7 | 6.34 | 2.32 | 2.32:1 | 3175 (625) | 1720 (340) |
| | Adult | 5.6 | 4.60 | 1.21 | 1.21:1 | 4495 (765) | 1935 (330) |
| Iris | Adult | 5.2 | 5.19 | 1.00 | 1.00:1 | 3270 (695) | 1780 (380) |

The averaged ϵc values for all adult eumelanosomes are plotted as a function of wavelength in **Figure 15**. Newborn melanosomes show similar trends. Generally, ϵc values decreased with increasing wavelength, as expected from previous measurements reported on synthetic and natural melanosomes (Sarna and Sealy, 1984b; Jacques and McAuliffe, 1991; Jacques et al., 1996; Sardar et al., 2001; Meredith and Sarna, 2006). Furthermore, as evidenced in **Figure 15**, the absorption coefficients of bovine RPE eumelanosomes were on average about 1.5-fold greater than those for eumelanosomes isolated from bovine choroid or iris tissues, regardless of age.

4.4 Discussion

When evaluating the attenuation of light, absorption and scattering must be considered due to the complex nature of the eumelanosomes. While it is difficult to evaluate the contribution of the scattering phenomena to our absorption measurement, we have attempted to disaggregate the two effects within the shadow region. As previously discussed (**Chapter 2**), the portion of the shadow region that is void of significant scattering contributions was determined following the methodology outlined by Chelaru et al. (Chelaru et al., 2006). Briefly, diffraction will influence the intensity in the shadow region beginning at a distance from the eumelanosome corresponding to the first maximum in the diffraction pattern observed on the substrate. This distance can be calculated from the Fraunhofer diffraction pattern of an elliptical aperture of the same dimensions as the eumelanosomes as the two diffraction patterns are the same except for

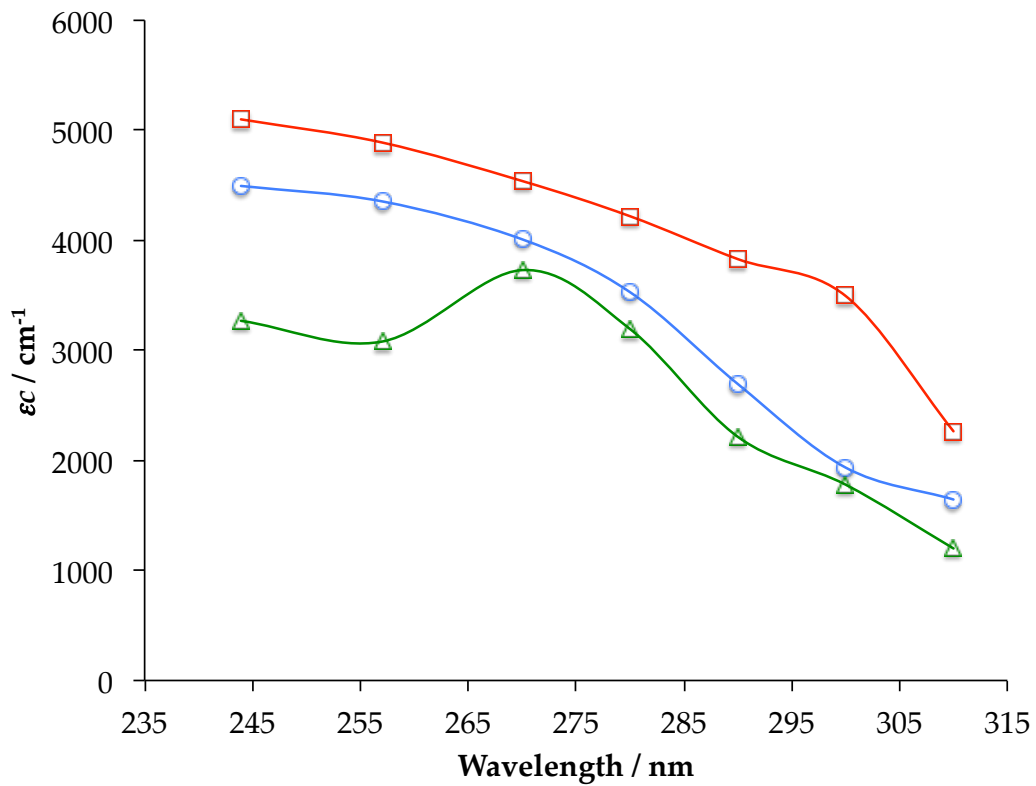


Figure 15: Summary of the average measured absorption coefficients of the bovine eumelanosomes versus wavelength. Adult bovine RPE (squares), choroid (circles) and iris (triangles) are plotted.

an inversion of the intensity distributions. This calculation, outlined in the experimental methods section (**Chapter 2, Equation 5**), was used for each eumelanosome at all wavelengths. As long as the region of the shadow analyzed is determined in this manner, it is the case that the calculated ϵc values for the eumelanosomes predominately reflect absorption of melanin.

It is important to acknowledge that although eumelanosomes are mainly comprised of eumelanin, they also contain proteins, lipids and various ions. While most lipids and amino acids exhibit negligible absorption between $\lambda = 244 - 310$ nm, the aromatic amino acids do absorb in this spectral range. The absorption maxima (extinction coefficient) of the aromatic amino acids Phe, Tyr and Trp are 257.4 nm (165 $M^{-1}cm^{-1}$), 274.6 nm (1,430 $M^{-1}cm^{-1}$), and 279.8 nm (6,000 $M^{-1}cm^{-1}$), respectively (Wetlaufer, 1962), with the extinction coefficients of the latter two on the order of the observed ϵc values. The contribution of the protein to the absorption measurements can be deduced from reported amino acid profiles of eumelanosomes. The protein content of the studied eumelanosomes increases from RPE to iris to choroid and ranges from 9 – 15% (Liu et al., 2005b). The distributions of the amino acids, however, are similar and the aromatic amino acid content makes up less than 10% of the protein composition for each type of eumelanosome (Liu et al., 2005b). Therefore, the contribution of the aromatic amino acids is expected to be at most 1.5% of the total absorption throughout the spectral range studied. This total contribution to the measured absorption is negligible.

Therefore the measured absorption predominately reflects that of the eumelanin pigment and as a result **Figure 15** represents quantitative absorption spectra of the pigment contained within bovine RPE, choroid and iris eumelanosomes.

Eumelanin is built from varying amounts of the monomeric dihydroxyindole building blocks, DHI and DHICA, (**Table 2**) (Liu et al., 2005b). Initial single-wavelength PEEM experiments performed on intact eumelanosomes (measured with the experimental conditions reported as “A” in **Figure 14**) at $\lambda = 244$ nm suggest that as the DHICA content increases, the ϵc of the melanosome increases. This observation was compared to the UV absorption spectra and extinction coefficients for the DHI and DHICA monomers (Benigni and Minnis, 1965; Ito and Nicol, 1974; Murphy and Schlutz, 1985; Tran et al., 2006; d'Ischia et al., 2008; Gauden et al., 2009). The extinction coefficients of DHI and DHICA are somewhat sensitive to pH; an average of the ϵ values from the published literature gives 2610 and 5530 $\text{M}^{-1} \text{cm}^{-1}$ at $\lambda = 244$ nm for DHI and DHICA, respectively. On the basis of the extinction coefficients of the contributing monomers, an increased absorption is expected with increased DHICA/DHI ratios.

If the absorption of the melanosome was modeled as arising from the sum of the absorption of contributing DHI and DHICA monomers, it is written as

$$A = \ell(\epsilon c)_{\text{eumelanin}} = \ell(\epsilon_{\text{DHI}} [\text{DHI}] + \epsilon_{\text{DHICA}} [\text{DHICA}]). \quad (12)$$

In terms of mole fraction, X , **Equation 12** becomes

$$\epsilon_{\text{eumelanin}} = \epsilon_{\text{DHI}} X_{\text{DHI}} + \epsilon_{\text{DHICA}} X_{\text{DHICA}}. \quad (13)$$

Because the total mole fraction is unity, $1 - X_{DHICA} = X_{DHI}$, and **Equation 12** can be written as

$$\epsilon_{eumelanin} = X_{DHICA}(\epsilon_{DHICA} - \epsilon_{DHI}) + \epsilon_{DHI} \quad (14)$$

Under this assumption, a plot of the melanosome absorption coefficients as a function of the percentage of DHICA content would have limiting values at the end points $X_{DHICA} = 0$ and 1 , given by ϵ_{DHI} and ϵ_{DHICA} , respectively. **Figure 16** shows a plot of ϵc as a function of the mole fraction of DHICA contained in the melanosomes. The line shown in the plot is drawn between the average ϵ values of the two monomers (2610 and 5530 $M^{-1} cm^{-1}$). This line represents the predicted absorption coefficients, assuming that this value is given by the sum of the constituent concentration of contributing DHI and DHICA monomers, **Equation 12**. The observed ϵc values are consistent with those with **Equation 14**, suggesting that the absorption of natural melanins can be quantified in terms of relative content of the two constituent monomers, weighted by their relative mole fractions. However, the region probed (% DHICA 0.4 - 0.7) and the spread of the data certainly indicates that this conclusion requires further testing to be substantiated. Such a trend was not observed with the $\lambda = 244$ nm ϵc values measured with SiC substrates and a tunable pulsed nanosecond laser (experimental conditions "C" of **Figure 14**), **Table 2**; the lack of correlation may be a reflection of the precision of the PEEM technique, **Figure 14**. To further examine whether ϵc for the melanosome

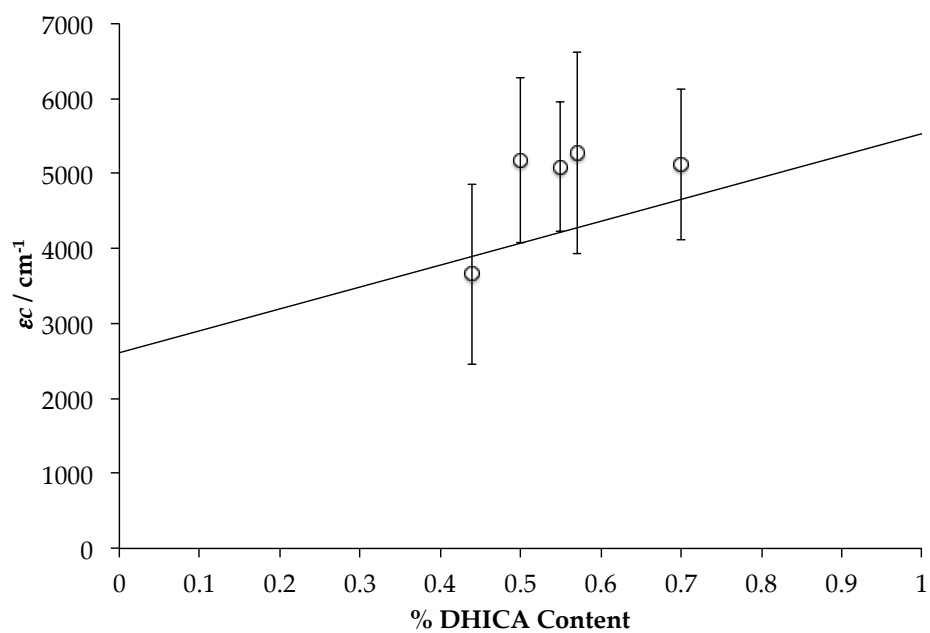


Figure 16: Plot of the observed absorption coefficient versus DHICA content at $\lambda = 244 \text{ nm}$. The line is representative of the predicted absorption as arising from the sum of the absorption of contributing DHI and DHICA monomers.

maintains an additive relationship with the constituent monomers across the absorption spectrum, the longer UV wavelength region is of importance.

The shapes of the absorption spectra of DHI and DHICA are similar in the spectral region from 240-270 nm, but differ significantly in shape in the UV-A with the absorption maxima (extinction coefficient) being $\lambda = 296 \text{ nm}$ ($3,310 \text{ M}^{-1} \text{ cm}^{-1}$) and $\lambda = 320 \text{ nm}$ ($\sim 14,000\text{-}16,000 \text{ M}^{-1} \text{ cm}^{-1}$), respectively (Murphy and Schlutz, 1985; Tran et al., 2006). Note, as mentioned, the exact literature values for the extinction coefficients of DHI and DHICA vary depending on the solvent or pH and the aforementioned spectra, taken in deaerated water and NaOH solution, respectively, were used throughout the presented analyses presented. If we were to model the absorption of the adult RPE eumelanosome as arising from the sum of the absorptions of its contributing DHI and DHICA monomers, weighted by their relative mole fractions, an absorption spectra similar to **Figure 17A** would be obtained, where the DHICA extinction coefficient increases the absorption at wavelengths nearing the UV-A. The measured absorption spectra presented in **Figure 15**, however, are in stark contrast to the predicted spectra. A decrease in the absorption is observed in the longer wavelength regions. Furthermore, as shown in **Figure 17B**, a plot of the eumelanosome absorption coefficients as a function of the percentage of DHICA content, at $\lambda = 300 \text{ nm}$, revealed a decrease in ϵc with an increase of DHICA content. The observed trend did not extrapolate to the limiting values of the DHI and DHICA extinction coefficients as would have been expected if the

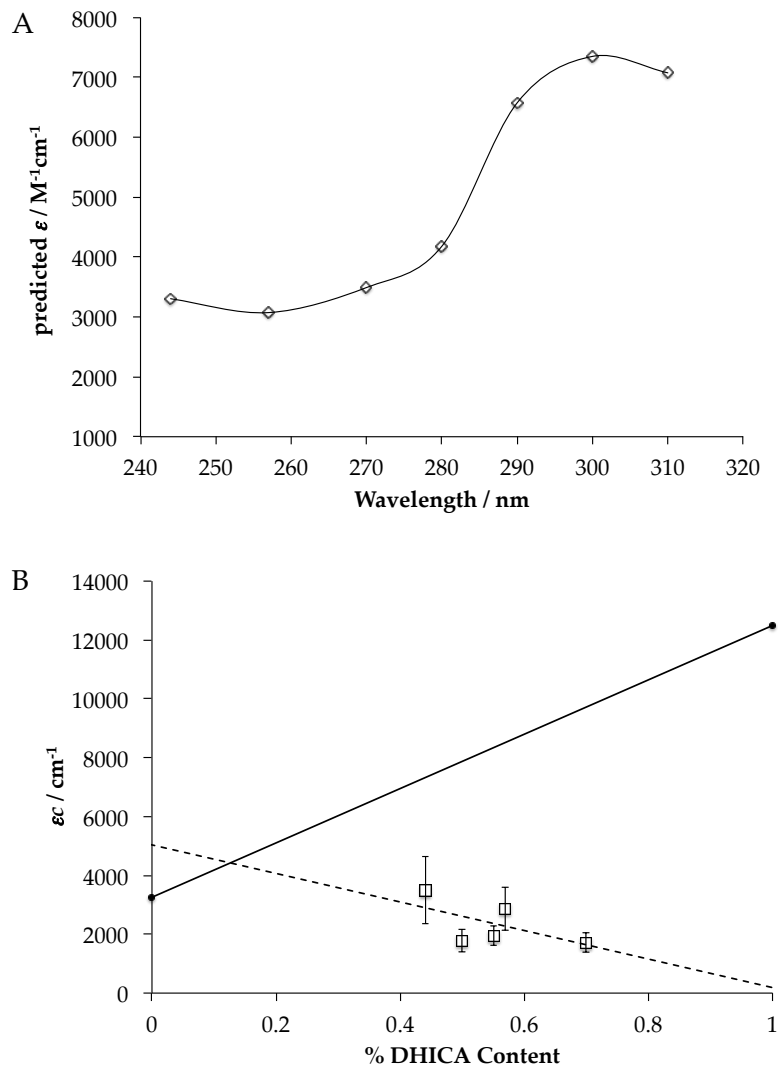


Figure 17: Predicted absorption spectra as arising from the sum of the absorption of contributing DHI and DHICA. The absorption spectra plotted in A) is the prediction based on the determined monomer composition for adult bovine RPE melanosomes (0.44 % DHICA). A plot of the observed absorption coefficients versus the % DHICA content at $\lambda = 300$ nm (open squares) is shown in B). The data points 0 and 1 % DHICA (black circles) are representative of the DHI and DHICA extinction coefficients at this wavelength and the solid line drawn between the points is the predicted absorption as arising from the sum of the absorption of the contributing monomers. The observed trend (dashed line) is in stark contrast to this prediction.

absorption of the eumelanosomes arose from the sum of the constituent concentration of contributing DHI and DHICA monomers. This trend was observed with all calculated absorption coefficients in the 280-310 nm region of interest. It was therefore unequivocally concluded that the predicted additive relationship with the constituent monomers is not maintained across the absorption spectrum.

Despite extensive experimental studies conducted on synthetic and natural eumelanin, including its soluble fraction, the structures of the natural oligomers formed from DHI and DHICA have evaded characterization. As a result, a thorough understanding of the unique optical properties of eumelanins has remained an immensely complex topic. The absorption data on intact, natural eumelanosomes offers a direct view into the oligomeric structure of the eumelanin pigment. As has been discussed, the natural oligomeric structure is not reflective of the electronic structure of the monomers throughout the ultraviolet. This is most notable in the UV-A region where the low energy band of DHICA appears to have a negligible effect on the absorption of the pigment. These results indicate that polymerization of DHICA into the melanin pigment disrupts the electronic structure of these monomeric building blocks; that polymerization modifies the monomers in the resulting oligomer. Recently, papers have been published that provide insight into UV-visible absorption properties of the evolution of the DHI and DHICA monomers into larger oligomeric structures (dimer to tetramer) (Tran et al., 2006; Riesz et al., 2007; d'Ischia et al., 2008; Pezzella et al., 2009a;

Pezzella et al., 2009b). The collective work observes absorption spectral shapes of the DHI and DHICA monomers that gradually shift towards the broadband eumelanin spectrum upon oxidative polymerization. In the studies of the DHICA polymerization (Tran et al., 2006; Riesz et al., 2007), the absorption maximum at $\lambda = 320$ nm was found to decrease as a function of time and a 20% hyperchromism was observed for the DHICA polymer compared to that of the monomer. These model studies have shown that the chemical linkages between the monomers affect the spectroscopic properties of the resulting oligomers. While the relevance of these model studies to the actual eumelanin oligomer remains to be assessed, similarities between the optical properties of the model oligomers are in accord with those of the natural eumelanosomes. The electronic structure of the eumelanin oligomer does not resemble the electronic structure of the monomeric building blocks, DHI and DHICA, suggesting that the monomers are in fact modified upon polymerization to the eumelanin pigment.

In an effort to further examine the natural oligomeric structure of the eumelanin pigment, a comparison of the absorption coefficients of the eumelanosomes as related to their embryonic origins is of interest. As plotted in **Figure 15**, the absorption coefficients calculated for the bovine RPE eumelanosomes were on average 1.5-fold greater than those measured for the uveal eumelanosomes. These results suggest that either the eumelanin pigment is present in greater density or that there is an underlying difference in the eumelanin molecular structure. The greater absorption coefficient between the

eumelanosomes derived from the primitive forebrain compared to those derived from the neural crest is consistent with previous estimates, but is less than the predicted 3.8-fold difference (Jacques et al., 1996). **Figure 18** compares the measured absorption coefficients of the RPE and uveal eumelanosomes with the previously reported and predicted cutaneous (Jacques and McAuliffe, 1991; Jacques et al., 1996) and RPE (Williams et al., 1985; Jacques et al., 1996; Strauss et al., 1997; Brinkmann et al., 2000; Glickman et al., 2001; Sardar et al., 2001; Neumann and Brinkmann, 2005) melanosome absorption coefficients. At the mid-visible wavelengths, the absorption coefficients of the RPE melanosomes were predominately larger than those for the cutaneous melanosomes in accord with the predictions. As seen, however, there is a large variance in the reported absorption coefficients; the values for RPE and cutaneous melanin ranged from 5 cm⁻¹ to 11,000 cm⁻¹ and 78 cm⁻¹ to 997 cm⁻¹ at the mid-visible wavelengths, respectively. The large variance may reflect differences in sample preparation, methodology and perhaps, to a lesser degree, individual variation (Sarna, 1992; Sardar et al., 2001; Riesz et al., 2006). In contrast to the previous studies, however, the absorption coefficients obtained herein are measured directly from single, intact natural eumelanosomes. The results suggest that while the RPE eumelanosome absorption coefficients are larger than those of the uveal eumelanosomes, the differences between the two are not comparable to the previously predicted differences and that the

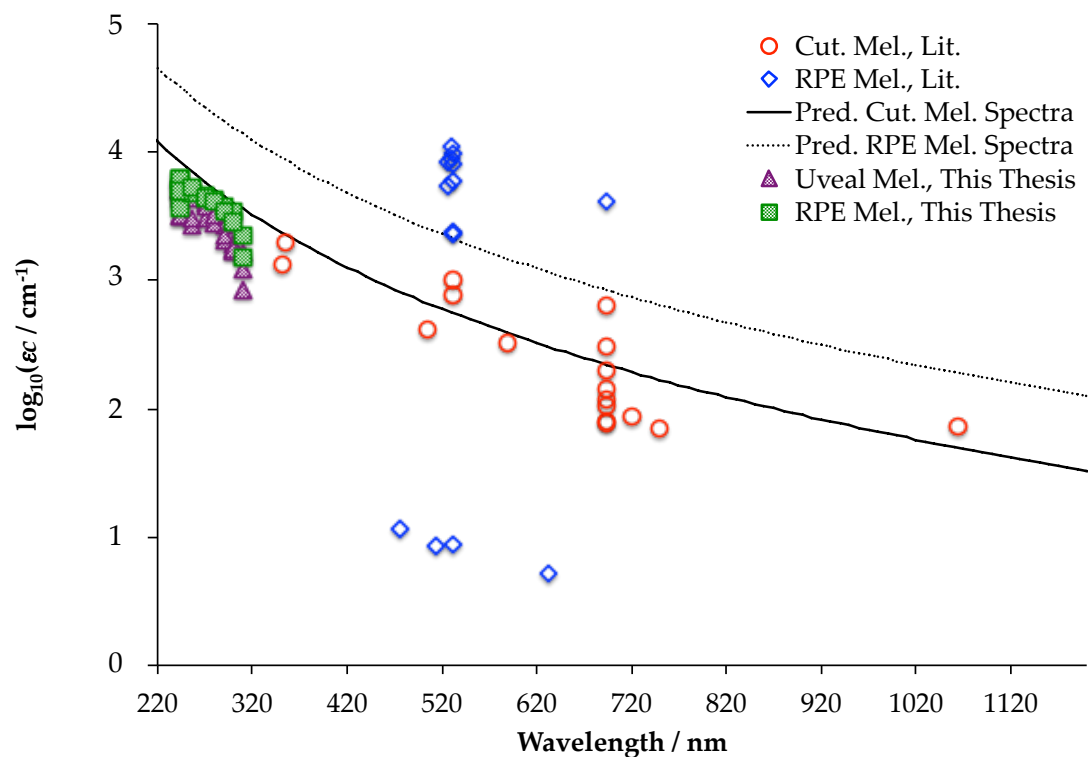


Figure 18: Comparison of the PEEM measured absorption coefficients with those previously reported in literature. Comparisons are made between the absorption coefficients calculated herein on uveal (iris and choroid) and RPE melanosomes (shaded triangle and rectangle data points, respectively) with previously reported cutaneous (Jacques et al., 1996) and RPE (Jacques et al., 1996; Strauss et al., 1997; Brinkmann et al., 2000; Glickman et al., 2001; Sardar et al., 2001; Neumann and Brinkmann, 2005) melanosome absorption coefficients (open circle and diamond data points, respectively) and previously predicted (Jacques et al., 1996) cutaneous and RPE spectra (solid and dashed lines, respectively).

calculated RPE eumelanosome absorption coefficients are comparable to the previously predicted cutaneous melanosome absorption coefficients.

4.5 Conclusions

The absorption coefficients of natural intact eumelanosomes from bovine eye tissues have been directly quantified. The lower-energy UV-A region provides support that the electronic structure of the naturally occurring eumelanic oligomers do not reflect the electronic structure of the monomers. Furthermore, an analysis of the absorption coefficients of the RPE eumelanosomes compared to the uveal eumelanosomes found a 1.5-fold increase, less than the difference predicted by previous reports. The observed difference suggests that either the eumelanin pigment present in RPE is of in greater density or that there is an underlying difference in the eumelanic molecular structure between the eumelanin derived from different embryonic origins.

5. The Ultraviolet Absorption Coefficients of Human Iridal Stroma Melanosomes¹

5.1 Introduction

Epidemiological data for uveal melanoma, the most common intraocular malignant tumor in human adults, suggests a link between incidence and the relative concentrations of pheomelanin (Wakamatsu et al., 2007; Hu et al., 2008). This observation is consistent with studies that indicate that pheomelanin is more pro-oxidant than eumelanin (Chedekel et al., 1978; Harsanyi et al., 1980; Persad et al., 1983; Takeuchi et al., 2004; Ye et al., 2006; Ye et al., 2008). However, because pheomelanin is naturally encased by the photoprotective eumelanin (**Chapter 3**), exposure of the pigment is necessary to induce oxidative stress. One mechanism by which this could occur is through oxidative damage to the melanosome over time, exposing or releasing the phototoxic pigment. Because the outer eumelanin layer becomes thinner with increasing pheomelanin content, such a model of “damage-induced” exposure of pheomelanin is consistent with the epidemiological observations. But other properties of the melanosomes may also change significantly with composition to correlate with the epidemiological data. Thus, it is of interest to also consider whether other photophysical

¹ Reproduced in part from: Peles, D. N. and Simon, J. D. *J. Phys. Chem. B*, **114**: 9677-9683, DOI: 10.1021/jp102603b and Simon, J. D. and Peles, D. N. (2010) *Acc. Chem. Res.*, **43**: 1452-1460, DOI: 10.1021/ar100079y

properties, such as photoprotection, vary significantly with pigment composition in a way that may further correlate with the epidemiological data.

The relative extinction coefficient, ϵ , of eumelanin and pheomelanin is necessary to understand and compare the quantum efficiency of photon absorption and subsequent photochemical reactions, such as oxygen activation, that are of biological importance. Unfortunately, the complex character of these natural melanins (highly insoluble, heterogeneous and difficult to isolate in pure form) has precluded detailed characterization of their macromolecular structure (Prota, 1992). As a result of these difficulties, studies on absorption properties of the pigments are usually conducted on synthetic model systems dissolved or suspended in buffer solutions that mimic physiological conditions (Sarna and Swartz, 2006). The absorptions exhibited by the synthetic melanins are normalized for concentration and extinction coefficients are expressed in terms of $\text{cm}^{-1}(\text{mg}/\text{mL})^{-1}$, units commonly used because of the lack of molecular structure information even in soluble synthetics. Thus, the absorption properties of natural eumelanin and pheomelanin contained in intact melanosomes have remained elusive.

The PEEM approach, developed in **Chapter 2**, has enabled a direct measurement of the absorption properties of melanins within intact melanosomes, **Chapter 4**. In this chapter, the first measurements of the absorption coefficients, ϵ_c , of intact iridal stroma melanosomes isolated from dark brown and blue-green human irides are described for

the spectral range $\lambda = 244 - 310$ nm. The iridal stroma melanosomes are an excellent system for quantifying the natural absorption coefficients of the two classes of pigments because different colored irides produce organelles of varying eumelanin:pheomelanin ratios (Wakamatsu et al., 2007) with similar size and morphology, **Chapter 3**. Chemical degradation analyses reveal eumelanin:pheomelanin ratios of 14.8 and 1.3 for melanosomes present in dark brown and blue-green human irides, respectively, and therefore, this single natural system enables a systematic approach for determining how the absorption coefficient changes with varying pigment composition. The experimental spectra measured within are compared with both the extinction coefficient spectra obtained on soluble synthetic model systems and the monomeric precursors to each pigment. Modeling the pigment in terms of the currently known monomeric chromophores enables the measured ϵ to be surveyed in units of $M^{-1}cm^{-1}$ instead of cm^{-1} , providing opportunities to compare extinction coefficients per monomer.

5.2 *Materials and Methods*

5.2.1 Sample Isolation

The isolated iridal stroma melanosomes from different colored iris tissues used to determine the size distributions and surface photoionization potentials in **Chapter 3**, are the same samples used in this chapter. Details of their enzymatic extraction were described in **Chapter 3**.

5.2.2 Photoemission Electron Microscopic Analysis

The UV absorption coefficients of the samples were quantified with the same procedures as described in **Chapter 2**.

5.3 Results and Discussion

Human iridal stroma melanosomes isolated from different colored irises were imaged with PEEM to directly quantify absorption coefficients of the eumelanin and pheomelanin pigments in the spectral range $\lambda = 244 - 310$ nm. **Figure 19** shows acquired PEEM images for dark brown iridal stroma melanosomes on SiC at $\lambda = 244$ nm (A) and 310 nm (B). The energy associated with the laser light at $\lambda = 244$ nm surpassed the photoionization threshold of the substrate and the melanosome and both were visualized in **Figure 19A**. In comparison, only the substrate was visualized in the PEEM image acquired with $\lambda = 310$ nm, **Figure 19B**. The photoionization threshold of the dark brown (and blue-green) iridal stroma melanosomes surpasses the laser energy at $\lambda \sim 260$ nm (**Chapter 3**) and, as a result, does not photoemit at the longer wavelengths examined herein. The shadows generated behind the melanosomes, however, continued to be visualized as the substrate is characterized with a low work function and subsequently provided the necessary contrast for visualization. The images presented in **Figure 19** were representative of the PEEM images acquired for all melanosomes studied, regardless of iris color.

Absorptive properties were determined from changes in the intensity of the

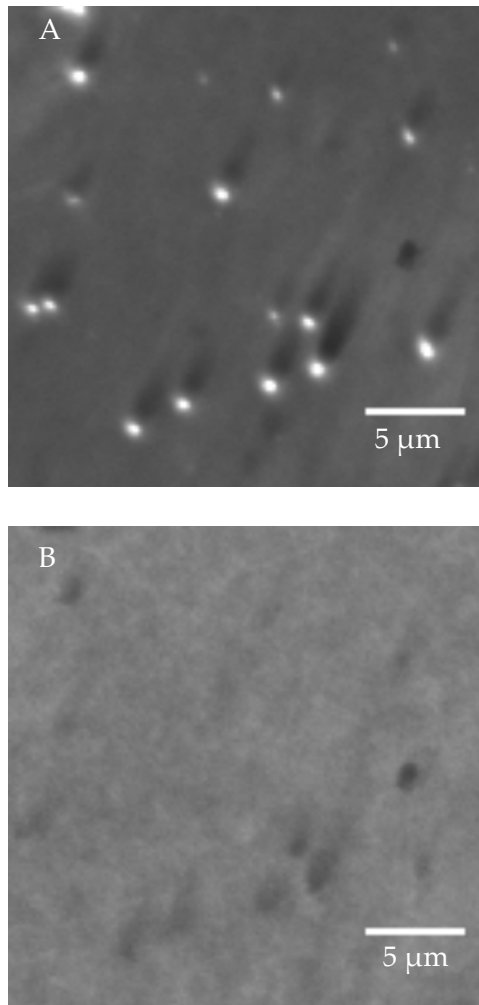


Figure 19: PEEM Images of dark brown iridal stroma melanosomes at A) $\lambda = 244$ nm and B) $\lambda = 310$ nm. The white arrow at the bottom left of panel A) identifies the direction of incoming light. The black spot observed in the right center of each image is the result of damage of the PEEM multichannel plate and is not part of the sample surface.

portion of the shadow identified as the first maximum of the diffraction pattern produced immediately behind the melanosome as this region is void of significant scattering contributions, **Chapter 2** (Chelaru et al., 2006). The total absorption of light, however, is a result of the absorption from all constituents within the melanosome: proteins, lipids and melanin. However, in the case of human iridal stroma melanosomes, the quantities of each of these constituents are not known. Although several studies have examined the protein content of melanosomes isolated from different human and animal tissue sources, the majority of these were based on melanosomes that had been isolated with acid/base extraction techniques (Borovansky and Hach, 1973; Borovansky and Duchon, 1974; Sarna et al., 1980). This particular extraction method was widely used to extract melanosomes from tissue, but this approach is now known to both alter the physical and biological properties of the melanosome and result in isolation of a larger protein content than that associated with intact melanosomes (Liu et al., 2003).

As a specific example, melanin comprises ~86% of the material present in enzymatically extracted melanosomes from black human hair, whereas the acid-base extraction of melanosomes from the same hair sample alters the melanosome structure, and the isolated materials contain 40-52% protein, depending on the method used (Liu et al., 2003). Thus, although previous isolation techniques produced samples with large

protein content, enzymatic isolation of intact melanosomes reveals that the dominant constituent in the organelle is the melanin pigment.

In addition, most lipids and amino acids exhibit negligible absorption in the UV spectral range studied. Noted exceptions are the aromatic amino acids Phe, Tyr and Trp, which are characterized with extinction coefficients of 165, 1430 and 6000 $\text{M}^{-1}\text{cm}^{-1}$ at $\lambda = 257.4, 274.6$ and 279.8 nm, respectively (Wetlaufer, 1962). As discussed in **Chapter 4**, the aromatic amino acid composition makes up less than 10% of the proteins in bovine iride melanosomes, with the relative melanin to protein content approximately 7:1 (wt/wt) (Liu et al., 2005b). These aromatic amino acids are thus expected to contribute of at most 1.5% to the total measured absorption. This is a negligible contribution and as a result it is concluded that the measured absorption does not reflect lipid and protein content, but instead is reflective of the eumelanin and pheomelanin pigments contained within the melanosomes.

Wavelength-dependent absorption coefficients for dark brown and blue-green human iridal stroma melanosomes are shown in **Figure 20**. The plotted absorption coefficients were determined from an average of the full data set collected on each type of melanosome. Variability was observed between the individual melanosomes within the measured data sets as a result of using average SEM dimensions (**Chapter 3**) in the pathlength calculation. The error of the reported absorption coefficients was calculated through the propagation of error of the melanosome size analyses and was determined

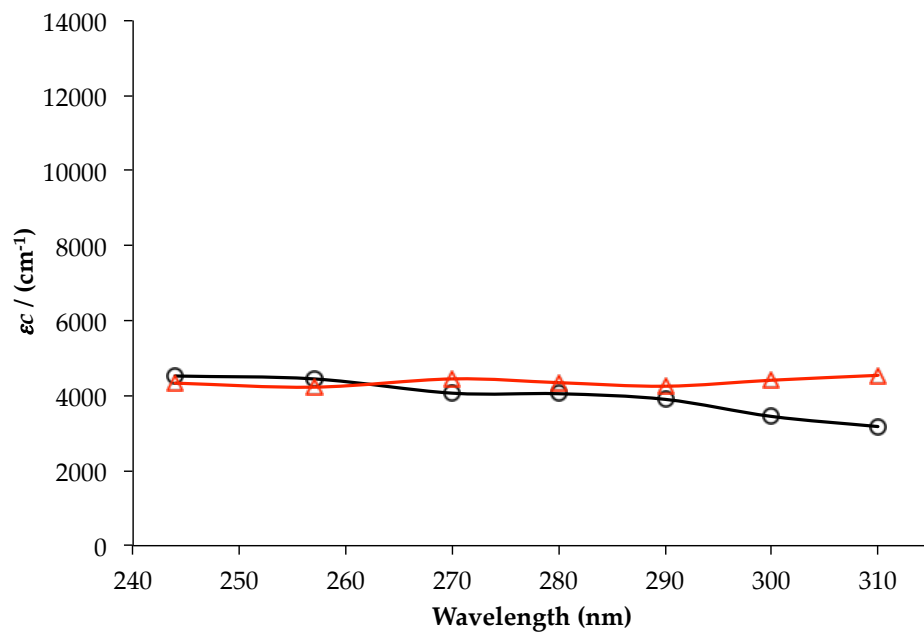


Figure 20: Average absorption coefficients versus wavelength for melanosomes isolated from dark brown and blue-green iridal stroma tissues. Absorption coefficients calculated from dark brown and blue-green iridal melanosomes are represented as open circles and triangles, respectively.

to be 33.6 and 34.7% for dark brown and blue-green human iridal stroma melanosomes, respectively.

In comparing the spectra from the dark brown and blue-green iridal stroma melanosomes, the same spectrum was observed within reasonable error. As the dark brown and blue-green iridal stroma melanosomes have relative pheomelanin compositions of 6 and 43%, respectively, the results suggest that the absorption of the melanosomes containing a mixture of eumelanin and pheomelanin does not significantly differ from those containing pure eumelanin. Because the absorption coefficients of the melanosomes are found to be independent of the melanic composition it is of interest to subsequently examine these values in terms of the pigment monomers to obtain extinction coefficients for further comparisons with synthetic samples.

The molecular chromophores of eumelanin are DHI and DHICA whereas the chromophore of pheomelanin is built from molecules such as dihydro-1,4-benzothiazine-3-carboxylic acid (DHBTCa) and 6-(2-amino-2-carboxyethyl)-4-hydroxybenzothiazole (BZ) (Wakamatsu et al., 2009). These precursors have different molecular volumes. AM1 calculations of the molecular volumes of DHI, DHICA, BZ, and DHBTCa give 0.129, 0.172, 0.195, and 0.268 nm³, respectively (<http://www.molinspiration.com/services/volume.html>). The chemical degradation analyses used to determine the eumelanin and pheomelanin content is a measure of the number of these monomer building blocks present in the intact pigment, and for a

constant total volume, an increase in the number of DHBTCAs units must result in a loss of a larger number of DHI/ DHICA units because DHBTCAs occupy a larger volume than a DHI/DHICA molecule. Therefore, if these species comprise the pigment and act as the “chromophore”, the total number of monomeric chromophores (eumelanin and pheomelanin combined) decreases, with increasing pheomelanin content. Taking the volume of the melanosome (calculated from the average dimensions determined from the SEM size analysis presented in **Chapter 3**), the eumelanin:pheomelanin ratio determined from chemical analyses, and the above volumes for the molecular building blocks (using an average of the DHI/DHICA volumes to represent the eumelanin precursors), a 32% decrease in the number of chromophores is found in blue-green iridal stroma melanosomes as compared with dark brown iridal melanosomes. Taking this decrease into account with the absorption data for intact melanosomes presented in **Figure 20**, we predict that the extinction coefficient (per monomer) for pheomelanin is on average 1.9 fold greater than that of eumelanin throughout the spectral range studied.

Sarna and co-workers reported extinction coefficients for synthetic eumelanin and pheomelanin plotted as a function of $\text{cm}^{-1}(\text{mg/mL})^{-1}$ versus λ (Sarna and Swartz, 2006) and the spectra of the two synthetic pigments were quite similar (**Figure 21A**). Steven Jacques subsequently converted melanin concentration expressed as (mg/mL) into (moles/liter) by multiplying the respective spectra by the molecular weight of the

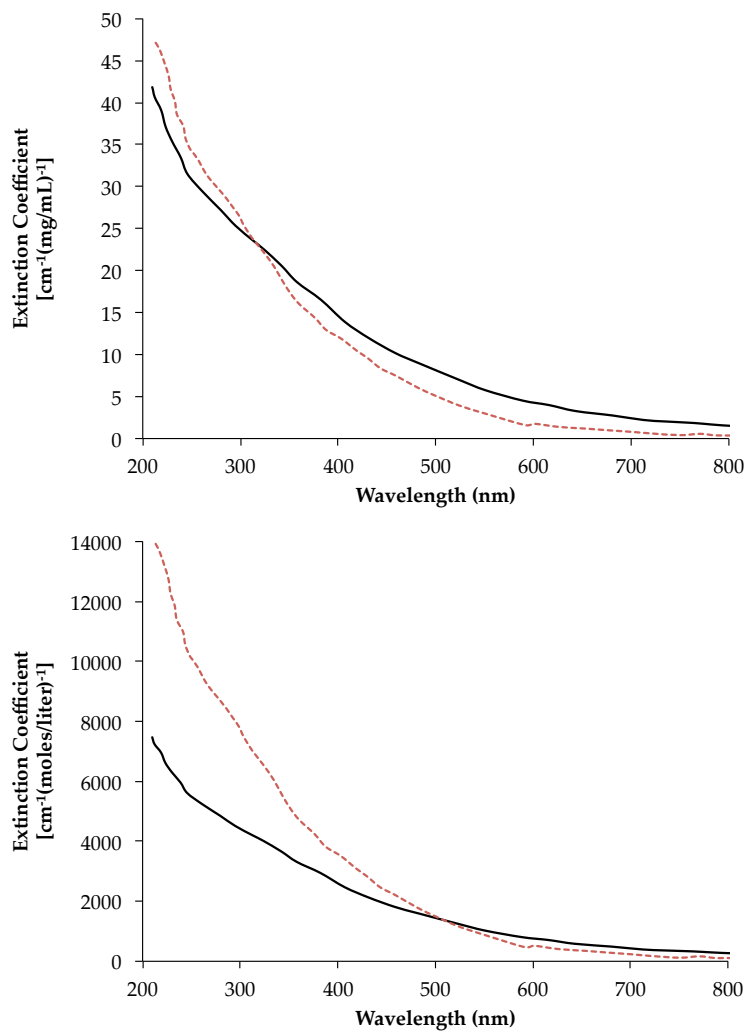


Figure 21: Extinction coefficients as a function of wavelength for eumelanin and pheomelanin. A) Absorption spectra for synthetic eumelanin (solid black line) and pheomelanin (dashed red line) obtained from (Sarna and Swartz, 2006). Extinction coefficients per monomer (B) were calculated from data reported on synthetic melanins in A) (Jacques, 2001). The eumelanin (solid black line) is reported per DHI monomer and pheomelanin is reported per benziothiazine monomer (dashed red line).

monomer plus added molecular weights for linkages (Jacques, 2001). In doing this, several assumptions were made: 1) the melanin polymer is comprised only of the monomers DHI/DHICA or benzothiazines with known molecular weights, 2) the linkages between the subunits are minimal, and 3) the mass measured is reflective of the pigment without attached protein or optically inert moieties. The wavelength dependence of the extinction coefficients of eumelanin and pheomelanin per monomer in units of $(\text{cm}^{-1}(\text{moles/liter})^{-1})$ are shown in **Figure 21B**. The pheomelanin:eumelanin ratio is ~ 1.8 throughout the spectra range examined herein, which is in excellent agreement with the determination of ~ 1.9 arrived at by modeling the calculated ϵc for the pigments with their currently known monomeric chromophores. This agreement suggests that the optical properties of the synthetic and natural pigments are similar.

It is interesting to compare the directly measured absorption spectra for pigments in intact melanosomes with the extinction coefficients of the eumelanin and pheomelanin monomers presented in **Figure 22** (Murphy and Schlutz, 1985; Tran et al., 2006; Wakamatsu et al., 2009). Generally, at wavelengths greater than $\lambda \sim 257$ nm, pheomelanin monomer extinction coefficients are smaller in magnitude than those for eumelanin. Furthermore, while the relative concentrations of DHBTCAs and BZs comprising the pheomelanin of blue-green iridal stroma melanosomes have yet to be quantified, the measured pheomelanin spectrum does not reflect the spectral trend of the two monomers. Additionally, the low energy band of the DHICA monomer does

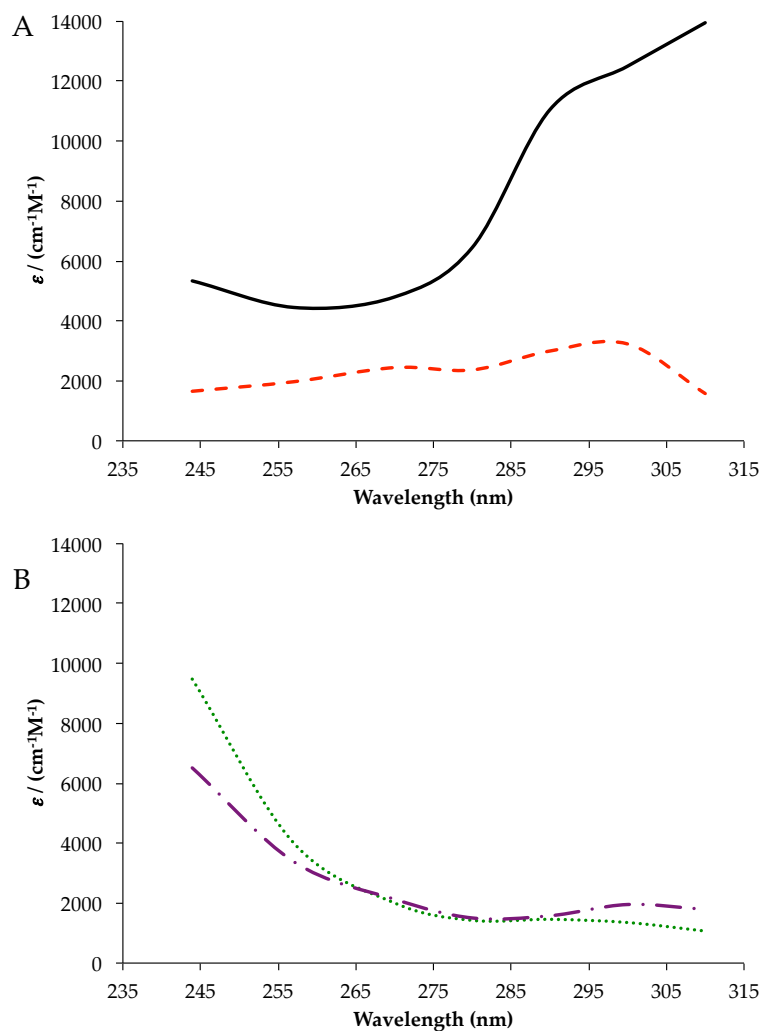


Figure 22: Extinction coefficients of the A) eumelanin and B) pheomelanin monomers. The eumelanin DHICA (—) and DHI (---) monomers are reported from spectra taken in NaOH (Tran et al., 2006) and deaerated water (Murphy and Schlutz, 1985; Jacques and McAuliffe, 1991), respectively. The pheomelanin monomers are reported from spectra of BZ (— ·) and DHBTCa taken in HCl (· · ·) (Wakamatsu et al., 2009).

not influence the measured eumelanin spectrum. These results suggest that the monomers are modified upon polymerization to the resulting melanin oligomers. This result is not unexpected based the work comparing the UV absorption spectra of eumelanin comprised of different DHI:DHICA ratios to the monomeric extinction coefficients (**Chapter 4**). It is important to acknowledge, however, that all of the melanin monomers are known to have fluctuations depending on the solvent and/or pH, but generally maintain the spectral trends plotted in **Figure 22** (Ito and Nicol, 1974; Murphy and Schlutz, 1985; Tran et al., 2006; Gauden et al., 2009; Wakamatsu et al., 2009). The values reported herein for the DHICA and DHI monomers are taken from spectra in NaOH (Tran et al., 2006) and deaerated water (Murphy and Schlutz, 1985), respectively, while the BZ and DHBTCAs monomers are taken from spectra in HCl (Wakamatsu et al., 2009).

Mixtures of eumelanin and pheomelanin are produced in various ratios throughout natural mammalian melanosomes (Ito, 2003; Wakamatsu et al., 2006; Wakamatsu et al., 2007) and epidemiological data has observed increased incidences of skin and ocular cancers for increased relative concentrations of pheomelanin (Vincensi et al., 1998; Wenczl et al., 1998b; Hu et al., 2008). In the context of these observations, a significant effort has been directed towards understanding the functional significance of increased incidences of pheomelanin. To date, however, there is data that both supports (Vincensi et al., 1998; Wenczl et al., 1998a; Wenczl et al., 1998b; Takeuchi et al., 2004;

Samokhvalov et al., 2005; Ye et al., 2006; Ye et al., 2008) and refutes (Sarna and Sealy, 1984b; Sarna et al., 1985; Hennessy et al., 2005) the possible causative role of pheomelanin. The work described herein on intact melanosomes offers a new viewpoint to this debate. The present work indicates that the photoprotective role of the melanosomes is maintained with increased pheomelanin content, as the absorption coefficient at biologically relevant wavelengths is similar on a per melanosome basis. The correlation between epidemiological data and the eumelanin/pheomelanin ratio is predicted to not be a reflection of the melanosome's decreased ability to attenuate biologically relevant wavelengths, but perhaps is instead a reflection of the different photoreactivities of the melanin pigments contained within. This prediction is further supported by the casing model, **Chapter 3**, as the photoprotective, antioxidant eumelanin pigment is thinner for increased relative pheomelanin concentrations. The thinner shell is more susceptible to degradation, and subsequent exposure of the reactive, pro-oxidant pheomelanin core. Further progress in this area depends on determining the quantum efficiency for oxygen activation from studies on intact natural melanosomes.

5.4 Conclusions

The wavelength-dependent quantification of the absorption coefficients of the natural melanins in intact melanosomes, presented herein, reveal that the absorption of the melanosome is independent of its eumelanin:pheomelanin ratio. Modeling the

pigment in terms of the currently known monomeric chromophores, suggests that the extinction coefficient of pheomelanin monomer is greater than that of eumelanin throughout the spectral range examined, similar to what has been deduced from studies of soluble synthetic pigments. These results suggest that on the volume of the melanosome, the correlation between epidemiological data and the eumelanin:pheomelanin ratio is not predicted to be a reflection of a decreased ability to attenuate biologically relevant wavelengths. Thus, because photoprotection is conserved with increased concentrations of pheomelanin, photoreactivity differences are suggested to be the cause of the observed correlation.

References

- Ade, H.; Yang, W.; English, S. L.; Hartman, J.; Davis, R.; Nemanich, R.; Litvinenko, V.; Pinayev, I. V.; Wu, Y. and Madey, J. M. J. (1998) A free electron laser-photoemission electron microscope system (FEL- PEEM). *Surf. Rev. Lett.*, **5**: 1257-1268.
- Agrup, G.; Hansson, C.; Rorsman, H. and Rosengren, E. (1982) The effect of cysteine on oxidation of tyrosine dopa, and cysteinyl dopas. *Arch. Dermatol. Res.*, **272**: 103-115.
- Bauer, E. (1994) Surface electron microscopy: the first thirty years. *Surf. Sci.*, **299/300**: 102-115.
- Benathan, M. and Wyler, H. (1980) Quantitative approaches to melanin structure. *Yale J. Bio. Med.*, **53**: 389-390.
- Benigni, J. D. and Minnis, R. (1965) The synthesis of 5,6-dihydroxyindole and some of its derivatives (1). *J. Hetero. Chem.*, **2**: 387-392.
- Bertrand, G. (1896) Sur une nouvelle oxydase, ou ferment soluble oxydant, d'origine vegetale. *Comp. Rend. Soc. Biol. (Paris)*, **112**: 1215-1217.
- Bethge, H. and Klaua, M. (1983) Photo-electron emission microscopy of work function changes. *Ultramicroscopy*, **11**: 207-214.
- Birrell, G.; Habliston, D. and Nadakavukaren, K. (1985) Immunophotoelectron microscopy: the electron optical analog of immunofluorescence microscopy. *Proc. Natl. Acad. Sci. USA*, **82**: 109-113.
- Birrell, G. B.; Habliston, D. L. and Griffith, O. H. (1994) Photoelectron imaging of viruses and DNA: evaluation of substrates by unidirectional low angle shadowing and photoemission current measurements. *Biophys. J.*, **67**: 2041-2047.
- Birrell, G. B.; Hedberg, K. K.; Habliston, D. L. and Griffith, O. H. (1991) Biological applications of photoelectron imaging: a practical perspective. *Ultramicroscopy*, **36**: 235-251.
- Birrell, G. B.; Rose, S. M. and Griffith, O. H. (1983) Photoelectron microscopy of erythrocyte ghosts; imaging of lectin binding sites with colloidal gold markers. *Ultramicroscopy*, **12**: 213-218.
- Bloch, B. and Schaaf, F. (1925) Pigment studien. *Biochem. Z.*, **162**: 181-206.

- Boissy, R. E. and Hornyak, T. J. (2006) Extracutaneous Melanocytes. In *The Pigmentary System: Physiology and Pathology* 2nd Edition (Norlund, J. J., Boissy, R. E., Hearing, V. J., King, R. A., Oetting, W. S. and Ortonne, J.-P., Eds.) pp. 91-107. Malden: Blackwell Publishing.
- Borovansky, J. and Duchon, J. (1974) Chemical composition of hair melanosomes. *Dermatologica*, **149**: 116-120.
- Borovansky, J. and Hach, P. (1973) Comments on Bolt's Tumour melanoprotein. *Neoplasma*, **20**: 325-329.
- Boulton, M.; Docchio, F.; Dayhaw-Barker, P.; Ramponi, R. and Cubeddu, R. (1990) Age-related changes in the morphology, absorption and fluorescence of melanosomes and lipofuscin granules of the retinal pigment epithelium. *Vision Res.*, **30**: 1291-1303.
- Bourquelot, E. and Bertrand, G. (1895) Le bleuissement et le noircissement des champignons. *Comp. Rend. Soc. Biol. (Paris)*, **2**: 582-584.
- Brinkmann, R.; Huttman, G.; Rogener, J.; Roider, J.; Birngruber, R. and Lin, C. P. (2000) Origin of retinal pigment epithelium cell damage by pulsed laser irradiance in the nanosecond to microsecond time regimen. *Lasers Surg. Med.*, **27**: 451-464.
- Brüche, E. (1933) Elektronenmikroskopische abbildung mit lichtelektrischen elektronen. *Z. Phys.*, **86**: 448-450.
- Brumbaugh, J. A. (1968) Ultrastructural differences between forming eumelanin and pheomelanin as revealed by the pink-eye mutation in the fowl. *Dev. Biol.*, **18**: 375-390.
- Buckanie, N. M.; Göhre, J.; Zhou, P.; von der Linde, D.; Horn-Von Hoegen, M. and Meyer Zu Heringdorf, F.-J. (2009) Space charge effects in photoemission electron microscopy using amplified femtosecond laser pulses. *J. Phys.: Condens. Matter*, **21**: 314003.
- Bumsted, K. M. and Barnstable, J. C. (2000) Dorsal retinal pigment epithelium differentiate as neural retina in microphthalmia(mi/mi) mouse. *Invest. Ophthalmol. Vis. Sci.*, **41**: 903-908.
- Bush, W. D.; Garguilo, J.; Zucca, F. A.; Albertini, A.; Zecca, L.; Edwards, G. S.; Nemanich, R. J. and Simon, J. D. (2006) The surface oxidation potential of human

- neuromelanin reveals a spherical architecture with a pheomelanin core and a eumelanin surface. *Proc. Natl. Acad. Sci. USA*, **103**: 14785-14789.
- Bush, W. D.; Garguilo, J.; Zucca, F. A.; Bellei, C.; Nemanich, R. J.; Edwards, G. S.; Zecca, L. and Simon, J. D. (2009) Neuromelanins isolated from different regions of the human brain exhibit a common surface photoionization threshold. *Photochem. Photobiol.*, **85**: 387-390.
- Bustamante, J.; Bredeston, L.; Malanga, G. and Mordoh, J. (1993) Role of melanin as a scavenger of active oxygen species. *Pigment Cell Res.*, **6**: 348-353.
- Chedekel, M. R.; Agin, P. P. and Sayre, R. M. (1980) Photochemistry of pheomelanin: Action spectrum for superoxide production. *Photochem. Photobiol.*, **31**: 553-555.
- Chedekel, M. R.; Smith, S. K.; Post, P. W.; Pokora, A. and Vessel, D. L. (1978) Photodestruction of pheomelanin: Role of oxygen. *Proc. Natl. Acad. Sci. USA*, **75**: 5395-5399.
- Chelaru, L.; Horn-Von Hoegen, M.; Thien, D. and Zu, F. (2006) Fringe fields in nonlinear photoemission microscopy. *Phys. Rev. B*, **73**: 115416.
- Clancy, C. M. R. and Simon, J. D. (2001) Ultrastructural organization of eumelanin from *Sepia officinalis* measured by atomic force microscopy. *Biochemistry*, **40**: 13353-13360.
- Cress, R. D. and Holly, E. A. (1997) Incidence of cutaneous melanoma among non-hispanic whites, hispanics, asians, and blacks: an analysis of California Cancer Registry data, 1988-93. *Cancer Causes Control*, **8**: 246-252.
- Crippa, P. R.; Cristofolletti, V. and Romeo, N. (1978) A band model for melanin deduced from optical-absorption and photoconductivity experiments. *Biochim. Biophys. Acta*, **538**: 164-170.
- d'Ischia, M.; Crescenzi, O.; Pezzella, A.; Arzillo, M.; Panzella, L.; Napolitano, A. and Barone, V. (2008) Structural effects on the electronic absorption properties of 5,6-dihydroxyindole oligomers: The potential of an integrated experimental and DFT approach to model eumelanin optical properties. *Photochem. Photobiol.*, **84**: 600-607.
- Dam, R. J.; Nadakavukaren, K. K. and Griffith, O. H. (1977) Photoelectron microscopy of cell surfaces. *J. Microsc.*, **111**: 211-217.

- Davies, T. W.; Treasure, F. P.; Welch, A. A. and Day, N. E. (2002) Diet and basal cell skin cancer: Results from the EPIC-Norfolk Cohort. *Brit. J. Dermatol.*, **146**: 1017-1022.
- Dryja, T. P.; Oneildryja, M. and Albert, D. M. (1979) Elemental analysis of melanins from bovine hair, iris, choroid, and retinal-pigment epithelium. *Invest. Ophthalmol. Vis. Sci.*, **18**: 231-236.
- Ehsasi, M. (1994) Application of photoemission electron microscopy to the study of surface reactions. *Appl. Surf. Sci.*, **76/77**: 89-100.
- Fattorusso, E.; Minale, L.; De Stefano, S.; Cimino, G. and Nicolaus, R. A. (1968) Struttura e biogenesi delle feomelanine. Nota V. Sulla struttura della gallofeomelanina-1. *Gazz. Chim. Ital.*, **98**: 1443-1463.
- Felix, C. C.; Hyde, J. S.; Sarna, T. and Sealy, R. C. (1978) Melanin photoreactions in aerated media: Electron-spin resonance evidence for production of superoxide and hydrogen-peroxide. *Biochem. Biophys. Res. Commun.*, **84**: 335-341.
- Fowler, R. (1931) The analysis of photoelectric sensitivity curves for clean metals at various temperatures. *Phys. Rev. A*, **38**: 45-56.
- Garguilo, J.; Hong, L.; Edwards, G. S.; Nemanich, R. J. and Simon, J. D. (2007) The surface oxidation potential of melanosomes measured by free electron laser-photoelectron emission microscopy. *Photochem. Photobiol.*, **83**: 692-697.
- Gauden, M.; Pezzella, A.; Panzella, L.; Napolitano, A.; d'Ischia, M. and Sundström, V. (2009) Ultrafast excited state dynamics of 5,6-dihydroxyindole, a key eumelanin building block: nonradiative decay mechanism. *J. Phys. Chem. B*, **113**: 12575-12580.
- Glickman, R.; Jacques, S.; Hall, R. and Kumar, N. (2001) Revisiting the internal absorption coefficient of the retinal pigment epithelium melanosome. *Proc. SPIE*, **4257**: 134-141.
- Glickman, R. D.; Jacques, S. L.; Schwartz, J. A.; Rodriguez, T.; Lam, K.-W. and Buhr, G. (1996) Photodisruption increases the free radical reactivity of melanosomes isolated from retinal pigment epithelium. *Proc. SPIE*, **2681**: 460-467.
- Griffith, O. (1986) Photoelectron microscopy: Applications to biological surfaces. *Appl. Surf. Sci.*, **26**: 265-279.

- Griffith, O. and Rempfer, G. (1985) Photoelectron imaging in cell biology. *Ann. Rev. Biophys. Biophys. Chem.*, **14**: 113-130.
- Griffith, O. and Rempfer, G. (1988) Photoelectron imaging and photoelectron labeling. *Ultramicroscopy*, **24**: 299-312.
- Griffith, O. H. and Birrell, G. B. (1985) Photoelectron microscopy. *Trends Biochem. Sci.*, **10**: 336-339.
- Griffith, O. H. and Engle, W. (1991) Historical perspective and current trends in emission microscopy, mirror electron microscopy and low-energy electron microscopy. *Ultramicroscopy*, **36**: 1-28.
- Griffith, O. H.; Habliston, D. L.; Birrell, G. B. and Schabtach, E. (1990) Photoelectron imaging of DNA. *Biopolymers*, **29**: 1491-1493.
- Griffith, O. H.; Lesch, G. H.; Rempfer, G. F.; Birrell, G. B.; Burke, C. A.; Schlosser, D. W.; Mallon, M. H.; Lee, G. B.; Stafford, R. G.; Jost, P. C. and Marriott, T. B. (1972) Photoelectron microscopy: a new approach to mapping organic and biological surfaces. *Proc. Natl. Acad. Sci. USA*, **69**: 561-565.
- Grund, S.; Eichberg, J. and Engel, W. (1979) Photoelectron emission microscopy of biological tissue; the influence of glutaraldehyde and heavy metals or biligrafin on the emission image of chicken liver in methacrylate *Ultramicroscopy*, **4**: 293-304.
- Guenther, R. D. (1990) Fresnel Diffraction. In *Modern Optics* pp. 463. New York: John Wiley & Sons.
- Habliston, D. L.; Birrell, G. B.; Griffith, O. H. and Rempfer, G. F. (1993) Photoelectron imaging of DNA: a study of substrates and contrast. *J. Phys. Chem.*, **97**: 3022-3027.
- Habliston, D. L.; Hedberg, K. K.; Birrell, G. B.; Rempfer, G. F. and Griffith, O. H. (1995) Photoelectron imaging of cells: photoconductivity extends the range of applicability. *Biophys. J.*, **69**: 1615-1624.
- Harsanyi, Z. P.; Post, P. W.; Brinkmann, J. P.; Chedekel, M. R. and Deibel, R. M. (1980) Mutagenicity of melanin from human red hair. *Experientia*, **36**: 291-292.
- Hennessy, A.; Oh, C.; Diffey, B.; Wakamatsu, K.; Ito, S. and Rees, J. (2005) Eumelanin and pheomelanin concentrations in human epidermis before and after UVB irradiation. *Pigment Cell Res.*, **18**: 220-223.

- Hill, H. Z. (1992) The function of melanin or six blind people examine an elephant. *BioEssays*, **14**: 49-56.
- Holly, E. (1990) Uveal melanoma in relation to ultraviolet light exposure and host factors. *Cancer Res.*, **50**: 5773-5777.
- Hong, L.; Garguilo, J.; Anzaldi, L.; Edwards, G. S.; Nemanich, R. J. and Simon, J. D. (2006) Age-dependent photoionization thresholds of melanosomes and lipofuscin isolated from human retinal pigment epithelium cells. *Photochem. Photobiol.*, **82**: 1475-1481.
- Houle, W. A.; Engel, W.; Willig, F.; Rempfer, G. F. and Griffith, O. H. (1982) Depth of information in photoelectron microscopy. *Ultramicroscopy*, **7**: 371-380.
- Houle, W. A. and Griffith, O. H. (1983a) Imaging of DNA by photoelectron microscopy. *Micron Microsc. Acta*, **14**: 351-352.
- Houle, W. A. and Griffith, O. H. (1983b) Photoelectron microscopy of viruses. *Ultramicroscopy*, **11**: 71-74.
- Hu, D.; McCormick, S.; Ritch, R. and Pelton-Henrion, K. (1993) Studies of human uveal melanocytes in vitro: isolation, purification and cultivation of human uveal melanocytes. *Invest. Ophthalmol. Vis. Sci.*, **34**: 2210-2219.
- Hu, D.; Simon, J. and Sarna, T. (2008) Role of ocular melanin in ophthalmic physiology and pathology. *Photochem. Photobiol.*, **84**: 639-644.
- Hu, D.; Yu, G.; McCormick, S.; Schneider, S. and Finger, P. (2005) Population-based incidence of uveal melanoma in various races and ethnic groups. *Am. J. Ophthalmol.*, **140**: 612.e611- 612.e618.
- Hu, D.-N.; Wakamatsu, K.; Ito, S. and McCormick, S. A. (2009) Comparison of eumelanin and pheomelanin content between cultured uveal melanoma cells and normal uveal melanocytes. *Melanoma Res.*, **19**: 75-79.
- Hu, D. N.; Ritch, R.; McCormick, S. A. and Peltonhenrion, K. (1992) Isolation and cultivation of human iris pigment epithelium. *Invest. Ophthalmol. Vis. Sci.*, **33**: 2443-2453.
- Hubbard-Smith, K.; Hill, H. Z. and Hill, G. J. (1992) Melanin both causes and prevents oxidative base damage in DNA: Quantification by anti-thymine glycol antibody. *Radiat. Res.*, **130**: 160-165.

- Ito, S. (1989) Optimization of conditions for preparing synthetic pheomelanin. *Pigment Cell Res.*, **2**: 53-56.
- Ito, S. (2003) A Chemist's view of melanogenesis. *Pigment Cell Res.*, **16**: 230-236.
- Ito, S. (2006) Encapsulation of a reactive core in neuromelanin. *Proc. Natl. Acad. Sci. USA*, **103**: 14647-14648.
- Ito, S. and Fujita, K. (1985) Microanalysis of eumelanin and pheomelanin in hair and melanomas by chemical degradation and liquid-chromatography. *Anal. Biochem.*, **144**: 527-536.
- Ito, S. and Jimbow, K. (1983) Quantitative analysis of eumelanin and pheomelanin in hair and melanomas. *J. Invest. Derm.*, **80**: 268-272.
- Ito, S. and Nicol, J. A. C. (1974) Isolation of oligomers of 5,6-dihydroxyindole-2-carboxylic acid from the eye of the catfish. *Biochem. J.*, **143**: 207-217.
- Ito, S. and Wakamatsu, K. (2003) Quantitative analysis of eumelanin and pheomelanin in humans, mice, and other animals: a comparative review. *Pigment Cell Res.*, **16**: 523-531.
- Ito, S. and Wakamatsu, K. (2006) Chemistry of Melanins. In *The Pigmentary System: Physiology and Pathophysiology* 2nd Edition (Norlund, J. J., Boissy, R. E., Hearing, V. J., King, R. A., Oetting, W. S. and Ortonne, J.-P., Eds.) pp. 282-310. Malden: Blackwell Publishing.
- Ito, S. and Wakamatsu, K. (2008) Chemistry of mixed melanogenesis - pivotal roles of dopaquinone. *Photochem. Photobiol.*, **84**: 582-592.
- Ito, S.; Wakamatsu, K. and Ozeki, H. (2000) Chemical analysis of melanins and its application to the study of the regulation of melanogenesis. *Pigment Cell Res.*, **13**: 103-109.
- Jacques, S. (2001) Optical Absorption of Melanin. <http://omlc.ogi.edu/spectra/melanin/> Accessed 9 June 2011.
- Jacques, S.; Glickman, R. and Schwartz, J. (1996) Internal absorption coefficient and threshold for pulsed laser disruption of melanosomes isolated from retinal pigment epithelium. *Proc. SPIE*, **2681**: 468-477.

- Jacques, S. L. and McAuliffe, D. J. (1991) The melanosome: threshold temperature for explosive vaporization and internal absorption coefficient during pulsed laser irradiation. *Photochem. Photobiol.*, **53**: 769-775.
- Kathuria, Y. P. (1985) Fresnel and far-field diffraction due to an elliptical aperture. *J. Opt. Soc. Am. A*, **2**: 852-857.
- Kollias, N.; Sayre, R. M.; Zeise, L. and Chedekel, M. R. (1991) Photoprotection by melanin. *J. Photochem. Photobiol. B: Biol.*, **9**: 135-160.
- Kordesch, M. E. (1995) Photoelectron emission microscopy. In *The Handbook of Surface Imaging and Visualization* (Hubbard, A. T., Ed. pp. 581-596. Boca Raton, FL: CRC Press, Inc.
- Korytowski, W.; Kalyanaraman, B.; Menon, I. A.; Sarna, T. and Sealy, R. C. (1986) Reaction of superoxide anions with melanins: electron spin resonance and spin trapping studies. *Biochim. Biophys. Acta*, **882**: 145-153.
- Korytowski, W.; Pilas, B.; Sarna, T. and Kalyanaraman, B. (1987) Photoinduced generation of hydrogen peroxide and hydroxyl radicals in melanins. *Photochem. Photobiol.*, **45**: 185-190.
- Land, E. J.; Ito, S.; Wakamatsu, K. and Riley, P. A. (2003) Rate constants for the first two chemical steps of eumelanogenesis. *Pigment Cell Res.*, **16**: 487-493.
- Land, E. J. and Riley, P. A. (2000) Spontaneous redox reactions of dopaquinone and the balance between the eumelanin and pheomelanin pathways. *Pigment Cell Res.*, **13**: 273-277.
- Li, W.; Goto, K. and Shimizu, R. (2005) PEEM is a suitable tool for absolute work function measurements. *Surf. Interface Anal.*, **37**: 244-247.
- Littre, A. (1720) *Histoire de l'academie royale des sciences*. Paris: Hochereau.
- Liu, Y.; Hong, L.; Wakamatsu, K.; Ito, S.; Adhyaru, B.; Cheng, C.-Y.; Bowers, C. R. and Simon, J. D. (2005a) Comparison of structural and chemical properties of black and red human hair melanosomes. *Photochem. Photobiol.*, **81**: 135-144.
- Liu, Y.; Hong, L.; Wakamatsu, K.; Ito, S.; Adhyaru, B. B.; Cheng, C.-Y.; Bowers, C. R. and Simon, J. D. (2005b) Comparisons of the structural and chemical properties of melanosomes isolated from retinal pigment epithelium, iris and choroid of newborn and mature bovine eyes. *Photochem. Photobiol.*, **81**: 510-516.

- Liu, Y.; Kempf, V. R.; Nofsinger, J. B.; Weinert, E. E.; Rudnicki, M.; Wakamatsu, K.; Ito, S. and Simon, J. D. (2003) Comparison of the structural and physical properties of human hair eumelanin following enzymatic or acid/base extraction. *Pigment Cell Res.*, **16**: 355-365.
- Liu, Y. and Simon, J. D. (2003) Isolation and biophysical studies of natural eumelanins: Applications of imaging technologies and ultrafast spectroscopy. *Pigment Cell Res.*, **16**: 606-618.
- Mason, H. S. (1948) The chemistry of melanin. III. Mechanism of the oxidation of dihydroxyphenylalanine by tyrosinase. *J. Biol. Chem.*, **172**: 83-92.
- Meredith, P. and Sarna, T. (2006) The physical and chemical properties of eumelanin. *Pigment Cell Res.*, **19**: 572-594.
- Michelson, J. B. and Shields, J. A. (1977) Relationship of iris nevi to malignant melanoma of the uvea. *Am. J. Ophthalmol.*, **83**: 694-696.
- Minale, L.; Fattorusso, E.; Cimino, G.; De Stefano, S. and Nicolaus, R. A. (1967) Structure and biogenesis of pheomelanins. II. Degradation products. *Gazz. Chim. Ital.*, **97** 1636-1663.
- Mundschau, M. (1991) Emission microscopy and surface science. *Ultramicroscopy*, **26**: 29-51.
- Mundschau, M.; Kordesch, M. E.; Rausenberger, B.; Engel, W.; Bradshaw, A. M. and Zeitler, E. (1990) Real-time observation of the nucleation and propagation of reaction fronts on surfaces using photoemission electron microscopy. *Surf. Sci.*, **227**: 246-260.
- Murphy, B. P. and Schlutz, T. M. (1985) Synthesis and physical properties of 5,6-dihydroxyindole. *J. Org. Chem.*, **50**: 2790-2791.
- Nadakavukaren, K. K. and Griffith, O. H. (1985) Photoelectron imaging of cytoskeletal elements. *Ultramicroscopy*, **17**: 31-42.
- Nadakavukaren, K. K.; Rempfer, G. F. and Griffith, O. H. (1981) Photoelectron microscopy of cell surface topography. *J. Microsc.*, **122**: 301-307.
- Nakano, Y.; Nakane, H. and Adachi, H. (2008) Work function measurement of modified W(100) surface with transition metal by photoemission electron microscopy. *Jpn. J. Appl. Phys.*, **47**: 1713-1716.

- Nepijko, S. A.; Sedov, N. N.; Schmidt, O.; Schonhense, G.; Bao, X. and Huang, W. (2001) Imaging of three-dimensional objects in emission electron microscopy. *J. Microsc.*, **202**: 480-487.
- Neugut, A. I.; Kizelnik-Freilich, S. and Ackerman, C. (1994) Black-white differences in risk for cutaneous, ocular, and visceral melanomas. *Am. J. Public Health*, **84**: 1828-1829.
- Neumann, J. and Brinkmann, R. (2005) Boiling nucleation on melanosomes and microbeads transiently heated by nanosecond and microsecond laser pulses. *J. Biomed. Opt.*, **10**: 024001.
- Nicolaus, R. A. (1968) *Melanins*. Paris: Hermann Press.
- Nofsinger, J. B.; Forest, S. E. and Simon, J. D. (1999) Explanation for the disparity among absorption and action spectra of eumelanin. *J. Phys. Chem. B*, **103**: 11428-11432.
- Nofsinger, J. B.; Liu, Y. and Simon, J. D. (2002a) Aggregation of eumelanin mitigates photogeneration of reactive oxygen species. *Free Rad. Biol. Med.*, **32**: 720-730.
- Nofsinger, J. B.; Weinert, E. E. and Simon, J. D. (2002b) Establishing structure function relationships for eumelanin. *Biopolymers*, **67**: 302-305.
- Nordlund, J. J. (1989) The lives of pigment cells. *J. Geriatr. Dermatol.*, **5**: 91-108.
- Oskooi, A. F.; Roundy, D.; Ibanescu, M.; Bermel, P.; Joannopoulos, J. D. and Johnson, S. G. (2010) Meep: A flexible free-software package for electromagnetic simulations by the FDTD method. *Comput. Phys. Commun.*, **181**: 687-702.
- Ozeki, H.; Ito, S.; Wakamatsu, K. and Ishiguro, I. (1997a) Chemical characterization of pheomelanogenesis starting from dihydroxyphenylalanine or tyrosine and cysteine. Effects of tyrosinase and cysteine concentrations and reaction time. *Biochim. Biophys. Acta*, **1336**: 539-548.
- Ozeki, H.; Wakamatsu, K.; Ito, S. and Ishiguro, I. (1997b) Chemical characterization of eumelanins with special emphasis on 5,6-dihydroxyindole-2-carboxylic acid content and molecular size. *Anal. Biochem.*, **248**: 149-157.
- Panizzi, L. and Nicolaus, R. A. (1952) Ricerche sulle melanine. *Gazz. Chim. Ital.*, **82**: 435-460.

- Peles, D. N.; Hong, L.; Hu, D.-N.; Ito, S.; Nemanich, R. J. and Simon, J. D. (2009) Human iridal stroma melanosomes of varying pheomelanin contents possess a common eumelanic outer surface. *J. Phys. Chem. B*, **113**: 11346-11351.
- Peles, D. N.; Lin, E.; Wakamatsu, K.; Ito, S. and Simon, J. D. (2010) Ultraviolet absorption coefficients of melanosomes containing eumelanin as related to the relative content of DHI and DHICA. *J. Phys. Chem. Lett.*, **1**: 2391-2395.
- Peles, D. N. and Simon, J. D. (2009) Challenges in applying photoemission electron microscopy to biological systems. *Photochem. Photobiol.*, **85**: 8-20.
- Peles, D. N. and Simon, J. D. (2010a) Direct measurement of the ultraviolet absorption coefficient of single retinal melanosomes. *Photochem. Photobiol.*, **86**: 279-281.
- Peles, D. N. and Simon, J. D. (2010b) The ultraviolet absorption coefficient of melanosomes decreases with increasing pheomelanin content. *J. Phys. Chem. B*, **114**: 9677-9683.
- Persad, S.; Menon, I. A. and Haberman, H. F. (1983) Comparison of the effects of UV-visible irradiation of melanins and melanin-hematoporphyrin complexes from human black and red hair. *Photochem. Photobiol.*, **37**: 63-68.
- Pezzella, A.; Iadonisi, A.; Valerio, S.; Panzella, L.; Napolitano, A.; Adinolfi, M. and d'Ischia, M. (2009a) Disentangling eumelanin "black chromophore": Visible absorption changes as signatures of oxidation state- and aggregation-dependent dynamic interactions in a model water-soluble 5,6-dihydroxyindole polymer. *J. Am. Chem. Soc.*, **131**: 15270-15275.
- Pezzella, A.; Panzella, L.; Crescenzi, O.; Napolitano, A.; Navaratnam, S.; Edge, R.; Land, E. J.; Barone, V. and d'Ischia, M. (2009b) Lack of visible chromophore development in the pulse radiolysis oxidation of 5,6-dihydroxyindole-2-carboxylic acid oligomers: DFT investigation and implications for eumelanin absorption properties. *J. Org. Chem.*, **74**: 3727-3734.
- Piattelli, M.; Fattorusso, E.; Magno, S. and Nicolaus, R. A. (1962) Structure of melanins and melanogenesis. II. Sepiomelanin and synthetic pigments. *Tetrahedron*, **18**: 941-949.
- Prota, G. (1992) *Melanins and Melanogenesis*. San Diego: Academic Press, Inc.

- Prota, G.; Hu, D. N.; Vincensi, M. R.; McCormick, S. A. and Napolitano, A. (1998) Characterization of melanins in human irides and cultured uveal melanocytes from eyes of different colors. *Exp. Eye Res.*, **67**: 293-299.
- Prota, G., Ischia M. D., Napolitano A. (1998) The Chemistry of Melanins and Related Metabolites. In *The Pigmentary System* (Nordlund J. J., B. R. E., Hearing V. J., King R. A., Ortonne J. P., Ed. pp. 307-332. New York: Oxford University Press.
- Prota, G. and Nicolaus, R. A. (1967a) On the Biogenesis of Phaeomelanins. In *Advances in Biology of Skin* (Montagna, W. and Hu, F., Eds.) Vol. 8: pp. 323-328. New York: Pergamon Press.
- Prota, G. and Nicolaus, R. A. (1967b) Struttura e biogenesi delle feomelanine. Nota I. Isolamento e proprietà dei pigmenti delle piume. *Gazz. Chim. Ital.*, **97**: 665-684.
- Prota, G.; Piattelli, M. and Nicolaus, R. A. (1966) Preliminary results in the study of phaeomelanins. *Rend. Accad. Sci. Mat. Fis.*, **33**: 146-150.
- Raper, H. S. (1927) The tyrosinase-tyrosine reaction. VI. Production from tyrosine of 5,6-dihydroxyindole and 5,6-dihydroxyindole-2-carboxylic acid the precursor of melanin. *Biochem. J.*, **21**: 89-96.
- Rempfer, G. F.; Nadakavukaren, K. K. and Griffith, O. H. (1980) Topographical effects in emission microscopy. *Ultramicroscopy*, **5**: 437-448.
- Riesz, J.; Gilmore, J.; McKenzie, R.; Powell, B.; Pederson, M. and Meredith, P. (2007) Transition dipole strength of eumelanin. *Phys. Rev. E*, **76**: 021915.
- Riesz, J.; Gilmore, J. and Meredith, P. (2006) Quantitative scattering of melanin solutions. *Biophys. J.*, **90**: 4137-4144.
- Rotermund, H. H. (1993) Investigation of dynamic processes in adsorbed layers by photoemission electron microscopy (PEEM). *Surf. Sci.*, **283**: 87-100.
- Rózanowska, M.; Sarna, T.; Land, E. J. and Truscott, T. G. (1999) Free radical scavenging properties of melanin interaction of eu- and pheo-melanin models with reducing and oxidising radicals. *Free Rad. Biol. Med.*, **26**: 518-525.
- Samokhvalov, A.; Garguilo, J.; Yang, W.-C.; Edwards, G. S.; Nemanich, R. J. and Simon, J. D. (2004) Photoionization threshold of eumelanosomes determined using UV free electron laser-photoelectron emission microscopy. *J. Phys. Chem.*, **108**: 16334-16338.

- Samokhvalov, A.; Hong, L.; Liu, Y.; Garguilo, J.; Nemanich, R. J.; Edwards, G. S. and Simon, J. D. (2005) Oxidation potentials of human eumelanosomes and pheomelanosomes. *Photochem. Photobiol.*, **81**: 145-148.
- Santorius, S. (1614) *De statica medicina et de responsione ad statica masticem. Sphorismorum sectionibus septem comprehensa*. Venice: Marcantonio Brogiollo.
- Sardar, D. K.; Mayo, M. L. and Glickman, R. D. (2001) Optical characterization of melanin. *J. Biomed. Opt.*, **6**: 404-410.
- Sarna, T. (1992) Properties and function of the ocular melanin - a photobiophysical view. *J. Photochem. Photobiol. B-Biol.*, **12**: 215-258.
- Sarna, T.; Froncisz, W. and Hyde, J. S. (1980) Cu²⁺ probe of metal-ion binding-sites in melanin using electron-paramagnetic resonance spectroscopy. II. Natural melanin. *Arch. Biochem. Biophys.*, **202**: 304-313.
- Sarna, T.; Menon, I. A. and Sealy, R. C. (1984) Photoinduced oxygen consumption in melanin systems-II. Action spectra and quantum yields for pheomelanins. *Photochem. Photobiol.*, **39**: 805-809.
- Sarna, T.; Menon, I. A. and Sealy, R. C. (1985) Photosensitization of melanins - a comparative study. *Photochem. Photobiol.*, **42**: 529-532.
- Sarna, T.; Pilas, B.; Land, E. J. and Truscott, T. G. (1986) Interaction of radicals from water radiolysis with melanin. *Biochim. Biophys. Acta*, **883**: 162-167.
- Sarna, T. and Sealy, R. C. (1984a) Free radicals from eumelanins: Quantum yields and wavelength dependence. *Arch. Biochem. Biophys.*, **232**: 574-578.
- Sarna, T. and Sealy, R. C. (1984b) Photoinduced oxygen consumption in melanin systems. Action spectra and quantum yields for eumelanin and synthetic melanin. *Photochem. Photobiol.*, **39**: 69-74.
- Sarna, T. and Swartz, H. A. (2006) The Physical Properties of Melanins. In *The Pigmentary System* 2nd Edition (Nordlund, J. J., Boissy, R. E., Hearing, V. J., King, R. A., Oetting, W. S. and Ortonne, J.-P., Eds.) pp. 311-341. Malden: Blackwell Publishing.
- Schraermeyer, U. and Heimann, K. (1999) Current understanding on the role of retinal pigment epithelium and its pigmentation. *Pigment Cell Res.*, **12**: 219-236.

- Seagle, B.-L. L.; Rezai, K. A.; Gasyna, E. M.; Kobori, Y.; Rezaei, K. A. and James R. Norris, J. (2005) Time-resolved detection of melanin free radicals quenching reactive oxygen species. *J. Am. Chem. Soc.*, **127**: 11220-11221.
- Seddon, J. M.; Gragoudas, E. S.; Glynn, R. J.; Egan, K. M.; Albert, D. M. and Blitzer, P. H. (1990) Host factors, UV radiation, and risk of uveal melanoma. *Arch. Ophthalmol.*, **108**: 1274-1280.
- Senturia, S. D. (2001) *Microsystem Design*. Boston: Kluwer Academic Publishers.
- Simon, J. D.; Hong, L. and Peles, D. N. (2008) Insights into melanosomes and melanin from some interesting spatial and temporal properties. *J. Phys. Chem. B*, **112**: 13201-13217.
- Strauss, M.; Amendt, P. A.; London, R. A.; Maitland, D. J.; Glinsky, M. E.; Lin, C. P. and Kelly, M. W. (1997) Computational modeling of stress transient and bubble evolution in short-pulse laser irradiated melanosome particles. *Proc. SPIE*, **2975**: 261-270.
- Taflove, A. and Hagness, S. C. (2000) *Computational Electrodynamics: The Finite-Difference Time-Domain Method*. Norwood: Artech.
- Takeuchi, S.; Zhang, W.; Wakamatsu, K.; Ito, S.; Hearing, V. J.; Kraemer, K. H. and Brash, D. E. (2004) Melanin acts as a potent UVB photosensitizer to cause an atypical mode of cell death in murine skin. *Proc. Natl. Acad. Sci. USA*, **101**: 15076-15081.
- Tran, M.; Powell, B. and Meredith, P. (2006) Chemical and structural disorder in eumelanins: a possible explanation for broadband absorbance. *Biophys. J.*, **90**: 743-752.
- Tsai, T.; Vu, C. and Henson, D. E. (2005) Cutaneous, ocular and visceral melanoma in African Americans and Caucasians. *Melanoma Res.*, **15**: 213-217.
- Tucker, M. A.; Shields, J. A.; Hartge, P.; Augsburger, J.; Hoover, R. N. and Fraumeni, J. F. (1985) Sunlight exposure as risk factor for intraocular malignant melanoma. *New Engl. J. Med.*, **313**: 789-792.
- Vajdic, C. M.; Kricger, A.; Giblin, M.; McKenzie, J.; Aitken, J.; Giles, G. G. and Armstrong, B. K. (2001) Eye color and cutaneous nevi predict risk of ocular melanoma in Australia. *Int. J. Cancer*, **92**: 906-912.

- Vincensi, M. R.; D'Ischia, M.; Napolitano, A.; Procaccini, E. M.; Riccio, G.; Monfrecola, G.; Santolanni, P. and Prota, G. (1998) Phaeomelanin versus eumelanin as a chemical indicator of ultraviolet sensitivity in fair-skinned subjects at high risk for melanoma: a pilot study. *Melanoma Res.*, **8**: 53-58.
- Wakamatsu, K.; Hu, D.-N.; McCormick, S. A. and Ito, S. (2007) Characterization of melanin in human iridal and choroidal melanocytes from eyes with various colored irides. *Pigment Cell Mel. Res.*, **21**: 97-105.
- Wakamatsu, K. and Ito, S. (2002) Advanced chemical methods in melanin determination. *Pigment Cell Res.*, **15**: 174-183.
- Wakamatsu, K.; Kavanagh, R.; Kadekaro, A. L.; Terzieva, S.; Sturm, R. A.; Leachman, S.; Abdel-Malek, Z. and Ito, S. (2006) Diversity of pigmentation in cultured human melanocytes is due to differences in the type as well as quantity of melanin. *Pigment Cell Res.*, **19**: 154-162.
- Wakamatsu, K.; Ohtara, K. and Ito, S. (2009) Chemical analysis of late stages of pheomelanogenesis: conversion of dihydrobenzothiazine to a benzothiazole structure. *Pigment Cell Mel. Res.*, **22**: 474-486.
- Wenczl, E.; van der Schans, G. P.; Roza, L.; Kolb, R.; Smit, N. and Schothorst, A. A. (1998a) UVA-induced oxidative DNA damage in human melanocytes is related to their (pheo)melanin content. *J. Invest. Derm.*, **110**: 693-693.
- Wenczl, E.; Van der Schans, G. P.; Roza, L.; Kolb, R. M.; Timmerman, A. J.; Smit, N. P. M.; Pavel, S. and Schothorst, A. A. (1998b) (Pheo)melanin photosensitizes UVA-induced DNA damage in cultured human melanocytes. *J. Invest. Derm.*, **111**: 678-682.
- Wetlaufer, D. (1962) Ultraviolet spectra of proteins and amino acids. *Adv. Protein Chem.*, **17**: 303-390.
- Williams, M. A.; Pinto, L. H. and Gherson, J. (1985) The retinal pigment epithelium of wild type (C57BL/6J +/+) and pearl mutant (C57BL/6J pe/pe) mice. *Invest. Ophthalmol. Visual Sci.*, **26**: 657-669.
- Xiong, G.; Joly, A. G.; Hess, W. P.; Cai, M.-D. and Dickinson, T. J. (2006) Introduction to photoelectron emission microscopy: principles and applications. *J. Chin. Electr. Microsc. Soc.*, **25**: 15-25.

- Ye, T.; Hong, L.; Garguilo, J.; Pawlak, A.; Edwards, G. S.; Nemanich, R. J.; Sarna, T. and Simon, J. D. (2006) Photoionization thresholds of melanins obtained from free electron laser–photoelectron emission microscopy, femtosecond transient absorption spectroscopy and electron paramagnetic resonance measurements of oxygen photoconsumption. *Photochem. Photobiol.*, **82**: 733-737.
- Ye, T.; Pawlak, A.; Sarna, T. and Simon, J. D. (2008) Different molecular constituents in pheomelanin are responsible for emission, transient absorption and oxygen photoconsumption. *Photochem. Photobiol.*, **84**: 437-443.
- Zeman, M.; Fulton, C.; Lucovsky, G. and Nemanich, R. (2006) Thermal stability of TiO, ZrO, or HfO on Si (100) by photoelectron emission microscopy. *J. Appl. Phys.*, **99**: 023519.

Biography

Dana Nicole Peles

Personal

Born November 1, 1983 in Denver, Colorado, USA.

Education

| | | |
|----------------------------------|------------------------|-----------|
| B.Sc., Chemistry and Mathematics | Randolph-Macon College | May 2006 |
| Ph.D., Chemistry | Duke University | July 2011 |

Publications

John D. Simon, Lian Hong and Dana N. Peles, (2008) Insights into Melanosomes from some Interesting Spatial and Temporal Properties, *Journal of Physical Chemistry B.*, **112**, 13201-13217.

Dana N. Peles and John D. Simon, (2009) Challenges in Applying Photoemission Electron Microscopy to Biological Systems, *Photochemistry and Photobiology*, **85**, 8-20.

Dana N. Peles, Lian Hong, John D. Simon and Dan-Ning Hu, (2009) Structural Characterization of Colored Human Iridal Melanosomes by Photoelectron Emission Microscopy, *Proceedings of SPIE*, **7182**, 7182E-1-7182E-9.

Dana N. Peles, Lian Hong, Dan-Ning Hu, Shosuke Ito, Robert J. Nemanich and John D. Simon, (2009) Human Iridal Stroma Melanosomes of Varying Pheomelanin Content Possess a Common Eumelanin Outer Surface, *Journal of Physical Chemistry B.*, **113**, 11346-11351.

John D. Simon, Dana N. Peles, Kazumasa Wakamatsu and Shosuke Ito, (2009) Current Challenges in Understanding Melanogenesis: Bridging Chemistry, Biological Control, Morphology and Function, *Pigment Cell and Melanoma Research*, **22**, 563-579.

Dana N. Peles and John D. Simon, (2010) Direct Measurement of the Ultraviolet Absorption Coefficient of Single Retinal Melanosomes, *Photochemistry and Photobiology*, **86**, 279-281.

Dana N. Peles and John D. Simon, (2010) The Ultraviolet Absorption Coefficient of Melanosomes Decreases with Increasing Pheomelanin Content, *Journal of Physical Chemistry B.*, **114**, 279-281.

Dana N. Peles, Erica Lin, Kazumasa Wakamatsu, Shosuke Ito and John D. Simon, (2010) Ultraviolet Absorption Coefficients of Melanosomes Containing Eumelanin as Related to the Relative Content of DHI and DHICA, *Journal of Physical Chemistry Letters*, **1**, 2391-2395.

John D. Simon and Dana N. Peles, (2010) The Red and the Black, *Accounts of Chemical Research*, **43**, 1452-1460.

Honors

Phi Lambda Upsilon, Member since January 2007
Honorary Chemical Society

Paul Mangus Gross Fellowship, June 2008
Awarded annually to two graduate students who have met and surpassed academic and research expectations in the doctoral program.

William Krigbaum Fellowship, June 2010
Awarded annually to a stellar physical chemist.

Charles Bradsher Fellowship, June 2010
Awarded annually to an outstanding graduate student in chemistry.